Convective-Reactive Nucleosynthesis in Oxygen-Carbon Shell Mergers

by

Joshua Issa
B.Sc., University of Waterloo, 2023

A Thesis Submitted in Partial Fulfillment of the
Requirements for the Degree of

MASTER OF SCIENCE

in the Department of Physics and Astronomy

We acknowledge and respect the Lək̓ʷəŋən (Songhees and Xʷsepsəm/Esquimalt) Peoples on whose territory the university stands, and the Lək̓ʷəŋən and W̱SÁNEĆ Peoples whose historical relationships with the land continue to this day.

Convective-Reactive Nucleosynthesis in Oxygen-Carbon Shell Mergers

by

Joshua Issa
B.Sc., University of Waterloo, 2023

Supervisory Committee

Dr. F. Herwig, Supervisor
(Department of Physics and Astronomy University of Victoria)

Dr. I. Dillmann, Co-Supervisor
(Senior Research Scientist, TRIUMF
Adjunct Professor, Department of Physics and Astronomy University of Victoria)

Abstract

Many massive stars models at the end of their lives can have a merger between the convective O-burning shell and C-burning shells known as a O-C shell merger. During the merger, the material in the C-burning shell is ingested into the much hotter O-burning shell. Stellar models that have O-C shell mergers have been found to produce the stable isotopes of phosphorus, potassium, chlorine, and scandium which are otherwise not produced by stellar models to match the solar observations. O-C shell mergers are also a site for the production of the p nuclei, a group of 35 n-deficient stable isotopes produced by photo-induced reactions in this scenario. Part of the reason for this is that the O-burning shell is a convective-reactive environment, meaning that the timescales of the convective mixing and the nuclear reactions are comparable. Because of this, isotopes can be react at one location in the shell and the products can be transported to another location in the shell where they can be further processed. This changes which nucleosynthetic pathways are dominant and which isotopes are produced.

Stellar models calculate the stellar evolution and nucleosynthesis of the merger in 1D, but 3D hydrodynamic simulations significantly disagree with the 1D models at these late stages of stellar evolution. Convective velocities in 3D are much higher than 1D, the convective mixing profile features a downturn near the convective boundaries, the flow has large scale non-radial asymmetries, and the rate of ingesting C-shell material can be significantly lower. This is important for understanding the nucleosynthesis in the O-C shell merger, because if the convective velocities are different, then the timescale for mixing changes and the possible nucleosynthetic pathways can be altered.

In this thesis, I implement the insights from 3D hydrodynamic simulations into 1D stellar evolution models to determine how the macrophysical uncertainties in the O-C shell merger impact the nucleosynthesis in a convective-reactive environment, particularly for the p nuclei. I also investigate the impact of nuclear reaction uncertainties on the nucleosynthesis of the p nuclei during the O-C shell merger and this is influenced by the mixing conditions.

Table of Contents

List of Tables

List of Figures

Acknowledgements

This thesis did not happen by accident, nor by some unique gift I alone have. I would like to thank of primary importance Dr. Falk Herwig and Dr. Iris Dillmann. Without your patience, teaching and supporting me through all my doubts and mistakes, this work would not have happened. Thank you for all the doors you have opened and the opportunities you have given me. I would also like to thank Dr. Pavel Denissenkov for his constant availability to answer all my programming questions and showing me how to use all the tools I needed to do this work. I am deeply grateful to have learned from you all.

To my parents, who have always been supportive of me. Thank you to my mother who taught me how to critically engage in the world and refuse to take things at face value. Thank you to my father who taught me what a life long dedication to learning looks like and insisting that I become a doctor of stars.

To Sneha, my companion. Words can't begin to express how grateful I am for your support and love, always being there and excited for every step that I have taken in this journey. Thank you for the FaceTime calls to wake me up in the morning, and the late night scrolls through Instagram together. Thank you for the motivation every day to work hard and shoot for the stars.

To Mr. Hordyk who told me I would do great things, Mr. Koiter who taught me physics and sparked my love for it, and Mr. Blyleven who who took me from a student who couldn't program Hello World to helping me land my first programming job, thank you for shaping me to be the scientist I am today. I still hear your advice to this day, and I am the better for it.

To my friends in Victoria and Vancouver who have been there through the frustrations and the joys. Thank you Praneet, Maeve, Mallory, Daniel, Bryn, Diego, Dhwani, Layla, Aviv, Ruxin, and Jono. Grad school without you all would have been a sad and lonely place.

I acknowledge and respect the Ləḱʷəŋən (Songhees and Xʷsepsəm/Esquimalt) Peoples on whose territory I live and work on, and the Ləḱʷəŋən and W̱SÁNEĆ Peoples whose historical relationships with the land continue to this day.

Well, I am just a humble theologian, and as far as I am concerned the whole of astronomy can be summed up by saying 'Twinkle, twinkle little star, how I wonder what you are.'

- Karl Barth

Dedication

To my parents who taught me how to see the world, my high school teachers who gave me my passion for computational physics, and to my fiancée who has been my biggest supporter in grad school and in life. Thank you.

Chapter 1

Introduction

The origin of the elements in the universe is a fundamental question in astrophysics. The elements are produced in stars by various nuclear reactions during their lifetimes and deaths. Nuclear astrophysics studies what specific processes are responsible for the synthesis of the elements. The seminal work done by Burbidge et al. (1957) laid the foundation for nuclear astrophysics, describing the formation of all isotopes in stars via a series of burning stages and nuclear processes, and proposing likely stellar conditions where they happen. Shortly after, Henyey et al. (1964) introduced a numerical method to model helium formation in stars via the CNO cycle. Since then, computational nuclear astrophysics has progressed significantly, enabling detailed modeling of stellar evolution across a wide range of masses and metallicities (Pignatari et al., 2016b; Ritter et al., 2018b; Battino et al., 2019).

1.1 Motivation

As far as computational nuclear astrophysics has come, there are still open questions regarding the origin of all isotopes. The stellar models that calculate the nucleosynthesis are typically one dimensional, relying on the assumptions of spherical symmetry and mixing length theory to describe the convective motions in stars. While these assumptions are adequate for much of the star's life, they do not hold as the star reaches the end of its life, particularly for massive stars. The goal of this thesis is to investigate how the nucleosynthesis of isotopes during the late stages changes when taking into account the three dimensional nature of stars.

1.2 Stars and the Origin of the Elements

Stars are the primary sites for the formation of elements through nuclear fusion. However, not all elements are synthesized at the same stage of a star's life cycle. Low-mass stars, with masses less than 3 $M_\odot$, spend most of their lifetimes burning hydrogen into helium in their cores. After exhausting the hydrogen in their cores, these stars expand into red giants and cease core hydrogen fusion, continuing to burn hydrogen in a shell surrounding the core. Eventually, the core becomes degenerate and undergoes a sudden flash of helium fusion, initiating the production of carbon as the star enters the asymptotic giant branch (AGB) phase. During the AGB phase, core helium fusion ceases, but helium continues to burn in a shell around the core. At this stage, the convective envelope can expand and mix hydrogen into the helium-burning shell, leading to recurrent flashes known as thermal pulses. These thermal pulses release large numbers of neutrons, enabling the synthesis of many elements heavier than iron. Ultimately, the star sheds its outer layers, leaving behind a planetary nebula and a white dwarf, and ceases to produce new elements. Intermediate-mass stars, with masses between 3 $M_\odot$ and 8 $M_\odot$, do not undergo a helium flash. Instead, after exhausting core hydrogen, they fuse helium into carbon and oxygen in their cores. Once core helium is depleted, these stars may also fuse carbon into neon, but do not produce elements heavier than this, and eventually become white dwarfs. (Prialnik, 2009; Herwig, 2013)

Massive stars, with masses greater than 8 $M_\odot$, also begin their lives by fusing hydrogen to helium in their cores, but they continue to fuse into heavier and heavier elements as they evolve. After they exhaust hydrogen in their cores, they will begin to fuse helium into carbon and oxygen in their cores. Then they will continue to fuse carbon, neon, oxygen, and eventually silicon. Once they begin to fuse silicon in their cores, they will begin to produce iron. Once iron begins to form in the core of stars, they begin to collapse as the fusion of elements heavier than iron is endothermic and does not produce energy. This collapse causes the star to explode in a supernova and many nuclear reactions can occur. After the supernova, the remnant core of the star can either become a neutron star or a black hole depending on the mass before collapse (Woosley et al., 2002; Prialnik, 2009).

The rest of the elements heavier than iron that are not produced in AGB stars or supernovae of massive stars are mostly produced during the merger of two neutron stars. When two neutron stars merge, they produce extremely high densities of neutrons and the heaviest stable elements in the universe are formed (Goriely et al., 2015). These astrophysical sites for the production of the elements are summarized in Figure 1.1.

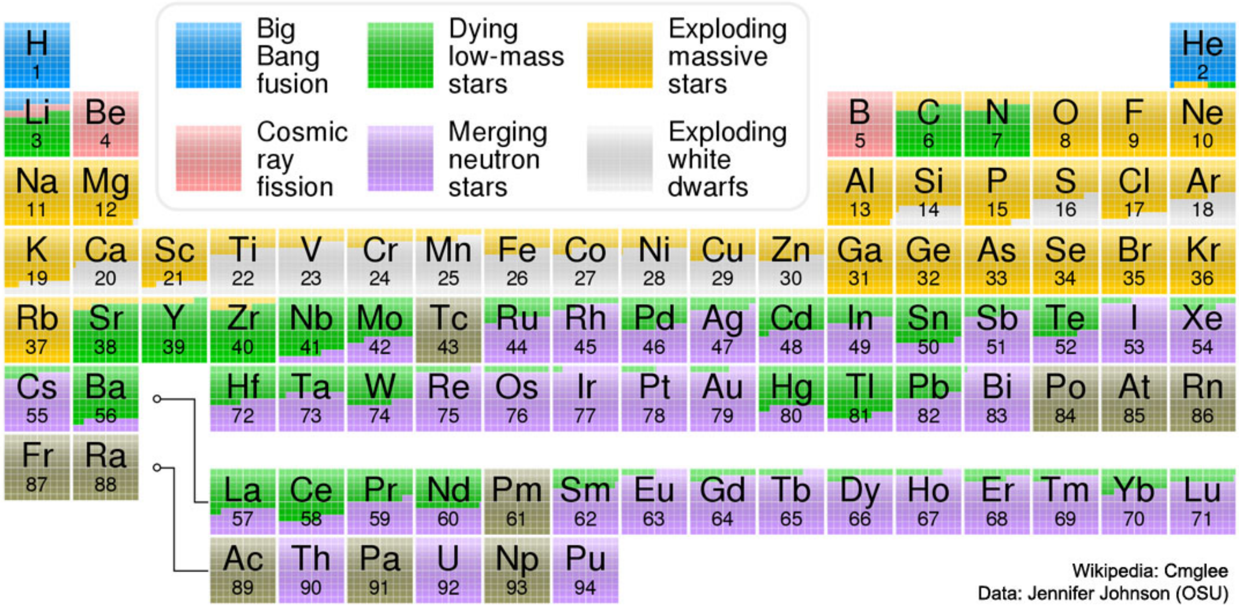

Figure 1.1: Taken from Johnson (2017): Periodic table shaded according to the origin of the elements in the solar system.

1.2.1 Massive Star Evolution

Stars with an inital mass greater than 8 $M_\odot$ undergo a series of nuclear burning phases:

$$\text{H} \rightarrow \text{He} \rightarrow \text{C} \rightarrow \text{Ne} \rightarrow \text{O} \rightarrow \text{Si} \rightarrow \text{Fe} \rightarrow \text{core collapse.}$$

These burning phases lead to the structure of the star being separated convective shells with primary burning structures, as seen in Figures 1.2 and 1.3.

After the formation of the Fe-core the star begins to rapidly contract as nuclear burning no longer can balance the gravitational force. This leads to a core collapse supernova explosion where further shockwave induced nucleosynthesis can occur (Woosley et al., 2002). The core of the star leaves behind a neutron star or black hole, and all other material beyond the mass cut is ejected into the interstellar medium. The exact border of where mass is ejected from changes the yields of massive star nucleosynthesis. Ritter et al. (2018b) place this mass cut for massive stars around the interface of the Si/O-shell.

1.2.2 O-C Shell Mergers

The burning shells of stars, as shown in Figures 1.2 and 1.3, are separated by radiative regions. Because of this, there is no material shared between the shells, but in the final stages

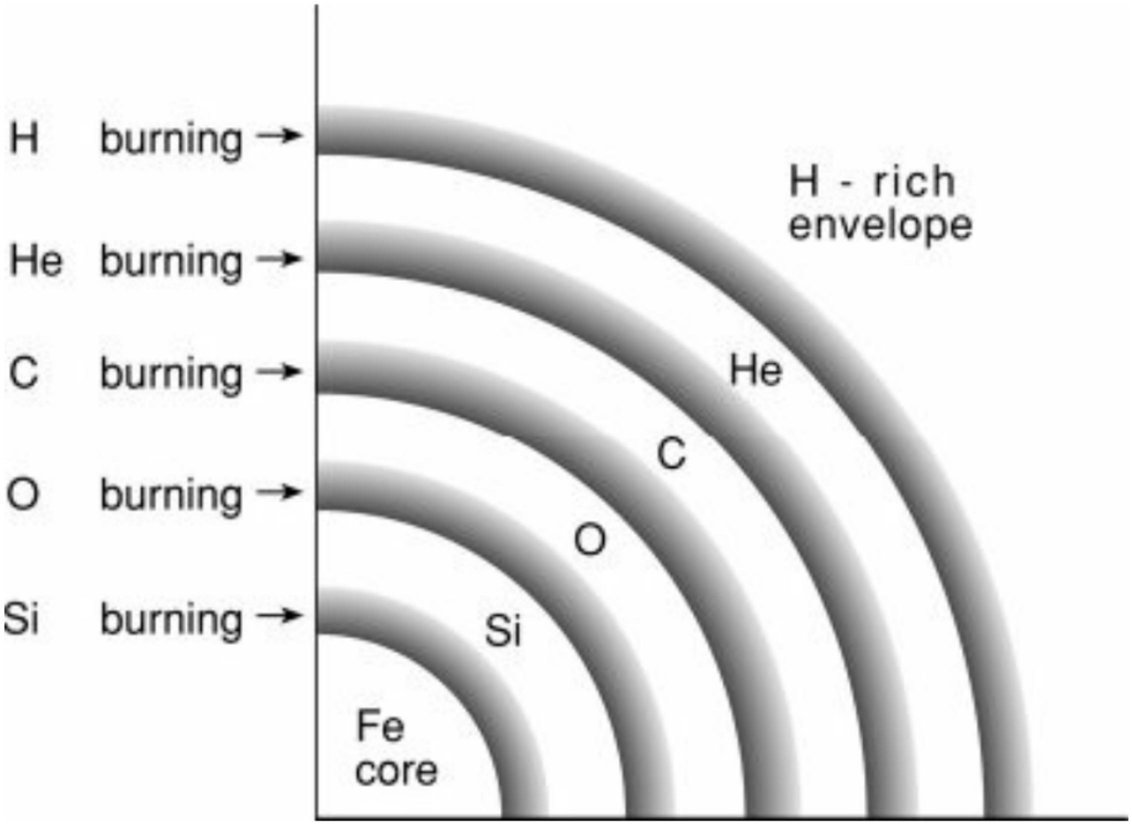

Figure 1.2: Taken from Prialnik (2009): Schematic structure of a supernova progenitor star. The Ne-burning layer is not shown but would be between the C- and O-layers.

of advanced O-shell stellar burning, hours before the core collapse of the star, anywhere from 20% to 40% of 1D massive star models have been found to have a merger of the O-, Ne-, and C-shells (Rauscher et al., 2002; Ritter et al., 2018a; Collins et al., 2018; Roberti et al., 2023, 2025). This phenomenon is known as an "O-C shell merger". Figure 1.4 shows a Kippenhahn diagram of the merger of the O- and C-burning shells for a 15 $M_\odot$ $Z = 0.02$ model from Ritter et al. (2018b). These mergers occur when the convective O- and C-shells grow large enough to overlap, forming a single extended convective region. This happens when the upper boundary of the O-shell starts to grow and ingest some of the C-shell material. As this material enters the O-shell, it begins to burn at the higher temperatures of the O-shell and the compositions of the shells begin to mix.

These mergers are known to have peculiar markers of nucleosynthesis because the convective-reactive environment of the O-shell, such as the production of the odd-Z elements P, Cl, K, and Sc which are underproduced in galactic chemical evolution calculations (Ritter et al.,

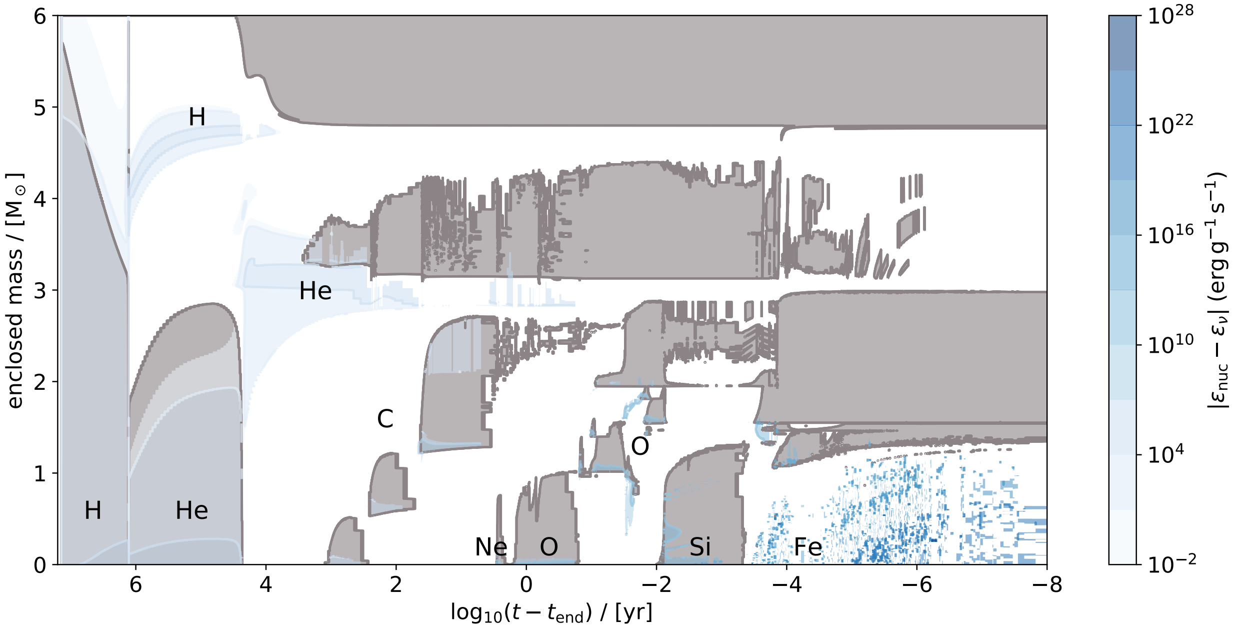

Figure 1.3: Kippenhahn diagram of the inner 6 M$_\odot$ of the 15 M$_\odot$ $Z = 0.02$ model from Ritter et al. (2018b) with labels for the main shell and core burning phases. Grey areas are convective regions, white areas are radiative regions, and blue areas show where nuclear burning occurs.

2018a; Roberti et al., 2025). The O-C shell merger has also been found to produce the p nuclei, heavy n-deficient isotopes, by photo-disintegrating stable heavy isotopes (Rauscher et al., 2002; Ritter et al., 2018a; Roberti et al., 2023).

O-C shell mergers have also been understood to be important for seeding asymmetries important for the supernova. The shell mergers are highly asymmetric and provide perturbations necessary for the supernova explosion in the O-shell (Müller, 2016; Collins et al., 2018; Müller, 2020; Yadav et al., 2020; Andrassy et al., 2020).

1.2.3 Hydrostatic Burning in Massive Stars

Burning in stars largely occurs in hydrostatic equilibrium, where the energy produced by nuclear reactions balances the gravitational forces acting on the star. This balance allows the star to maintain a stable structure and prevents it from collapsing under its own gravity. The burning phases in stars occur at specific range of temperatures and densities, depending on the initial mass of the star as shown in Table 1.1. Much of the nuclear burning in the core and shells of stars happens in convective regions which is a region where the stratification of the star is unstable and the material mixes. In this section, the details of the hydrostatic

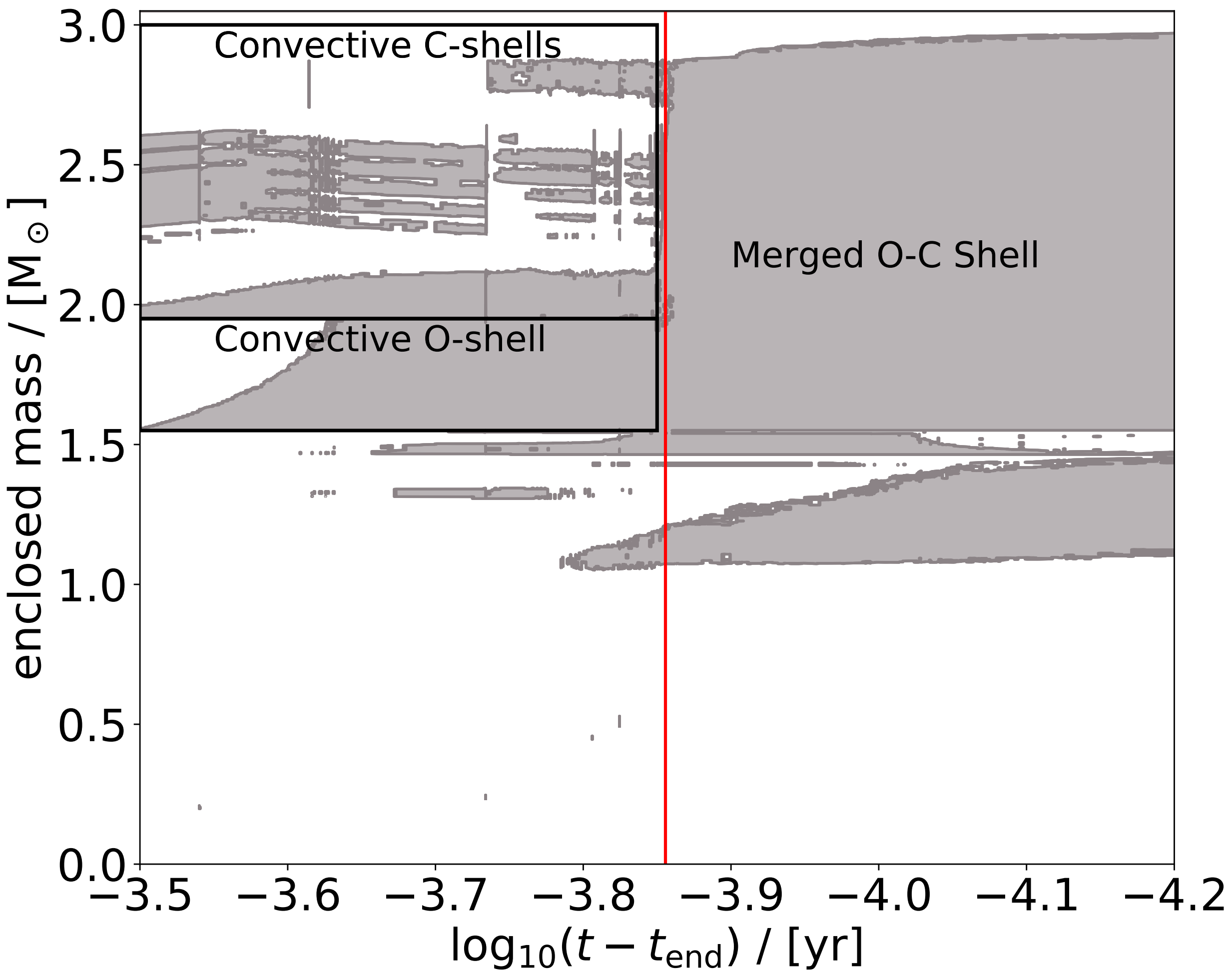

Figure 1.4: Zoom in view of Figure 1.3 showing the merger of the convective O and C-burning shells for the 15 M$_\odot$ $Z = 0.02$ model from Ritter et al. (2018b). The O-burning shell extends from 1.55−1.95 M$_\odot$. The first convective C-burning shell sits directly on top from 1.96−2.11 M$_\odot$ and additional convective C-burning shells that are ingested are above. The merger onsets at $\log_{10}(t - t_{\rm end})/{\rm yr} \approx -3.85$ and reaches full extent at ≈ -4.

burning phases in massive stars are described in more detail, along with the nuclear reactions that occur during these phases.

The following section describes the burning stages following Woosley et al. (2002) and Iliadis (2015). H-burning is the first stage of hydrostatic burning which occurs in stars, primarily by the CNO cycle.

$$^{12}{\rm C}(p,\gamma)^{13}{\rm N}(\beta^+)^{13}{\rm C}(p,\gamma)^{14}{\rm N}(p,\gamma)^{15}{\rm O}(\beta^+)^{15}{\rm N}(p,\alpha)^{12}{\rm C}$$

In the CNO cycle, carbon, nitrogen, and oxygen act as a catalyst for the fusion of four ^{1}H

Table 1.1: Details about hydrostatic burning phases in massive stars of 13–25 $M_\odot$ from Table 1 of Woosley et al. (2002).

Burning Phase	**Temperature (MK)**	**Density (g cm^{-3})**	**Timescale (yrs)**
H-burning	34.4–38.1	6.66–3.81	(13.5–6.70) $\times 10^7$
He-burning	172–196	(1.73–0.762) $\times 10^3$	(2.67–0.839) $\times 10^7$
C-burning	815–841	(3.13–1.29) $\times 10^5$	(2.82–0.522) $\times 10^3$
Ne-burning	1690–1570	(10.8–3.95) $\times 10^6$	0.341–0.891
O-burning	1890–2090	(8.19–3.60) $\times 10^6$	4.77–0.402
Si-burning	3280–3650	(4.83–3.01) $\times 10^7$	(48.8–2.0) $\times 10^{-3}$

isotopes into ^{4}He. If the star does not have enough carbon, nitrogen, and oxygen to catalyze the fusion of hydrogen, it will instead fuse hydrogen into helium by the three p-p chains:

$$p(p, e^+\nu)^2\mathrm{H}(p,\gamma)^3\mathrm{He}(^3\mathrm{He}, 2p)^4\mathrm{He}$$

$$p(p, e^+\nu)^2\mathrm{H}(p,\gamma)^3\mathrm{He}(\alpha,\gamma)^7\mathrm{Be}(e^-,\nu)^7\mathrm{Li}(p,\alpha)\alpha$$

$$p(p, e^+\nu)^2\mathrm{H}(p,\gamma)^3\mathrm{He}(\alpha,\gamma)^7\mathrm{Be}(p,\gamma)^8\mathrm{B}(\beta^+\nu)^8\mathrm{Be}(\alpha)\alpha$$

After the hydrogen in the core of the star is used up, the star will begin to burn helium by two main processes that create carbon and oxygen:

$$^4\mathrm{He} + {}^4\mathrm{He} \longleftrightarrow {}^8\mathrm{Be} + \alpha \rightarrow {}^{12}\mathrm{C} + \gamma \quad \text{and} \quad {}^{12}\mathrm{C} + \alpha \rightarrow {}^{16}\mathrm{O} + \gamma$$

^{8}Be has a very short half-life of 8.2×10^{-17} s and decays back into two α particles, but a quasi-equilibrium state is reached between its formation and decay rate. A small fraction of these ^{8}Be nuclei capture another α before decaying, forming ^{12}C through the resonant Hoyle state. After helium is exhausted, the massive star will begin to fuse carbon either in its core or slighly above the core and primarily produce neon, magnesium, and sodium:

$$^{12}\mathrm{C} + {}^{12}\mathrm{C} \rightarrow {}^{20}\mathrm{Ne} + \alpha$$

$$^{12}\mathrm{C} + {}^{12}\mathrm{C} \rightarrow {}^{23}\mathrm{Na} + p$$

$$^{12}\mathrm{C} + {}^{16}\mathrm{O} \rightarrow {}^{24}\mathrm{Mg} + \alpha$$

$$^{12}\mathrm{C} + {}^{12}\mathrm{C} \rightarrow {}^{23}\mathrm{Mg} + n$$

When the carbon burning stops, the star will begin to burn neon in the core which first produces ^{16}O by photo-induced emission of an α particle, and then produces ^{24}Mg by the capture of the released α on ^{20}Ne:

$$^{20}\mathrm{Ne} + \gamma \to {}^{16}\mathrm{O} + \alpha$$

$$^{20}\mathrm{Ne} + \alpha \to {}^{24}\mathrm{Mg} + \gamma$$

After neon burning is complete, the star will begin to fuse oxygen in its core into silicon, sulfur, phosphorus, and magnesium:

$$^{16}\mathrm{O} + {}^{16}\mathrm{O} \to {}^{28}\mathrm{Si} + \alpha$$

$$^{16}\mathrm{O} + {}^{16}\mathrm{O} \to {}^{31}\mathrm{S} + n$$

$$^{16}\mathrm{O} + {}^{16}\mathrm{O} \to {}^{31}\mathrm{P} + p$$

With a core composed of ^{28}Si, it will be burned by photo-disintegration reactions (γ, α), (γ, n), and (γ, p). Once enough α particles are produced by these photo-disintegration reactions, there can be a net production elements up to iron and nickel:

$$^{28}\mathrm{Si}(\alpha,\gamma)^{32}\mathrm{S}(\alpha,\gamma)^{36}\mathrm{Ar}(\alpha,\gamma)^{40}\mathrm{Ca}(\alpha,\gamma)^{44}\mathrm{Ti}(\alpha,\gamma)^{48}\mathrm{Cr}(\alpha,\gamma)^{52}\mathrm{Fe}(\alpha,\gamma)^{56}\mathrm{Ni}$$

Finally, during the explosive burning conditions of the core collapse, the star will produce elements like Ti, Cr, V, and Mn.

1.2.4 Galactic Cosmic Rays

Galactic cosmic rays are high-energy particles originating from outside the solar system, primarily composed of protons, α particles, and small fraction of heavy nuclei that come from high energy astrophysical sites like a supernovae, stellar winds released by supernovae remnants, or hot ionized interstellar medium. As these rays travel, they interact with interstellar gas and dust and produce the light elements Li, Be, and B by spallation reactions (Mitler, 1970; Mewaldt, 1988; Meyer et al., 1997; Iliadis, 2015; Lingenfelter, 2019; Tatischeff et al., 2021).

1.2.5 Neutron Captures

Neutron captures are an important part of how elements heavier than iron are formed. In the neutron capture processes, an iron nucleus in a neutron rich environment captures neutrons by (n, γ) reactions and becomes increasingly n rich and unstable. The unstable nucleus then β^- decays until it becomes a stable isotope. The neutron capture processes are divided into three main regimes: the slow, intermediate, and rapid neutron capture processes, commonly referred to as the s, i, and r processes. The s and r processes were originally proposed by Burbidge et al. (1957) and the i process was later identified by Cowan and Rose (1977). The name of each process refers to the speed at which the neutron captures occur compared to the β^- decay timescale. The faster the neutron captures occur, the more unstable the nucleus becomes and it travels further from the valley of stability. Finally, a neutron shell becomes full when a nucleus has 50, 82, or 126 neutrons, which corresponds to Sr/Y/Zr, Ba/La/Ce/Nd, and Pb/Bi. When this happens, the (n, γ) cross section becomes lower, making it more likely that the nucleus will undergo β^- decay rather than capture another neutron.

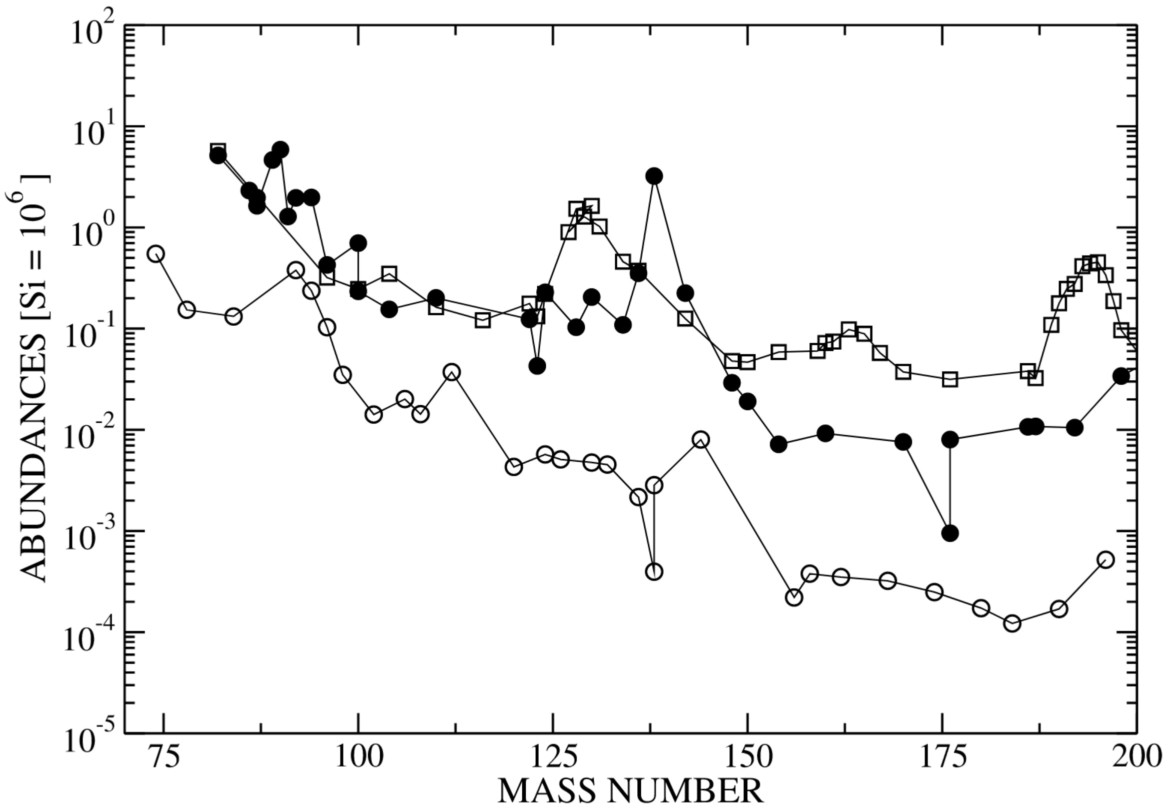

Figure 1.5: Taken from Rapp et al. (2006): Abundance distribution of heavy isotopes that can be entirely ascribed to s process (filled circles), r process (squares), and p process (open circles) nucleosynthesis.

The s process primarily occurs in AGB stars during their thermal pulse phase. Periodic

He-shell flashes generate a convective zone in the He-intershell, which mixes freshly synthesized ^{12}C. After the pulse, the convective envelope can penetrate into this region (third dredge-up), bringing carbon and other products to the surface. Between pulses, a ^{13}C pocket is formed when protons partially mix into the ^{12}C-rich intershell, leading to ^{13}C production via $^{12}\mathrm{C}(p,\gamma)^{13}\mathrm{N}(\beta^{+})^{13}\mathrm{C}$. The ^{13}C subsequently reacts via $^{13}\mathrm{C}(\alpha,n)^{16}\mathrm{O}$, releasing neutrons with densities of $10^{6}-10^{10}$ cm^{-3}, driving the s-process nucleosynthesis close to the valley of stability. Additional neutrons are briefly produced during He-shell flashes from ^{22}Ne which comes from $^{14}\mathrm{N}(\alpha,\gamma)^{18}\mathrm{F}(\beta^{+})^{18}\mathrm{O}(\alpha,\gamma)^{22}\mathrm{Ne}$ and releases neutrons by $^{22}\mathrm{Ne}(\alpha,n)^{25}\mathrm{Mg}$ (Sneden et al., 2008; Herwig, 2013). In massive stars, a weaker form of the s process occurs during the He- and C-burning phases where neutrons are released by $^{22}\mathrm{Ne}(\alpha,n)$ (Pignatari et al., 2010; Käppeler et al., 2011).

The i process has two sites considered for its production: metal poor AGB stars and rapidly accreting white dwarfs. If an AGB star is metal poor, when it undergoes its third thermal pulse it can sustain a longer connection between the H and He rich layers and produce neutron densities of $10^{13}-10^{15}$ cm^{-3} (Choplin et al., 2021). If a white dwarf has a main sequence star binary companion, it can accrete the H-rich material from its companion. As hydrogen is accreted onto the white dwarf, it burns and creates a He-shell. When the He-shell reaches a critical mass, it will undergo a flash and release neutrons by $^{13}\mathrm{C}(\alpha,n)^{16}\mathrm{O}$ (Denissenkov et al., 2021). i-process nucleosynthesis has a similar peak abundance pattern to the s process as it does not travel significantly farther from the valley of stability, the primary difference being which isotope is the most abundant (Choplin et al., 2021).

The r process is thought to occur in the merger of two neutron stars, as when they merge they produce a large number of neutrons at densities greater than 10^{20} cm^{-3}. The neutron captures in the r process occur so rapidly that the nuclei produced are extremely unstable and travel far from the valley of stability. The r process abundance distribution shows peaks at $A = 80$, $A = 130$, and $A = 195$. The $A = 130$ and $A = 195$ peaks come from the fission of n-heavy actinides (Arnould et al., 2007; Goriely et al., 2015; Mumpower et al., 2018). A weaker form of the r process may occur in the supernova of a massive star which produces isotopes up to $A = 130$ (Woosley and Hoffman, 1992; Kobayashi et al., 2020).

1.2.6 p-Nuclei Nucleosynthesis

The p nuclei are a set of 35 n-deficient stable isotopes from ^{74}Se to ^{196}Hg that make up a small fraction of the observed solar abundance distribution of their respective elements (Rapp et al., 2006; Rauscher et al., 2013). These isotopes are typically 10–1000 times less abundant than their stable n-rich counterparts as seen in Figure 1.5. Burbidge et al. (1957) first identified these isotopes as a distinct group, and did not think that the p nuclei were produced by the neutron capture processes. Instead, they proposed that a series of (p, γ) reactions in equilibrium with (γ, p) and (γ, n) reactions in the H-rich envelope of a Type II supernova in a process they labelled the "p process". This is because the p nuclei are shielded from neutron captures by stable isotopes, as shown in Figure 1.6.

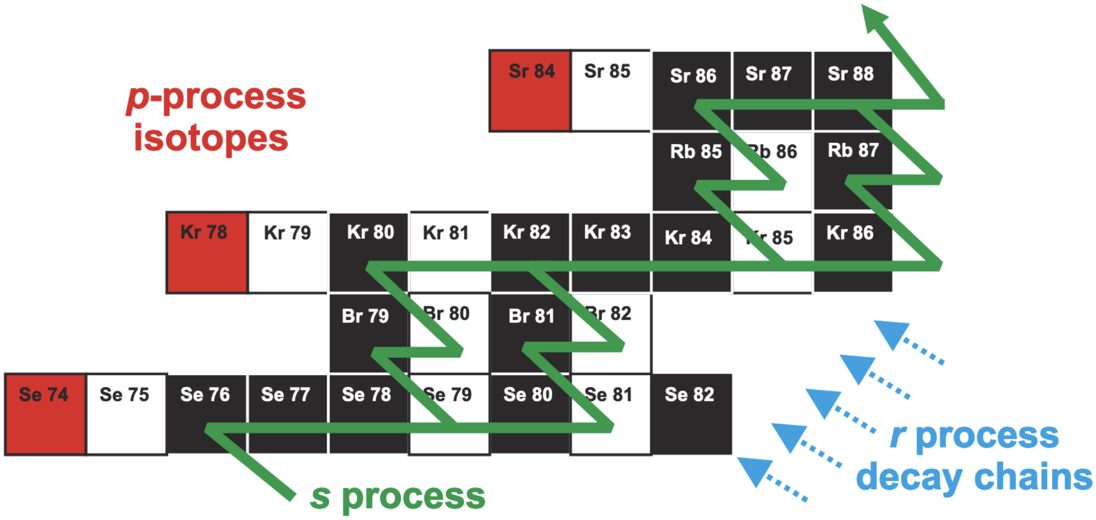

Figure 1.6: Taken from Rauscher et al. (2013): The p isotopes are shielded from r process decay chains by stable isotopes and are bypassed in the s process reaction flow.

Since the proposal of the p process by Burbidge et al. (1957), the common understanding is that the observed solar abundance of the 35 p nuclei is produced by a superposition of astrophysical processes. Some of the varied processes and sites that can produce the p nuclei include:

- ^{74}Se$-^{94}$Mo can be produced in the ejecta of a supernova during the α capture process by photo-disintegrations (Woosley and Hoffman, 1992).
- ^{74}Se$-^{108}$Cd can be produced by ν induced (n, p) reactions in the winds of a supernova (Fröhlich et al., 2006; Arcones and Montes, 2011).
- ^{84}Sr$-^{98}$Ru can be produced in a H-rich accretion disk around a neutron star by rapid (p, γ) and β^+ decay analogous to the neutron capture process (Schatz et al., 2001).
- ^{152}Gd, ^{164}Er, and ^{180m}Ta have significant contributions from the s process (Bisterzo et al., 2011).

- ^{113}In and ^{115}Sn can be made during the r process (Dillmann et al., 2008).
- ν capture reactions have been found to play a role in the production of ^{113}In, ^{138}La, and ^{180m}Ta (Goriely et al., 2001; Arnould and Goriely, 2003; Sieverding et al., 2018).

The majority of the p nuclei can be produced by the "γ process", a process that was first proposed by Woosley and Howard (1978) who did not think the temperatures of the H-envelope during a supernova were sufficient. The γ process is a secondary process that requires pre-existing stable nuclei that undergo photo-disintegrations (γ, n), (γ, α), and (γ, p) reactions to produce the p nuclei at temperatures of $(1.5-3) \times 10^9$K (Rauscher et al., 2013). Because it is a secondary process, the γ process is dependent on the metallicity of the star and seeds available (Travaglio et al., 2015; Battino et al., 2020).

One site where the γ process could take place is in the explosive O and Ne burning shells of a massive star (Woosley and Howard, 1978; Rayet et al., 1990; Rauscher et al., 2002). In this site, the p nuclei are produced, but there are serious underproductions of the light isotopes, especially ^{92,94}Mo and ^{96,96}Ru, ^{138}La, and ^{180m}Ta (Rapp et al., 2006; Rauscher et al., 2013; Pignatari et al., 2016a).

Another site is the explosion of white dwarfs during Type Ia supernova if the seeds for the process are enhanced. White dwarfs have s-process material from either during the prior AGB phase or from He-flashes during accretion from a companion star. When the white dwarf reaches the Chandrasekhar mass limit, it can explode in a Type Ia supernova and produce the p nuclei by the γ process (Travaglio et al., 2011, 2015). Rapidly accreting white dwarfs that have i-process nucleosynthesis are also able to produce the p nuclei by the γ process in the Type Ia supernovae (Battino et al., 2020). White dwarf explosions are able to produce the p nuclei apart from ^{113}In, ^{115}Sn, ^{138}La, ^{152}Gd, and ^{180m}Ta without an underproduction of the molybdenum and ruthenium isotopes (Rauscher et al., 2013).

It has also been found that the p nuclei can be produced in the O-C shell merger of a massive star before the supernova explosion (Rauscher et al., 2002; Ritter et al., 2018a; Roberti et al., 2023). As explained in Section 1.2.2, the stable isotopes in the C-shell are ingested into the much hotter temperatures of the O-shell. In the O-shell, the stable isotopes undergo photo-disintegration reactions and produce the p nuclei. A significant percentage of the final yields of the p nuclei with $A > 100$ are produced during the O-C shell merger independent of the peak explosion energy of the subsequent supernova (Roberti et al., 2023, 2024).

1.3 1D Stellar Modelling

Stars are 3D objects that are governed by the Navier-Stokes equations where the fluid is undergoing a series of nuclear reactions. The equations governing the hydrodynamic flow are given below (Kippenhahn et al., 2013):

$$\frac{\partial \rho}{\partial t} + \nabla \cdot (\rho \mathbf{v}) = 0 \tag{1.1}$$

$$\rho \left(\frac{\partial \vec{v}}{\partial t} + (\vec{v} \cdot \nabla)\vec{v} \right) = -\nabla P - \rho \nabla \Phi \tag{1.2}$$

$$\frac{dE}{dt} = -\frac{P}{\rho} \nabla \cdot \vec{v} + \epsilon - \frac{1}{\rho} \nabla \cdot \vec{F} \tag{1.3}$$

$$\nabla^2 \Phi = 4\pi G \rho \tag{1.4}$$

where ρ is the density, $\mathbf{v}$ is the velocity, P is the pressure, Φ is the gravitational potential, E is the specific internal energy, ϵ is the energy generation rate, and $\vec{F}$ is the energy flux.

These equations can be solved in 3D, but calculating the full 3D hydrodynamic equations for the entire evolution of a star is computationally expensive. This is because the timestep of the simulation is limited by the Courant-Friedrichs-Lewy (CFL) condition (Courant et al., 1928; Viallet et al., 2011) which states that the timestep must be small enough that the fluid does not travel more than one grid cell in a single timestep. The CFL condition which must be satisfied for the whole simulation is given by:

$$\Delta t \leq \frac{\Delta x}{|u| + c_s} \tag{1.5}$$

where Δx is the grid cell size, and $|u| + c_s$ is the fastest wave speed in the simulation. Depending on how much of the star is included and which stage of stellar evolution is being simulated, the timestep can be very short and following the evolution of a star can become computationally prohibitive. It becomes even more expensive if a nuclear reaction network is included. Some studies are able to calculate both the hydrodynamical and nuclear network equations together (Rizzuti et al., 2024b), but these are limited to a couple dozen species. Because of this, it is necessary to have a 1D approximation to be able to study the whole of stellar evolution.

1D stellar modeling requires the assumptions of spherical symmetry and hydrostatic equilibrium. Under spherical symmetry, all variables depend only on the radial coordinate r and time t. However, it is typical to replace the radial coordinate r with the mass coordinate

m, defined as the mass enclosed within radius r. This transformation allows all structural variables to be expressed as functions of m and t:

$$\rho = \rho(m,t), \quad P = P(m,t), \quad T = T(m,t), \quad L = L(m,t), \quad r = r(m,t)$$

The assumption of hydrostatic equilibrium implies that each mass shell remains static, with pressure gradients exactly balancing gravity at all times. This condition can be expressed as

$$\frac{\partial P}{\partial r} = -\frac{Gm\rho}{r^2}$$

Here, m is the mass enclosed within radius r, and G is the gravitational constant.

The radius as a function of m can be derived from mass conservation:

$$\frac{\partial r}{\partial m} = \frac{1}{4\pi r^2 \rho}$$

This equation relates the incremental change in radius to the local density and defines the geometry of the star.

The pressure gradient in terms of m follows from hydrostatic equilibrium and the geometric relation above:

$$\frac{\partial P}{\partial m} = -\frac{Gm}{4\pi r^4} \tag{1.6}$$

The luminosity gradient is derived from energy conservation. The luminosity L changes with m due to local energy generation and changes in internal energy:

$$\frac{\partial L}{\partial m} = \varepsilon_{\text{nuc}} - \varepsilon_\nu - c_P \frac{\partial T}{\partial t} + \frac{\delta}{\rho}\frac{\partial P}{\partial t} \tag{1.7}$$

Here, ε_{nuc} is the local nuclear energy generation rate per unit mass, and ε_ν is the energy loss rate from neutrinos. The terms involving c_P (specific heat at constant pressure) and δ account for changes in thermal and mechanical energy content, respectively.

The temperature structure is governed by the thermal gradient. The temperature gradient can be written as

$$\nabla \equiv \frac{d \ln T}{d \ln P}$$

In mass coordinates, this gives

$$\frac{\partial T}{\partial m} = -\frac{GmT}{4\pi r^4 P}\nabla \tag{1.8}$$

The actual value of ∇ depends on the mode of energy transport. In radiative regions, energy is carried by photons diffusing outward. The mean free path of photons is given by

$$\ell_{\mathrm{mfp}} = \frac{1}{\kappa\rho}$$

where κ is the opacity. Assuming local thermodynamic equilibrium and that $\ell_{\mathrm{mfp}} \ll r$, the radiative flux can be described as a diffusive process:

$$F = -\frac{4ac}{3}\frac{T^3}{\kappa\rho}\frac{\partial T}{\partial r}$$

where a is the radiation constant and c is the speed of light. Using the relation $L = 4\pi r^2 F$, one finds for the radiative gradient:

$$\nabla_{\mathrm{rad}} = \frac{3\kappa P L}{16\pi\ G\ a\ c\ m\ T^4} \tag{1.9}$$

In convective regions, energy is transported by adiabatic motions of fluid elements. If the gas is assumed to behave ideally, then

$$P = \frac{\mathscr{R}}{\mu}\rho T$$

where $\mathscr{R}$ is the gas constant and μ is the mean molecular weight. For adiabatic displacements, the pressure and density satisfy

$$P \propto \rho^{\gamma}$$

with adiabatic index γ. This yields

$$\nabla_{\mathrm{ad}} = 1 - \frac{1}{\gamma} \tag{1.10}$$

In general, the actual temperature gradient in convective regions is close to ∇_{ad} due to efficient mixing.

In radiative regions, only temperature gradients are equilibrated through photon diffusion. In convective regions, both temperature and composition gradients are homogenized as fluid elements exchange mass. Moreover, the assumption of adiabatic convection implies constant entropy along fluid trajectories. If a region transitions from radiative to convective, the entropy gradient must be flattened as mixing proceeds.

Finally, the chemical composition in stellar evolution is described by the mass fractions

X_i, satisfying $\sum_i X_i = 1$. The change in composition due to nuclear burning is given by

$$\left.\frac{dX_i}{dt}\right|_{\text{burn}} = \sum_j R_{ij} \tag{1.11}$$

where R_{ij} represents net reaction rates involving species i and j. Alternatively, in terms of number densities N_i, the general form is

$$\frac{dN_i}{dt} = \sum_{j,k} N_j N_k \langle\sigma v\rangle_{jk} - N_i \sum_j N_j \langle\sigma v\rangle_{ij} + \ldots + \sum_n N_n \lambda_n - N_i \lambda_i$$

Here, $\langle\sigma v\rangle$ denotes thermally averaged reaction rates, and λ represents decay rates.

Mixing of chemical species is described as a diffusive process:

$$\left.\frac{dX_i}{dt}\right|_{\text{mix}} = \frac{\partial}{\partial m}\left[(4\pi r^2 \rho)^2 D \frac{\partial X_i}{\partial m}\right] \tag{1.12}$$

where D is the effective diffusion coefficient describing convective or other mixing processes.

1.3.1 Mixing Length Theory Approximation

Prandtl (1925) was first to describe the turbulent flow of water through a channel by considering a characteristic length scale the eddies would travel before mixing with their surroundings. Following his insight, Böhm-Vitense (1958) developed the first stellar model using the idea of a characteristic length scale to describe the convective motions of the Sun.

Turbulent motions are complex 3D flows involving eddies of different shapes, velocities, and distances they travel before mixing with their environment. Rather than describing the flow of every individual fluid element, it models the average distance each fluid element travels, ℓ, before mixing with its surroundings. It also assumes that the average size of the fluid elements is equal to the travel distance ℓ. This is the "mixing length theory" (MLT) approximation. Fluid elements also have other average properties such as the velocity $\bar{v}$ they travel at and therefore an average timescale they travel for before becoming mixed with their surroundings $\tau = \ell/\bar{v}$ (Kippenhahn et al., 2013; Cox and Giuli, 1968; Joyce and Tayar, 2023). In stars, the average distance traveled ℓ is the mixing length ℓ_{MLT} and is given by:

$$\ell_{\text{MLT}} = \alpha_{\text{MLT}} \cdot H_P \tag{1.13}$$

where H_P is the pressure scale height and α_{MLT} is a dimensionless free parameter and can be chosen to match stellar evolution tracks to empirical data (Joyce and Tayar, 2023).

Prandtl (1925) used this assumption to describe the turbulent flows by a diffusion process, and this description of the motion is still the understood physical picture that MLT relies on (Joyce and Tayar, 2023). In the MLT approximation, the motion of fluid elements is characterized by a diffusion coefficient:

$$D_{\mathrm{MLT}} = \frac{1}{3} v_{\mathrm{conv}} \times \ell_{\mathrm{MLT}} \tag{1.14}$$

where v_{conv} are the average convective velocities of the fluid elements and ℓ_{MLT} is the mixing length. The timescale can also be re-written in terms of this diffusion coefficient and the mixing length (Herwig et al., 2011):

$$\tau_{\mathrm{MLT}} = \ell_{\mathrm{MLT}}^2 / D_{\mathrm{MLT}} \tag{1.15}$$

1.3.2 Stellar Evolution with `MESA`

The `Modules for Experiments in Stellar Astrophysics` (`MESA`) code is an open-source 1D stellar evolution framework used in stellar astrophysics that allows the computation of the structure and evolution of stars from pre-main sequence to advanced stages of burning up to the core collapse (Paxton et al., 2010). One of `MESA`'s distinguishing features is its implicit, fully coupled solution of the structure, nuclear burning, and mixing equations. The code employs a Newton-Raphson method to simultaneously solve the coupled set of equations of 1D stellar structure, diffusion of species, and nuclear reactions. The coupled equations allow `MESA` to resolve multi-timescale problems. In convective regions, `MESA` adopts a time-dependent diffusive mixing approximation, solving the mixing (subscript "mix") and nuclear burning (subscript "nuc") processes at the same time with operator coupling:

$$\left(\frac{dX_i}{dt}\right) \text{total} = \left(\frac{dX_i}{dt}\right)_{\text{nuc}} + \left(\frac{dX_i}{dt}\right)_{\text{mix}} \tag{1.16}$$

where X_i is the mass fraction of isotope i, and both terms are evaluated and advanced implicitly in a coupled fashion. Species mixing in `MESA` is taken to be diffusion (Paxton et al., 2010). `MESA` can include nuclear networks of hundreds of isotopes. However, solving large coupled equations takes a lot of computational power, and so stellar evolution calculations typically use reduced networks to capture the reactions that are relevant to energy generation without tracking full nucleosynthetic yields.

1.3.3 Post-Processing with `mppnp`

To obtain detailed nucleosynthesis predictions, it is necessary to post-process stellar models. One such code is `multi-zone post-processing network parallel` (`mppnp`) created by the `NuGrid` collaboration[1]. `mppnp` is a parallelized multi-zone code that takes as input an already evolved stellar structure and species from `MESA` and calculates the full nucleosynthesis of thousands of isotopes and tens of thousands of reactions.

Unlike the coupled equations of `MESA`, `mppnp` adopts an operator-split approach where it solves nuclear reactions and mixing separately in alternating steps:

1. The abundances X_i are updated via an implicit solver for nuclear reactions, using the supplied temperature and density histories.

2. The resulting abundances are then mixed by diffusion.

3. Optionally, an ingestion step can be included where a species is ingested at the top of region and mixed in.

By decoupling the nuclear physics from the stellar structure, `mppnp` is able to calculate large nuclear networks. However, if the timescales of mixing and burning are comparable, the operator-split approach can lead to inaccuracies in the final abundances.

1.3.4 Convective-Reactive Environments

One of the ways that a region of a star can be characterized is through the Dämkohler number (Dimotakis, 2005):

$$D_\alpha = \frac{\tau_{\mathrm{mix}}}{\tau_{\mathrm{burn}}} a \tag{1.17}$$

For the MLT scenario, τ_{mix} is given by Equation 1.15 and τ_{burn} is given by the timescale for nuclear burning, which can be approximated as the inverse of the reaction rates:

$$\tau_{\mathrm{react}} = \sum_j \frac{1}{\rho N_A \langle \sigma v \rangle X_j} \tag{1.18}$$

where ρ is the density, N_A is Avogadro's number, $\langle \sigma v \rangle_j$ the reaction rates contributing to some species, X_j is the mass fraction of the reacting species, and A_j is the mass number of the reacting species.

---

[1] Details about the NuGrid collaboration and their codes can be found at `https://nugrid.github.io/`.

Hydrostatic burning in convective regions is characterized by $D_\alpha \ll 1$. In this case, the mixing timescale is much shorter than the nuclear burning timescale, and the convective mixing is fast enough that the isotopes are mixed before they can undergo significant nuclear burning. Convective-reactive nucleosynthesis occurs when nuclear burning and convective mixing operate on comparable timescales, $D_\alpha = 1$ (Dimotakis, 2005; Herwig et al., 2011; Ritter et al., 2018b). In these conditions, the mass fractions of species are not well-mixed, and can undergo significant nuclear burning as they are being mixed. Reactions are not balanced across the region, and species are able to have different nucleosynthetic pathways depending on the temperature where $D_\alpha = 1$.

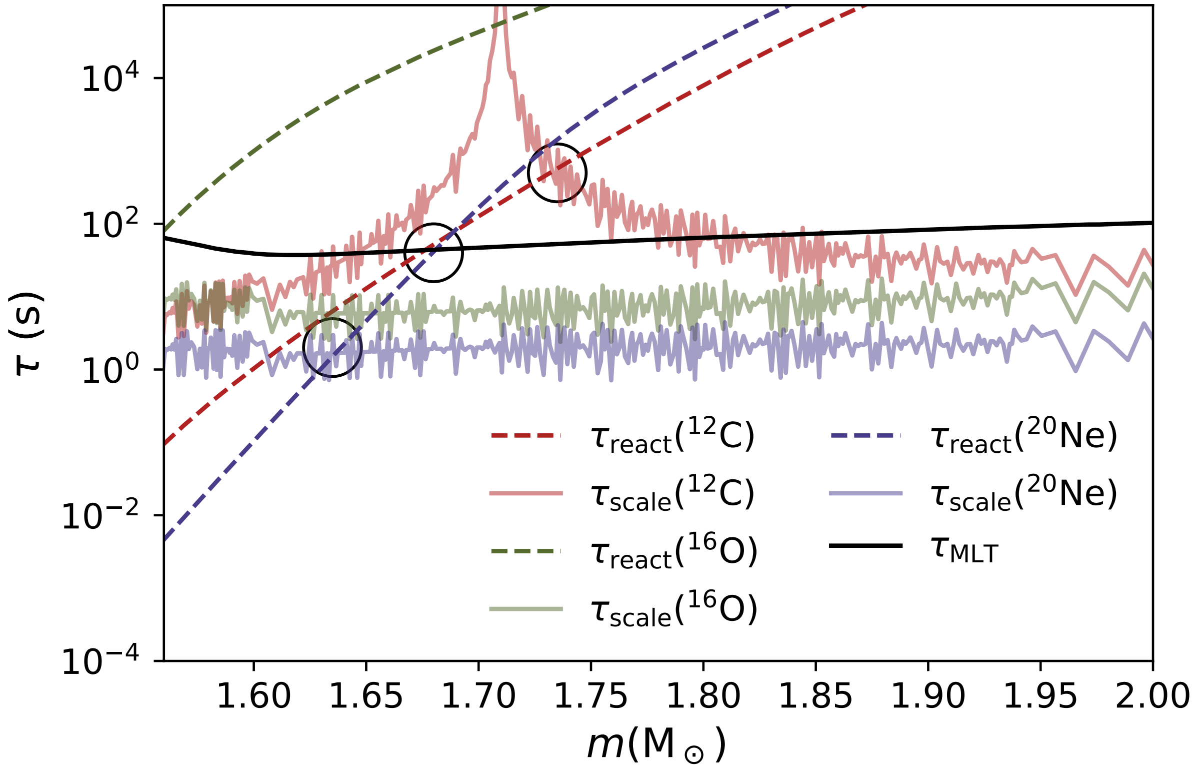

Figure 1.7: Timescales τ_{MLT}, τ_{react}, and τ_{scale} vs mass for the 15 $\mathrm{M}_\odot$ $Z = 0.02$ stellar model from Ritter et al. (2018b) during the merger at $\log_{10}(t - t_{\mathrm{end}}) \approx -3.88$. The black line is τ_{MLT}. The dashed red line is τ_{react} for ^{12}C, and the solid red line is τ_{scale} for ^{12}C. Likewise, the green lines are for ^{16}O, and the purple lines are for ^{20}Ne. Black circles are provided where $D_\alpha = 1$ for ^{12}C and ^{20}Ne.

Herwig et al. (2011) found that in a convective-reactive environment, the MLT mixing timescale is not always appropriate for describing the mixing timescale. They propose a reaction scale height timescale using the generalized principles of scale heights (Chapman, 1961):

$$H_\phi = \left(\frac{dln\phi}{dr}\right)^{-1} \tag{1.19}$$

where ϕ is the quantity of interest, in this case $\phi = \rho N_a \langle\sigma v\rangle$. The timescale associated with this scale height is given by (Herwig et al., 2011):

$$\tau_{\text{scale}} = \frac{H_\phi^2}{D_{\text{MLT}}} \tag{1.20}$$

and there would likewise be a Dämkohler number for the scale height where τ_{mix} is τ_{scale}.

Figure 1.7 shows that $D_\alpha = \tau_{\text{MLT}}/\tau_{\text{react}} = 1$ and $D_\alpha = \tau_{\text{MLT}}/\tau_{\text{scale}} = 1$ for ^{12}C and ^{20}Ne but $D_\alpha < 1$ for ^{16}O during the merger shown in Figure 1.4. As the merger progresses, the material that is ingested from the C-shell undergoes convective-reactive nucleosynthesis.

Since this is a convective-reactive environment, it is important to resolve the timescales for both mixing and burning. This is done by ensuring that there is little change in the final mass fraction when increasing the number of timesteps and mass zones in the simulation. As Figures 1.8 and 1.9 show, for the post-processing of the 15 $M_\odot$ $Z = 0.02$ stellar model from Ritter et al. (2018b), there is very little change in the final mass fractions of the p nuclei when the number of timesteps and mass zones are increased. The case with 200 mass zones in Figure 1.9 is strangely quite different from the other cases, but as the mass zones are increased to 400, the final mass fractions do not change significantly.

1.4 3D Macrophysics

Despite the value of 1D stellar evolution codes, stars are 3D objects that exhibit non-spherical features. The simplifications made by spherical symmetry and the MLT approximation do not sufficiently capture the 3D physics of convection. Because of this, there are modelling inconsistencies between 1D MLT predictions and 3D hydrodynamic simulations.

1.4.1 Limitations of MLT

As explained before, MLT assumes that there is some average length ℓ_{MLT} that all fluid elements travel in a convective environment before mixing with their surroundings.

One of the problems with MLT is how it treats the boundary between a convective region and a radiative region. As explained in Section 1.3 as defined by Equations 1.9 and 1.10, convective regions are described by $\nabla_{\text{ad}} < \nabla_{\text{rad}}$ and radiative regions where $\nabla_{\text{ad}} > \nabla_{\text{rad}}$. The boundary between these two regions is defined by the Schwarzschild criterion where

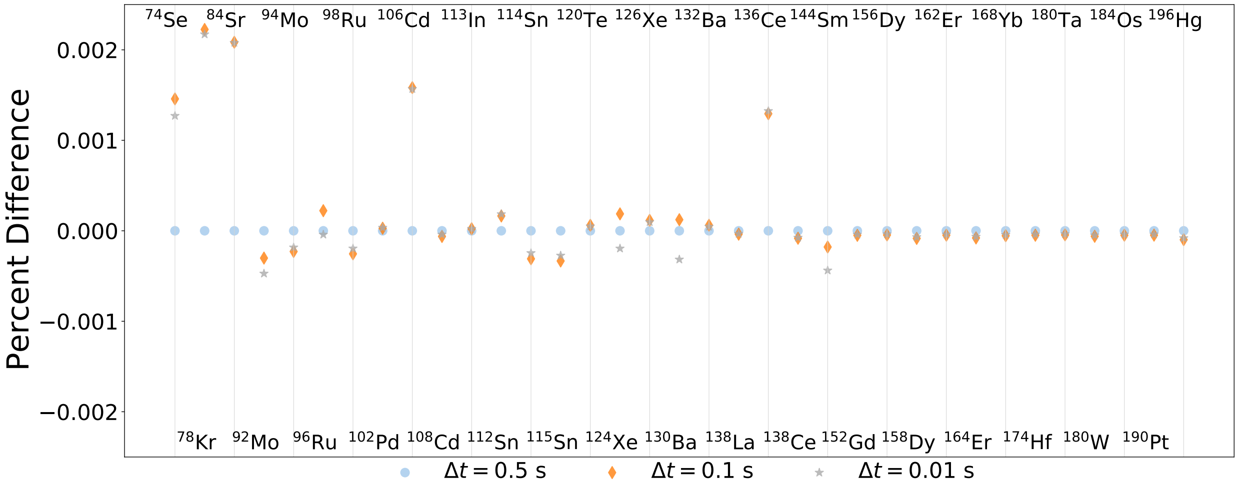

Figure 1.8: Time resolution test for the p nuclei using a post-processed model of the 15 $\mathrm{M}_\odot$ $Z = 0.02$ stellar model from Ritter et al. (2018b) at 110 s of ingestion and 400 mass zones. Percent difference is calculated as the (case $-$ $\Delta t = 0.5$ s)/($\Delta t = 0.5$ s). The $\Delta t = 0.5$ s case has a percent difference of 0%.

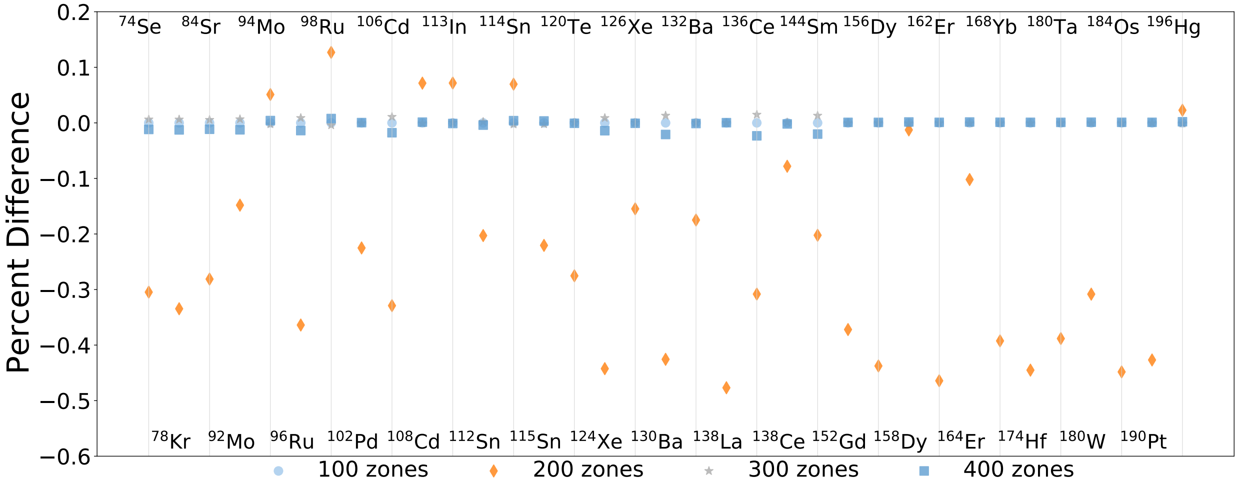

Figure 1.9: Mass resolution test for the p nuclei using a post-processed model of the 15 $\mathrm{M}_\odot$ $Z = 0.02$ stellar model from Ritter et al. (2018b) at 110 s of ingestion and 400 mass zones. Percent difference is calculated as the (case $-$ 100 zones)/(100 zones). The 100 zones case has a percent difference of 0%.

$\nabla_{\mathrm{ad}} = \nabla_{\mathrm{rad}}$. According to Equation 1.14, the diffusive coefficient for mixing is equal to the convective velocities. Outside the boundary of a convective region, suddenly $v_{\mathrm{conv}} = 0$ which would imply an unphysical infinite acceleration to stop the fluid at the edges. To treat the boundaries of convective regions, stellar evolution codes like `MESA` implement a convective overshooting parameterization where

$$D_{\mathrm{OV}} = D_{\mathrm{conv},0} \times \exp\left(-\frac{2z}{f\lambda_{P,0}}\right) \tag{1.21}$$

where $D_{\mathrm{conv},0}$ is the diffusion coefficient at the boundary, $\lambda_{P,0}$ is the pressure scale height at that location, z is the position in the radiative zone, and f is a free parameter so that the diffusion drops off exponentially rather than immediately (Paxton et al., 2010).

As described in Renzini (1987), there are some fundamental issues in using MLT to describe a convective region. One big issue is that the mixing length is assumed to be both the average distance a fluid element travels and its size. If the convective region is smaller than the mixing length, then it cannot resolve the mixing since it is smaller than a single fluid element. This applies to both convective regions and the overshooting region, which is a fraction of the pressure scale height. Therefore, for MLT to be a valid description, ℓ_{MLT} must be sufficiently small.

As recognized by Bazan and Arnett (1994), the O-burning shell cannot adequately be described by MLT. For example, Figure 1.10 shows the 15 $\mathrm{M}_{\odot}$ $Z = 0.02$ model from Ritter et al. (2018b) as it is merging. The O-burning shell has a size of 4.7×10^6 m, the merging region 1.07×10^6 m, and the C-burning shell 9.44×10^6 m. Since the fluid element in MLT is assumed to be the same size as the mixing length, it can be estimated that each region can resolve 3.2, 0.3, and 2.2 fluid elements respectively by dividing the lowest mixing length by the size of the region in Figure 1.10. Clearly, these regions are not well resolved by MLT, especially the region where the O- and C-shells are merging.

1.4.2 3D Simulations of Convective O-Shell Burning and C-Shell Entrainment

Multidimensional hydrodynamic simulations have been done of O-shell burning and C-shell entrainment in massive stars. Bazan and Arnett (1994) performed a 2D simulation of O-burning where they show that the convective motions and temperature are non-radially, spherically asymmetric and mix through radiative layers by a penetrative convection rather than a simple overshoot.

Meakin and Arnett (2006) performed a 2D simulation of both the O- and C-burning shells with a limited nuclear network and compared to a 3D simulation of just the O-shell. They found that the non-convective region between the two shells had comparable velocities to the convective shells and that the convective shells have large, round vortices and asymmetric density perturbations. Additionally, they found that the convective motions excited waves

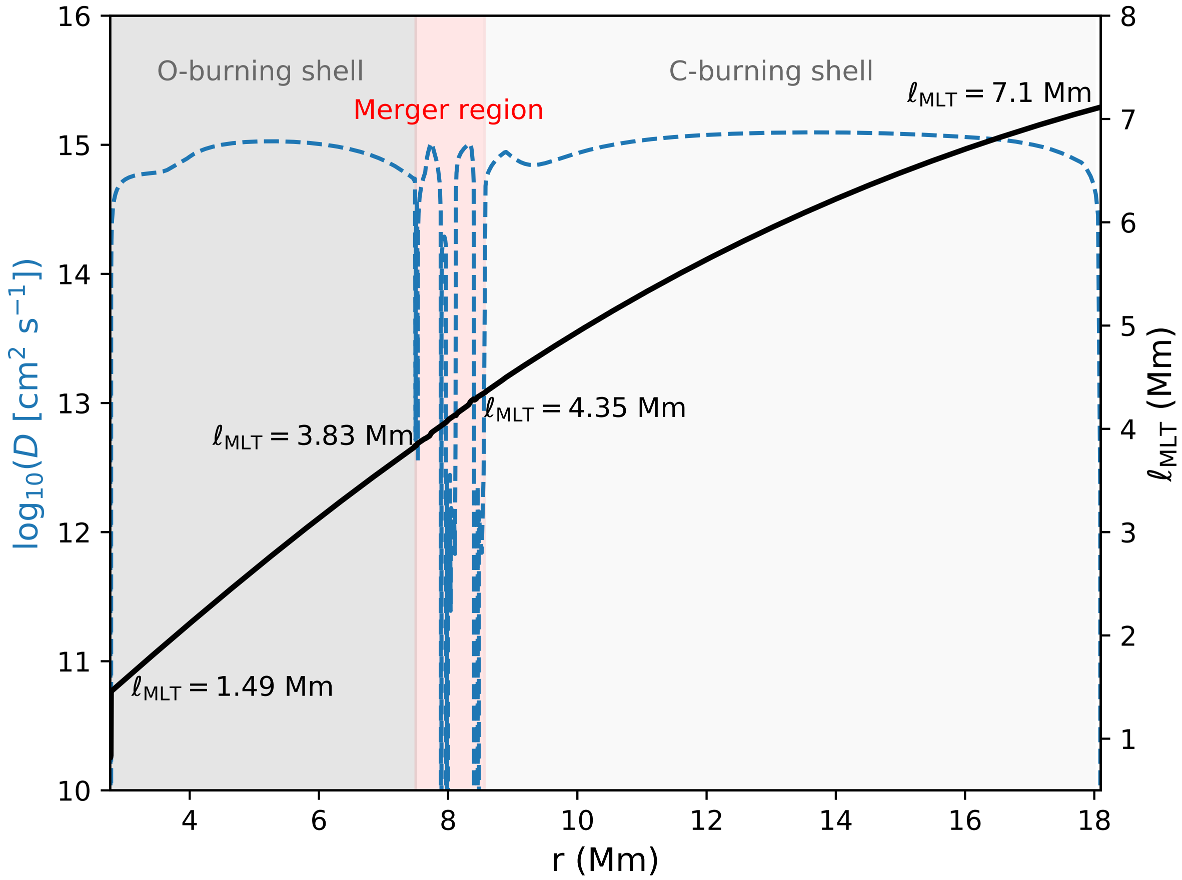

Figure 1.10: O- and C-burning shells in the $15\mathrm{M}_{\odot}$ $Z = 0.02$ model from Ritter et al. (2018b) at model number 9200 right before the merger with the C-shell is fully realized. The left y-axis shows the diffusion coefficient in blue, and the right y-axis shows the mixing length in black. The O-shell is from $(2.79-7.49)\times10^6$ m, the merger region is from $(7.49-8.56)\times10^6$ m, and the C-burning shell is from $(8.56-18)\times10^6$ m.

in the radiative layer that allowed for C-shell entrainment into the O-shell at $\sim 10^{-4}\ \mathrm{M}_{\odot}\mathrm{s}^{-1}$. Because of this entrainment, they found there would be sudden O-flames burning in the O-shell that would turn on and off. However, they note that their 3D O-shell simulation show plumes rather than vortices to describe the flow and caution against using 2D simulations to describe the convective motions in this scenario.

Meakin and Arnett (2007) also find this mixing difference between 2D and 3D simulation of O-shells, and they also find that the 3D radial velocity decreases gradually at the top of the shell and sharply at the bottom, which cannot be explained by a constant $\alpha_{\rm MLT}$. This is explained by the distance to the convective boundary acting as an upper limit to the mixing length, as fluid elements cannot travel a full mixing length if the remaining space they have is less than it. They also find turbulent entrainment of material from the stable layer above the O-shell.

Jones et al. (2017) in their 3D simulation of O-shell burning find that the 3D radial velocity profile exhibits the same gradual decrease at the upper boundary and find an entrainment from the stable layer of 1.33×10^{-6} $M_{\odot}s^{-1}$.

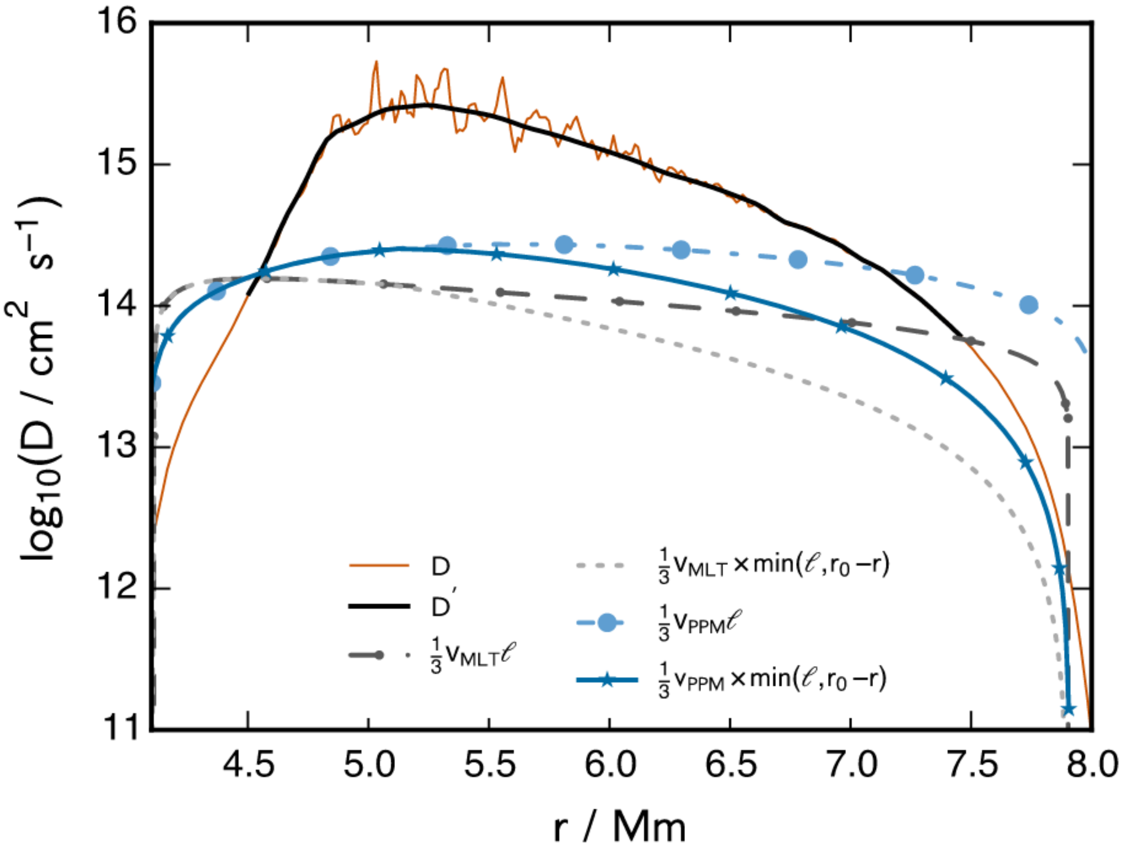

Figure 1.11: Taken from Jones et al. (2017): Time-averaged radial diffusion coefficient profile calculated from the spherically averaged abundance profiles by the method described in Section 3.5 (brown solid line; black solid line is a fit to the noisy region). The convective velocities computing using MLT agree with the spherically averaged 3D velocities to within about a factor of 2 inside the convection zone but are too large in the vicinity of the convective boundary, resulting in an overestimation of the diffusion coefficient there. Limiting the mixing length to the distance from the convective boundary reproduces the fall-off of the diffusion coefficient inside the convection zone approaching the boundary which is seen in the spherically averaged 3D simulation results.

As they show in Figure 1.11, the diffusion coefficient from MLT does not match the shape of what is estimated in 3D and underestimate velocities. However, they provide a recommendation for 1D modelling to better match the 3D diffusion profile shape:

$$D = v_{\mathrm{MLT}} \times \min(\alpha H_{\mathrm{P}}, |r - r_{\mathrm{SC}}|) \tag{1.22}$$

where $\alpha H_{\mathrm{P}} = \ell$ is the mixing length, r is the radius in the convective region, r_{SC} is the distance to the convective boundary, and v_{MLT} are the velocities predicted by MLT. This is rooted in the same insight by Meakin and Arnett (2007) that fluid elements may be too close to the convective boundary to move a full mixing length. In addition to this, they apply the same insight of distance to convective boundary to convective overshooting and find good agreement with the spherically average 3D diffusion coefficient.

Arnett et al. (2019) follows the critiques of Renzini (1987) by listing the many issues with the assumptions made by MLT and comparing the results of 3D hydrodynamic simulations to MLT. Among other things, they find that 3D simulations have a gradual decrease in the radial velocity profile as it reaches the bottom of their shell, and that there is entrainment of material from the stable layers. These are behaviours which cannot be captured by MLT.

Yadav et al. (2020) in their 3D simulation of an O-Ne shell merger find that 3D simulations have much faster convective velocities than predicted in 1D, and as the Ne-shell merges strong plumes carry the material to the bottom of the O-shell where burn in a convective-reactive environment. The asymmetric plume distribution leads to local hotspots of burning causing as difference in the Si, O, and Ne mass fractions when compared to 1D.

Andrassy et al. (2020) performed 3D simulation of C-ingestion into a convective O-shell and found a range of possible ingestion rates from 9.5×10^{-8} $\mathrm{M_\odot s^{-1}}$ to 1.18×10^{-4} $\mathrm{M_\odot s^{-1}}$ and convective velocities of 38 km $\mathrm{s^{-1}}$ to 181 km $\mathrm{s^{-1}}$ depending on the luminosity of the $^{12}\mathrm{C} +^{12}\mathrm{C}$, $^{16}\mathrm{O} +^{16}\mathrm{O}$, and $^{12}\mathrm{C} +^{16}\mathrm{O}$ reactions. In their simulations they find large scale asymmetries in the luminosity and density during entrainment. The radial velocity profile they find exhibits a gradual decline at the top of the O-shell, but also a less steep decline at the bottom of the shell. In addition to this, they boost the energy of C-burning and find large scale asymmetric oscillations like the Global Oscillation of Shell H-ingestion (GOSH) as found in Herwig et al. (2014). These are events where a sudden ingestion of hydrogen into a helium-rich convective shell. GOSHs can lead to increased entrainment of material, but also quench convective motions due to the energy feedback from the burning.

Rizzuti et al. (2024a) performed a 3D hydrodynamic simulation of an O-C shell merger with a limited nuclear network and find significant differences from their 1D model. In the

1D model, the top convective boundary of the O-shell grows until it merges with the Ne/C-shell above it, but in the 3D simulation the bottom of the C-shell grows until it merges with the Ne and O-shells under it. Like Jones et al. (2017), they find that 1D convective velocities are an order of magnitude lower than the 3D simulation. Because of the differences in 1D and 3D they find that there are significant differences in the mass fraction of species like ^{20}Ne, ^{24}Mg, and ^{28}Si.

1.4.3 1D Implementation of 3D Hydrodynamics

Despite the limitations of 1D stellar evolution, 3D hydrodynamic codes are unable to calculate the nucleosynthesis for complex processes such as the γ-process where thousands of isotopes can be involved. Nucleosynthetic yields have to be calculated then in 1D, but the limitations of 1D can be mitigated by adopting the results of 3D hydrodynamics and testing a variety of mixing scenarios. Specific to O-shell burning in O-C shell mergers, the following steps can be taken to investigate in 1D how macrophysical uncertainties impact nucleosynthesis:

- The shape of the radially averaged 3D diffusion coefficient profile exhibits a downturn at the boundaries of the O-shell that is not seen in 1D (Meakin and Arnett, 2007; Jones et al., 2017).

- Convective velocities are higher in 3D hydrodynamic simulations than predicted by mixing length theory (Jones et al., 2017; Rizzuti et al., 2024a).

- The entrainment rate of C-shell material into the O-shell could be anywhere from 10^{-8} M$_\odot$s^{-1} to 10^{-4} M$_\odot$s^{-1} (Andrassy et al., 2020).

- Asymmetric non-radial instabilities are present due to energy feedback which could lead to convective quenching (Andrassy et al., 2020).

To address the shape a gradual downturn to $D_{\rm conv}$ Equation 1.14 from Jones et al. (2017) is adopted, but at the bottom of the O-shell instead of the top. This is done because we are simulating the nucleosynthesis during an O-C shell merger, and so the upper convective boundary is already connected to the C-shell above. To address lower convective velocities in 1D, a series of boost factors can be applied to the diffusion coefficient. To address the variability of C-shell entrainment, a variety of entrainment rates can be adopted in a 1D post-processed model. Finally, to address energy feedback such as the GOSH-like events seen in Andrassy et al. (2020), a simple dip in the convective profile can be adopted:

$$D_{\mathrm{dip}} = D_{\mathrm{MLT}} - (D_{\mathrm{MLT}} - c) \times \exp\left[-\frac{(r-a)^2}{w^2}\right] \tag{1.23}$$

where c is the depth of the dip, a is the centre of the dip, w is width of the dip, and r is the radius in the region. All variables are in 10^6 m. Using the results of 3D hydrodynamic simulations, we can explore the possible impact on nucleosynthesis from macrophysics.

1.5 Thesis Outline

As explained in Section 1.4.1, 1D stellar evolution models are limited during the late stages of stellar evolution, particularly during the O-C shell merger. This poses a problem for understanding the nucleosynthesis of isotopes produced during this merger because the O-shell is a convective-reactive environment as explored in Section 1.3.4. If the convective velocities are higher in the O-shell, this would decrease the mixing timescale and could change how the nucleosynthesis occurs. This is particularly important for understanding the p nuclei, as models with O-C shell mergers strongly contribute to their production as explained in Section 1.2.6. This thesis will explore the importance of macrophysical uncertainties during convective-reactive nucleosynthesis in the O-shell by implementing 3D hydrodynamic insights into 1D stellar evolution models.

Chapter 2: Impact of 3D-macrophysics and nuclear physics on p-nuclei nucleosynthesis in O-C shell mergers

In Chapter 2, I describe the impact of a 1D implementation of 3D hydrodynamic concerns on the production of the p nuclei. I explore how the nature of convective-reactive affects the nucleosynthesis of the p nuclei, how the mixing concerns mentioned in Section 1.4.3. In addition to this, I present the results of a nuclear reaction correlation study and investigate how the results of these correlation studies change depending on the mixing conditions in the O-shell.

Chapter 3: Additional Work

In Chapter 3, I describe how this work can continue to be applied to the production of the light odd-Z isotopes. In particular, I highlight how the isotopes ^{39}K, ^{40}K, and ^{41}K are impacted by these macrophysical uncertainties. This has relevance to whether exoplanets could form habitable atmospheres, as the decay of the radionuclide ^{40}K is a significant heating source in early planet formation (Frank et al., 2014; O'Neill et al., 2020). I also provide some preliminary work investigating whether advective-reactive nucleosynthesis matters for the r-process in the post-processing of trajectories that have escaped a black hole.

Chapter 2

Impact of 3D-macrophysics and nuclear physics on p-nuclei nucleosynthesis in O–C shell mergers

The following work has been written and prepared for submission to peer-review (Issa et al., 2025). This paper was written in collaboration with my supervisor Dr. Falk Herwig, Dr. Pavel Denissenkov, and Dr. Marco Pignatari. Drs. Herwig and Pignatari provided comments on the manuscript and editing feedback. Dr. Denissenkov supplied the initial code used to create the post-processed models, analysis tools, and training necessary to understand how to use the code. I have modified this code and created new tools to perform the analysis, but his contributions were essential to the inital stages. Dr. Herwig has also provided guidance and support throughout the project in his role as my supervisor.

2.1 Abstract

O-C shell mergers in massive stars are a site for producing the p nuclei by the γ process, but 1D stellar models rely on mixing length theory, which does not match the radial velocity profiles of 3D hydrodynamic simulations. We investigate how 3D macro physics informed mixing impacts the nucleosynthesis of p nuclei. We post-process the O-shell of the $M_{\mathrm{ZAMS}} = 15\ \mathrm{M}_{\odot}$, $Z = 0.02$ model from the NuGrid stellar data set. Applying a downturn to velocities at the boundary and increasing velocities across the shell as obtained in previous results, we find non-linear, non-monotonic increase in p-nuclei production with a spread of 0.96 dex, and find that isotopic ratios can change. Reducing C-shell ingestion rates as found in 3D simulations suppresses production, with spreads of $1.22-1.84$ dex across MLT and downturn scenarios. Applying dips to the diffusion profile to mimic quenching events also suppresses production, with a 0.51 dex spread. We analyze the impact of varying all photo-disintegration rates of unstable n-deficient isotopes from Se–Po by a factor of 10 up and down. The nuclear physics variations for the MLT and downturn cases have a spread of $0.56-0.78$ dex. We

also provide which reaction rates are correlated with the p nuclei, and find few correlations shared between mixing scenarios. Our results demonstrate that uncertainties in mixing arising from uncertain 3D macro physics are as significant as nuclear physics and are crucial for understanding p-nuclei production during O-C shell mergers quantitatively.

2.2 Introduction

The origin of the solar pattern of the 35 stable p nuclei is a long-standing problem for understanding nucleosynthesis. Burbidge et al. (1957) first identified these isotopes as a distinct group, produced primarily not by the s or r process, but instead by a p process through (p, γ), (γ, p), and (γ, n) reactions occurring during Type II supernovae and possibly Type I supernovae. Based on the first generations of stellar computational models, Arnould (1976) found that the p process could be driven by all photo-disintegration reactions (γ, n), (γ, α) and (γ, p) during the most advanced evolutionary stages of massive stars. Woosley and Howard (1978) found instead that these photo-disintegrations could create the distribution of p-process nuclei during the passage of the supernova shock over the internal progenitor structure, which they called the γ process. Following works better defined γ process production in Type II supernovae and more in general in core-collapse supernovae (CCSNe e.g., Prantzos et al., 1990; Rayet et al., 1995; Travaglio et al., 2018; Choplin et al., 2022; Roberti et al., 2023, 2024).

A variety of additional processes and astrophysical sites have been discussed, and no single mechanism produces all the p nuclei. Woosley and Hoffman (1992) found that ^{74}Se–^{92}Mo could be produced during the α-rich freezeout of a supernova. Fröhlich et al. (2006) found high neutrino fluxes during a supernova can create ^{74}Se–^{108}Cd by (n, p), (n, γ), and (p, γ) reactions in a νp process. Schatz et al. (1998) suggested that a hydrogen-rich accretion disk around a neutron star could undergo a series of rapid proton captures in a rp process to produce ^{74}Se–^{98}Ru. Xiong et al. (2024) proposed that neutrino induced reactions of r-process material in a νr process could produce ^{78}Kr–^{138}La in the winds of a proto-neutron star. Goriely et al. (2002) proposed that a proton-poor and neutron boosted region could undergo proton-captures could produce all p nuclei by a pn process during He-detonation of a C-O white dwarf's ejected envelope. Rauscher et al. (2002) found that the γ process can produce the p nuclei in massive stars during core-collapse supernovae, and also beforehand if the O shell merges with the C shell, but that the γ process underproduces ^{92,94}Mo and ^{96,98}Ru. Ritter et al. (2018a) and Roberti et al. (2023) confirmed these results and studied the p process triggered by O-C shell merger.

The γ process describes the flow of (γ, n), (γ, p), and (γ, α) reactions on the stable isotopic seeds that are already present in the shell at temperatures of $T = (1.5\text{–}3) \times 10^9$ K (Rauscher et al., 2013). However, the γ process in massive stars underproduces not only the Mo and Ru, but all p nuclei with $A = 90\text{–}130$ (Arnould and Goriely, 2003; Woosley and Heger, 2007). Travaglio et al. (2011) showed that the γ process could produce all p nuclei during a Type Ia supernova from the s-process material synthesized during stellar evolution without the underproduction of ^{92,94}Mo and ^{96,98}Ru. Furthermore, Travaglio et al. (2015) found that modifying the distribution of s-process material significantly influenced the production of the p nuclei, especially the heaviest ones, and that the lightest three were strongly dependent on the metallicity. Battino et al. (2020) additionally found that the H-flashes of rapidly accreting white dwarfs which undergo the i process could modify the seed distribution to produce p nuclei with $96 < A < 196$ by the γ process during the subsequent SNIa.

Since the first isotopic classification made by Burbidge et al. (1957), it has been found that not all p nuclei in the solar abundance pattern are produced by a single process. Bisterzo et al. (2011) state that ^{152}Gd, ^{164}Er, and ^{180}Ta have significant contributions of 70.5%, 75.5%, and 74.5% from the s process. Dillmann et al. (2008) found that ^{113}In and ^{115}Sn are made by β-decays after the r process through isomeric states. Goriely et al. (2001) argue that (γ, n) was too weak to produce ^{138}La, and instead that it is made by ν_e-capture on ^{138}Ba during the CCSN, and Arnould and Goriely (2003) similarly say that $^{180\mathrm{m}}$Ta could also have ν-induced contributions. Sieverding et al. (2018) also found that the ν-process is important for the nucleosynthesis of ^{113}In, ^{138}La, and $^{180\mathrm{m}}$Ta.

The O-shell where p nuclei are produced during a merger is a convective-reactive environment where mixing and nuclear burning timescales are equal (Ritter et al., 2018a; Yadav et al., 2020). If there is significant energy released the flow can be modified (Dimotakis, 2005), such as H-ingestion into He-burning shell (Herwig et al., 2011, 2014) or O-C shell mergers causing violent mixing (Andrassy et al., 2020; Yadav et al., 2020). The Damköhler number (Dimotakis, 2005) quantifies the ratio of these timescales and is defined as:

$$D_\alpha \equiv \frac{\tau_{\mathrm{mix}}}{\tau_{\mathrm{react}}} \tag{2.1}$$

where τ_{mix} is the mixing timescale and τ_{react} is the nuclear reaction timescale. Convective regions where the mixing timescale is much faster than the nuclear burning timescale have $D_\alpha \ll 1$, and species are well-mixed across the region. Convective-reactive regions where timescales are equal have $D_\alpha \sim 1$, and species can either react at a location or advect to another location and react with the material there, and as a consequence are not well-mixed.

The mixing and reaction timescales can be given by:

$$\tau_{\rm mix} = \frac{\ell^2}{D_{\rm MLT}}; \quad \tau_{\rm react} = \frac{1}{\rho N_A \langle \sigma v \rangle Y_j} \tag{2.2}$$

where ℓ is the mixing length, $D_{\rm MLT}$ is the mixing diffusion coefficient, ρ is the local density, N_A is Avogadro's number, $\langle \sigma v \rangle$ is the thermally averaged reaction rate, and Y_j is the molar abundance of the interacting species. The diffusion coefficient is $D_{\rm MLT} = \frac{1}{3} v_{\rm MLT} \cdot \ell$, where $v_{\rm MLT}$ is the convective velocity and the mixing length is $\ell = \alpha \cdot H_p$ where H_p is the pressure scale height and α is a free parameter (Joyce and Tayar, 2023).

Existing massive star models that calculate p-nuclei nucleosynthesis are 1D and rely on mixing length theory (MLT) to describe convection. However, multi-dimensional hydrodynamic simulations of convective O-shell burning predict higher convective velocities than MLT and show a gradual downturn in the mixing efficiency profile at shell boundaries (Meakin and Arnett, 2007; Jones et al., 2017). 3D simulations reveal features absent in 1D, such as asymmetric nuclear burning (Bazan and Arnett, 1994; Yadav et al., 2020), large-scale non-radial density asymmetries, and potentially lower C-shell ingestion rates during O-Ne-C shell mergers (Andrassy et al., 2020; Yadav et al., 2020). In 1D models like those from Ritter et al. (2018b), O-C shell mergers occur because the upper boundary of the O-shell entrains ^{12}C and ^{20}Ne as it burns, flattening the entropy gradient. In contrast, 3D simulations by Rizzuti et al. (2024a) find the lower boundary of the C-shell extending downward and engulfing the O-shell. Similarly, Yadav et al. (2020) show that entropy generation in nuclear burning hotspots within the Ne-shell leads to downdrafts that raise the entropy in the O-shell. Dynamic behaviour shortly before the core collapse for these supernova progenitors late in their evolution are not captured in 1D (Arnett and Meakin, 2011; Müller, 2016; Yadav et al., 2020). While 3D hydrodynamic simulations may not be solving all relevant equations, such as a robust nuclear network, 1D models fundamentally fail to represent the non-radial mixing and spherically asymmetric instabilities during O-C shell mergers (Meakin and Arnett, 2006; Andrassy et al., 2020; Yadav et al., 2020).

This has consequences for p-nuclei production. Nuclei with $A > 110$ are primarily synthesized during the merger, not during explosive burning, regardless of the peak CCSN energy (Roberti et al., 2023, 2024). To explore the impact of the macrophysical uncertainties in the O-shell during a merger, we adopt a 3D hydrodynamic inspired set of modified radial mixing profiles and ingestion rates to determine the impact of mixing on the γ process. We will also explore how varying the nuclear reaction rates impact the nucleosynthesis of the p nuclei as the O-shell is a convective-reactive environment.

Section 2.3 describes the post-processing of the Ritter et al. (2018b) model using 3D hydrodynamic-inspired mixing profiles and assesses the impact of varying nuclear reaction rates. Section 2.4.1 examines how the convective-reactive environment produces the p nuclei and the role of C-shell ingestion. Sections 2.4.2–2.4.4 explore how 3D hydrodynamic insights affect p nuclei production: 2.4.2 analyzes the impact of downturns and boosted velocities in the O-shell, 2.4.3 investigates reduced C-shell ingestion, and 2.4.4 evaluates dips in the mixing efficiency due to quenching. Section 2.4.5 presents the sensitivity to nuclear rates, their correlation with p nuclei, and their relation to mixing profiles and velocities. Finally, Section 2.5 summarizes our findings and their implications.

2.3 Methodology

2.3.1 Initial Model and Post-Processing Setup

We post-process the $M_{\rm ZAMS} = 15\ {\rm M}_\odot$, $Z = 0.02$ massive stellar model from the NuGrid data set (Ritter et al., 2018b). The 1D stellar model was computed with `MESA` (Paxton et al., 2010) without rotation and convective boundary mixing is treated using an exponential-diffusive prescription (Freytag et al., 1996; Herwig, 2000) with an overshoot parameter of $f = 0.022$ at all boundaries except at the base of convective shells where $f = 0.005$ until the end of core He burning, after which $f = 0$. This model has a merger of its convective O and C-burning shells late in its evolution as shown in Figure 2.1. During this merger, the C-burning ashes and stable isotopic material are ingested into the much hotter O-burning shell.

The detailed nucleosynthesis is calculated with the 1D multi-zone post-processing code `mppnp` (Pignatari et al., 2016b). `mppnp` is a multi-zone post-processing code that uses stellar structure calculated by stellar evolution codes to calculate the full nucleosynthesis of a stellar model. `mppnp` treats mixing, nuclear burning, and ingestion separately rather than the coupled treatment by a code like `MESA` (Paxton et al., 2010). A convergence test was performed by decreasing the timesteps and increasing the number of mass zones. It found that a timestep of $\Delta t = 0.01$ s and 400 equidistant mass zones with 4 additional zones at the bottom of the O-shell were sufficient to resolve both the burning and mixing timescales with a decreasing mixing efficiency profile. Calculations initially used a 5234 isotope network, but many n-rich species were unnecessary. A network of only the necessary 1470 isotopes was adopted, focusing on the n-deficient isotopes, for faster calculations. Isomeric states were not included in this network so $^{180\rm m}$Ta is not calculated. A single simulation costs approximately 8 hours on 40 cores, for a total of 274 core years for this work.

The `mppnp` code calculates both the undecayed mass fraction as a function of mass and

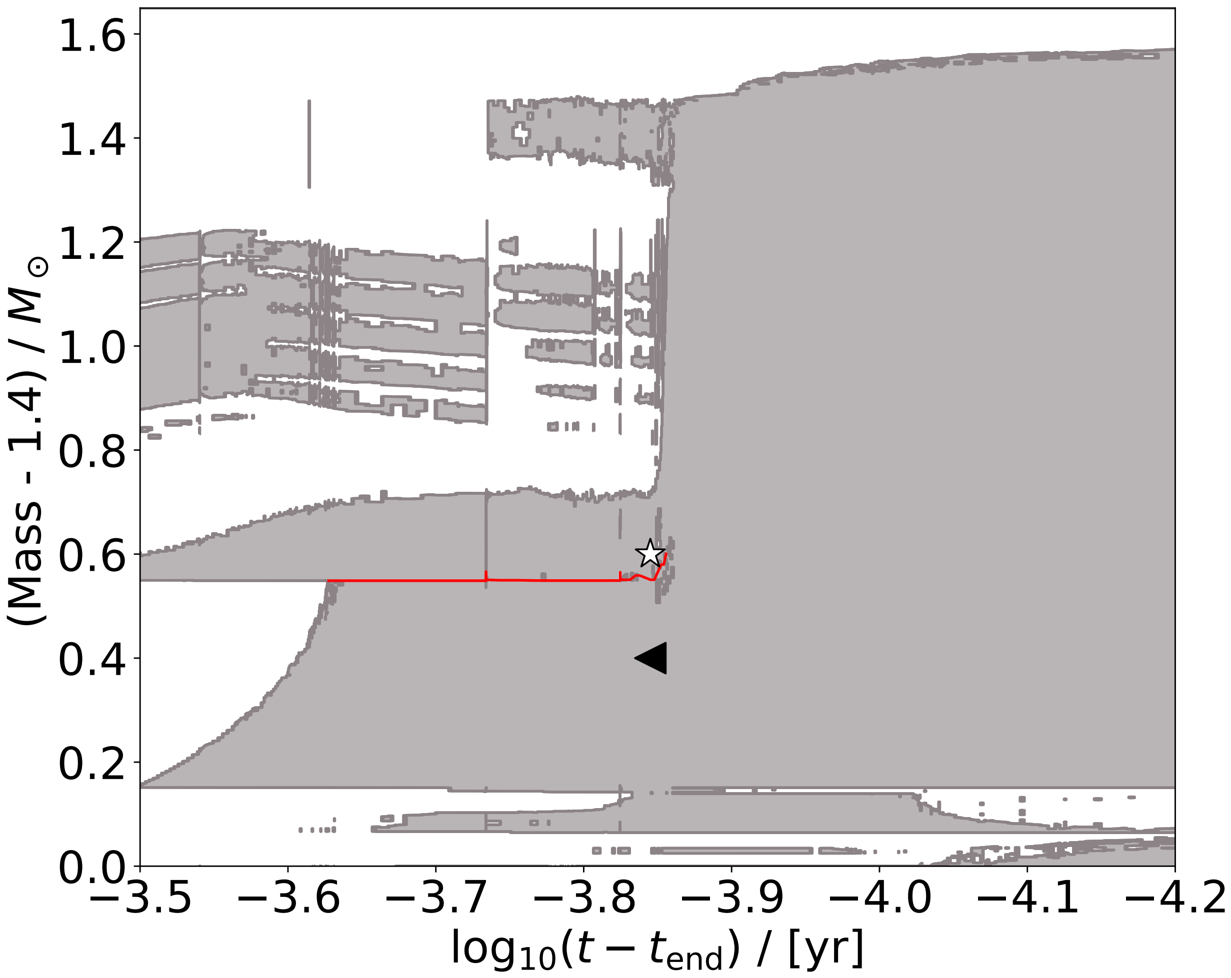

Figure 2.1: Kippenhahn diagram showing the merger of the convective O and Cburning shells. The Oburning shell extends from 1.55 $M_\odot$ to 1.95 $M_\odot$, and the first ingested Cburning shell from 1.96 $M_\odot$ to 2.11 $M_\odot$. A red guideline has been provided to mark the thin radiative layer separating the O and C-shell. Other convective regions are also Cburning shells. The merger onsets at $\log_{10}(t - t_{\rm end})/{\rm yr} \approx -3.85$ and reaches full extent at ≈ -4. A black triangle marks where the initial composition is taken from and a white star marks the location where the ingested C-shell material is taken from for this study.

the mass-averaged contribubtions from radiogenic decay at a temperature of $T = 100$ MK without explosive contributions. The mass fraction X_i of species i is defined as the ratio of the mass of that species to the total mass of the stellar material, such that $\sum_i X_i = 1$ for all isotopes.

To analyze the impact of macrophysical uncertainties and varying the nuclear reaction rates during the merger, isotopic mass fractions are taken just before the onset of merger at $\log_{10}(t - t_{\rm end})/{\rm yr} = -3.845$ from $m = 1.8$ $M_\odot$, and the ingested C-shell material is taken from $m = 2.0$ $\mathrm{M}_{\odot}$ at the same time, as shown in Figures 2.1 and 2.2. Earlier in the model, there is some p-nuclei production in the first convective O-shell, which extends from 1.55 $\mathrm{M}_{\odot}$ to 1.95 $\mathrm{M}_{\odot}$ during $\log_{10}(t - t_{\mathrm{end}})/\mathrm{yr} = -1.76$ to -2.16. These nuclei are not processed by any further burning before the merger.

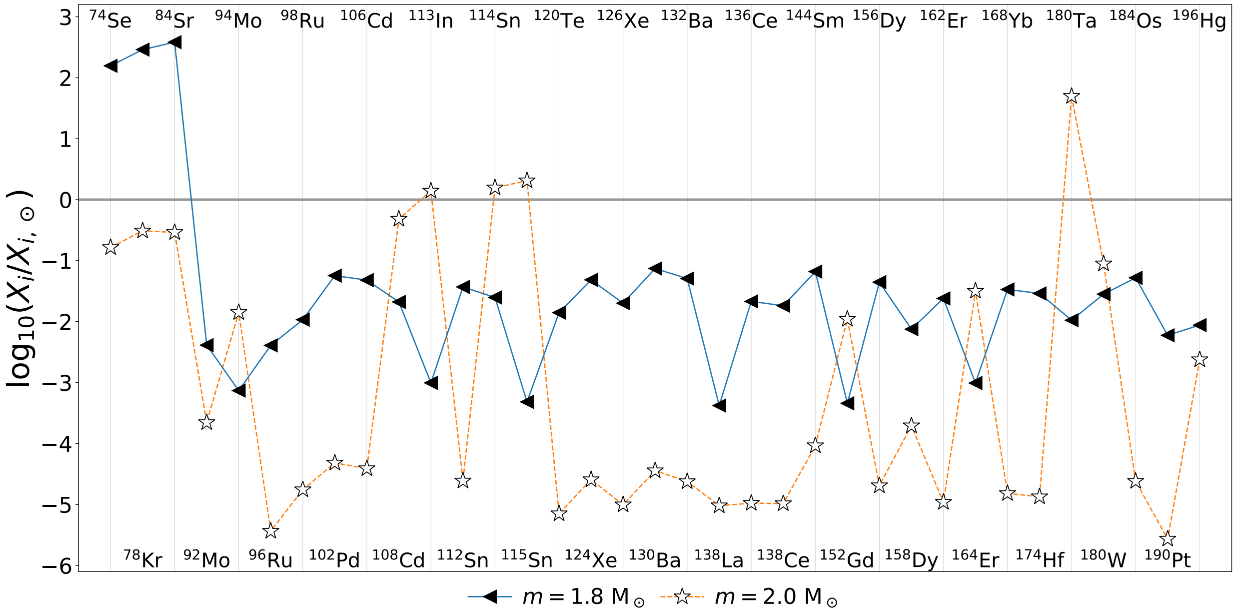

Figure 2.2: Logarithmic ratio to solar value for the p nuclei from $\log_{10}(t - t_{\mathrm{end}})/\mathrm{yr} = -3.856$ used for initial O-shell composition and ingested C-shell material. The solar values are taken from Lodders et al. (2009) and the grey line at zero is equal to the solar value. Markers are the same as Figure 2.1.

The results are presented in terms of an overproduction OP compared to the initial composition:

$$\mathrm{OP} = \log_{10}\left(\frac{X_f}{X_i}\right) \tag{2.3}$$

where X_f is the final mass-averaged decayed mass fraction of a species in the O-shell and X_i is the inital mass fraction. The average overproduction factor is calculated as the arithmetic mean of OP:

$$\langle \mathrm{OP} \rangle = \frac{1}{N}\sum_{i}^{N} \mathrm{OP}_i \tag{2.4}$$

where N is the number of p nuclei.

The stellar structure used is from the onset of the merger at $\log_{10}(t - t_{\mathrm{end}})/\mathrm{yr} = -3.856$ and to clearly analyze the impact of mixing alone, the stellar structure is kept constant. Although the structure is not static in the model, the change to the temperature, density, and entropy between the initial composition and where we take the structure from is less than 5% during those 110 s. The merger at $\log_{10}(t-t_{\rm end})/{\rm yr} = -3.856$ is not fully developed, but MLT cannot accurately describe this region as the mixing length ℓ is too large (Renzini, 1987; Arnett et al., 2019). Because of this, the mixing efficiency profile is smoothed at the top as shown in Figure 2.3 to simulate a full merger.

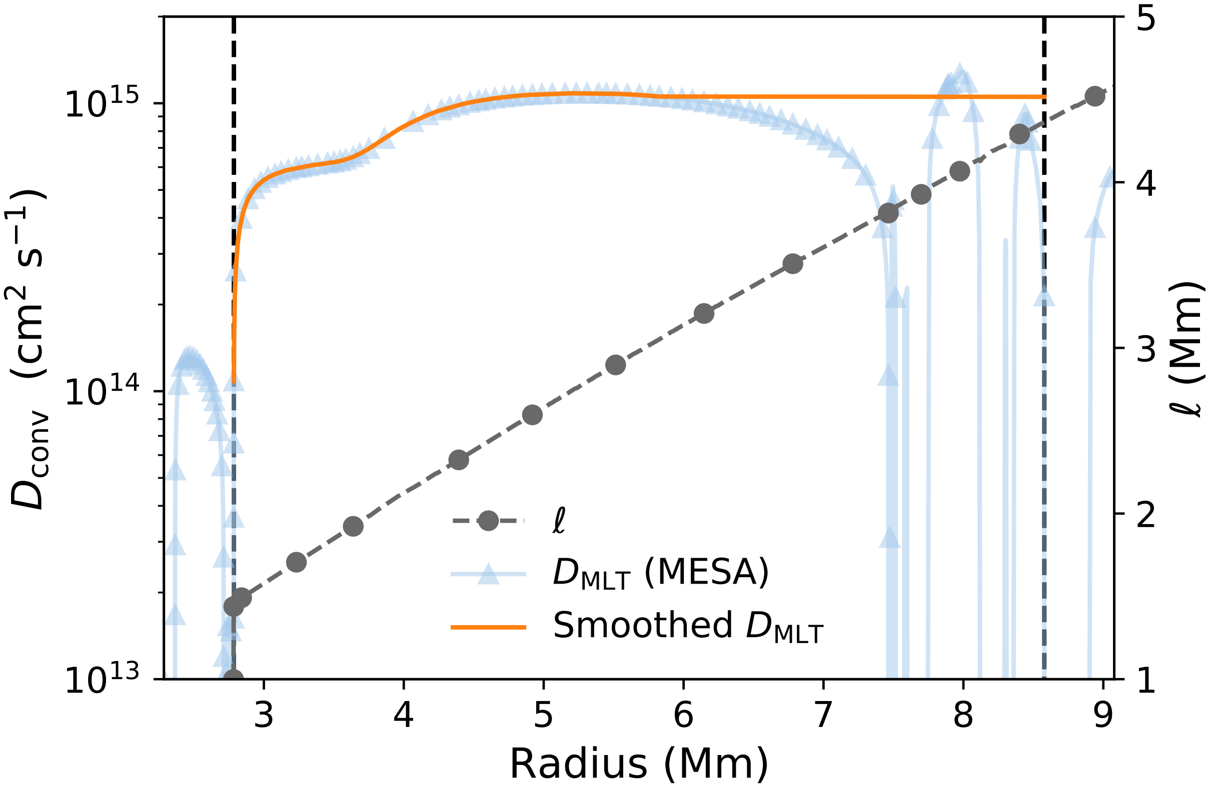

Figure 2.3: The diffusion coefficient profile and mixing length at model number 9200 for the $M_{\rm ZAMS} = 15\ {\rm M}_\odot$, $Z = 0.02$ model. The light blue line is D from MESA, the orange line the smoothed D used for the MLT mixing scenario in this paper, and the grey line is the mixing length. Black dashed lines mark the shell boundaries for this paper.

2.3.2 1D implementation of 3D macrophysics

MLT predictions of the radial mixing efficiency profile deviate from the more realistic predictions from 3D simulations. 3D convective O-burning simulations show that the radial convective velocity profile gradually decreases near the shell boundary, in contrast to MLT predictions of a stiff boundary (Meakin and Arnett, 2007; Jones et al., 2017). This downturn is seen at both the bottom and top of convective shells (Herwig et al., 2006; Meakin and

Arnett, 2007; Jones et al., 2017). The decrease occurs because mixing is driven by convective plumes in these simulations, rather than the idealized convective blobs in MLT. Plumes exhibit strong radial velocities in the interior of the convective region but lose their radial component as they reach the boundary, while non-radial velocity components increase. This behavior contrasts with MLT, which predicts a sharp drop to zero velocity at the boundary. Using Equation 4 from Jones et al. (2017), the downturn to the mixing efficiency profile can be implemented in 1D:

$$D_{\text{3D-insp.}} = \frac{1}{3} v_{\text{MLT}} \times \min\left(\ell, r - r_0\right) \tag{2.5}$$

where ℓ is the mixing length, r_0 is the Schwarzschild boundary at the bottom of the O-shell, and an additional factor of 1/3 is applied to match the MLT diffusion coefficient at the top of the shell.

MLT also underpredicts the strength of the convective velocities in the O-shell. Jones et al. (2017) found that convective velocities are stronger by a factor of ~ 30 compared to MLT. Andrassy et al. (2020) in their 3D C-shell entrainment simulations show that their velocities could be up to ~ 5 times stronger than Jones et al. (2017) depending on the luminosity of C- and O-burning. It is possible the velocities could be even higher as these simulations do not include feedback from a nuclear network or treatment of radiation pressure (Jones et al., 2017; Andrassy et al., 2020). Rizzuti et al. (2024a) finds that velocities are boosted by a factor of ~ 10 due to the feedback from new reactions with the ingested material in their 3D O-C shell mergers. We implement this by applying a boost factor of 3×, 10×, and 50× to the convective velocities as shown in Figure 2.4.

The entrainment rate of C-shell material could be lower during the merger depending on the strength of burning (Jones et al., 2017; Andrassy et al., 2020). To investigate the impact of this, a range of rates are considered: $4 \times 10^{-5}\ \mathrm{M_\odot s^{-1}}$, $4 \times 10^{-4}\ \mathrm{M_\odot s^{-1}}$, $4 \times 10^{-3}\ \mathrm{M_\odot s^{-1}}$, and a scenario with no entrainment. The maximum mass of the convective C-shell in our model is $0.8\ \mathrm{M_\odot}$, so for 110 s of merging the maximum possible entrainment rate would be $7 \times 10^{-3}\ \mathrm{M_\odot s^{-1}}$ similar to Ritter et al. (2018a).

1D and 3D simulations show that the convective profile can be quenched as material is ingested as entropy changes due to entrainment and burning (Iben, 1975; Sackmann et al., 1974; Herwig et al., 1999; Miller Bertolami et al., 2006; Herwig et al., 2011, 2014). As an example, during H-ingestion into a He-shell, the energy feedback from the ingested material could cause a split in the convective profile with very small amount of entrainment (Herwig et al., 2011). Herwig et al. (2014) found this effect could decrease the radial velocity profile and reduce the entrainment of species and labelled the event Global Oscillation of Shell

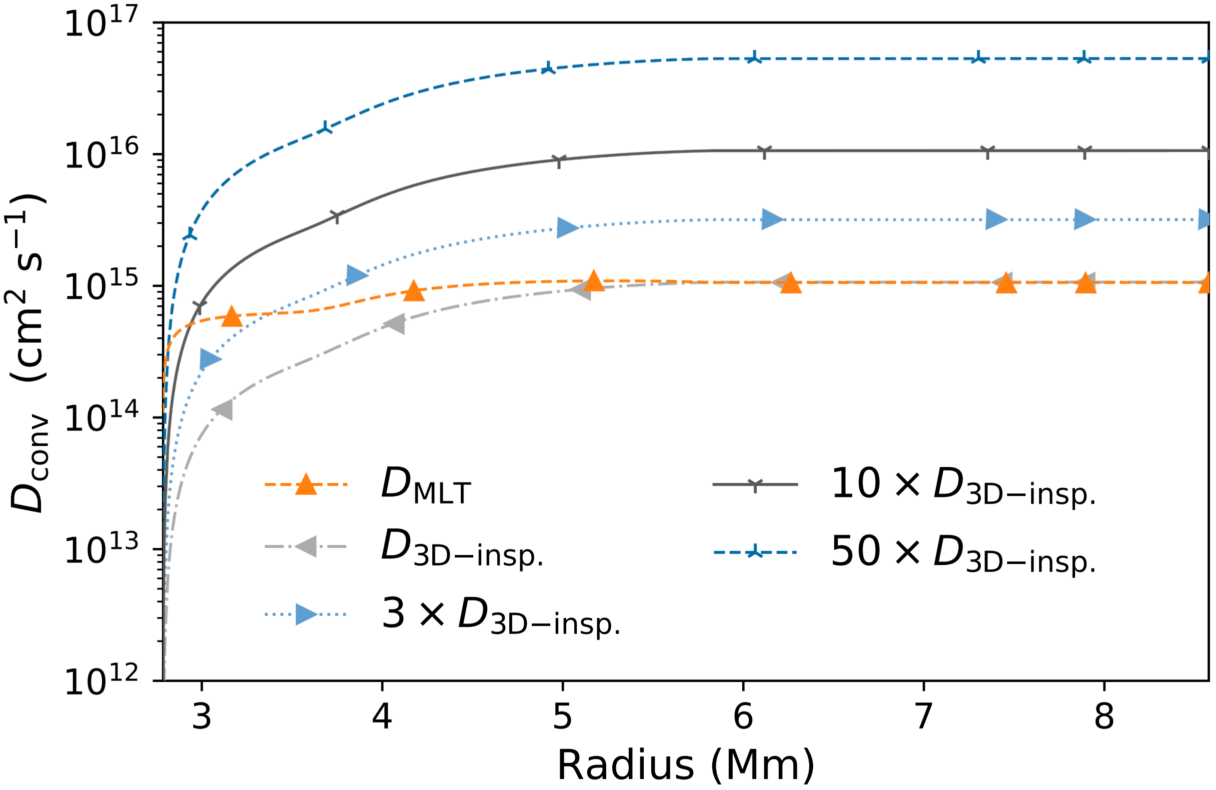

Figure 2.4: The diffusion coefficient profiles for the MLT and 3D-inspired gradual downturn scenarios. The dashed orange line is D_{MLT} and the dashed light grey line, dotted light blue line, solid grey line, and dashed dark blue line are the downturn profiles with boost factors of 1, 3, 10, and 50 respectively.

Hydrogen-Ingestion (GOSH). Similar effects during C-shell entrainment could be possible, as Andrassy et al. (2020) found that strong oscillatory modes like GOSHs were present in their 3D simulations. Energy feedback events like this could explain supernova observations (Smith and Arnett, 2014). There is no clear prescription for how to implement this effect into 1D models, but it is clear that there would be decreased mixing because of a split. To investigate a possible convective quenching, we consider a GOSH-like event and a partial merger, where a Gaussian dip (but not full split) occurs in the MLT diffusion profile:

$$D_{\mathrm{quench}} = D_{\mathrm{MLT}} - (D_{\mathrm{MLT}} - c) \times \exp\left[-\frac{(r-a)^2}{w^2}\right] \tag{2.6}$$

where c is the maximum extent of the dip, w is the width, and a is the center of the dip. The GOSH-like convective splitting could occur at the location where $D_\alpha = 1$ for a significant burning event (Herwig et al., 2011). We centre this event at $a = 4.95$ Mm at a location of probable energetic feedback could occur. The O-shell could partially merge with the C-shell due to feedback effects, so we consider a partial merger at $a = 7.5$ Mm where the unmerged MLT profile has a dip as seen in Figure 2.3. A width of $w = 0.25$ Mm is used for both scenarios, which is approximately the distance between the top of the O-shell and the convective bump above it in Figure 2.3. For both scenarios we consider a weaker dip to $c = 10^{14}$ cm^{2}s^{-1} and a stronger dip to $c = 10^{13}$ cm^{2}s^{-1} to investigate the impact on nucleosynthesis. The profiles for the GOSH-like and partial merger scenarios are shown in Figure 2.5.

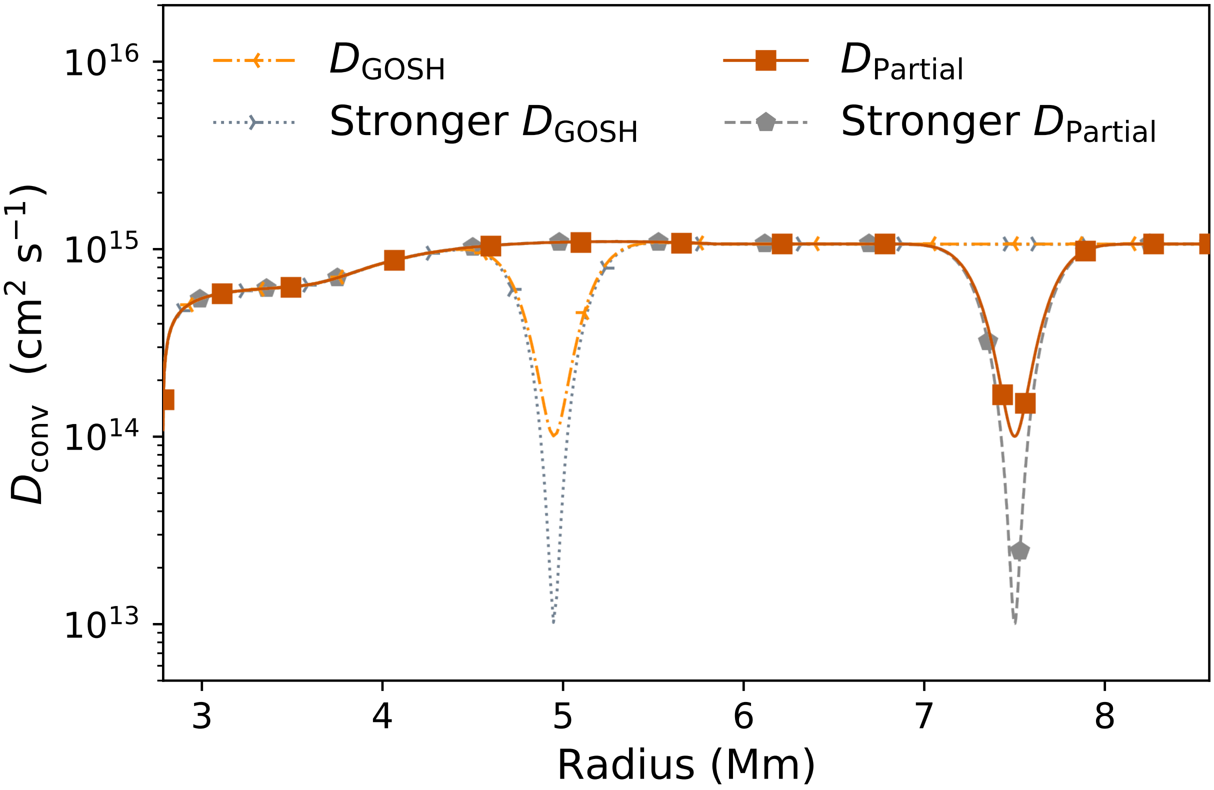

Figure 2.5: The quenched mixing scenario convective profiles. The dashed light orange line and dotted light grey line are the GOSH-like profiles with a dip centred at $r = 4.95$ Mm. The solid red line and dashed dark grey line are the partial merger profiles with a dip centred $r = 7.5$ Mm.

2.3.3 Determining impact of varying nuclear reactions

Many of the reactions involving the unstable n-deficient isotopes from Se to Po have not been measured experimentally and are determined by theoretical models, and the uncertainties of unmeasured reactions for unstable isotopes are much greater than for stable isotopes. To determine the impact of nuclear physics for the γ process, we vary our (γ, α), (γ, p), and (γ, n) photo-disintegration rates used by the NuGrid code (Pignatari et al., 2016b) for all unstable n-deficient isotopes from Se to Po by a random factor uniformly selected between 0.1 to 10 by a Monte Carlo method for 1000 cases. This applies the same approach used for (n, γ) rates during the i process developed by Denissenkov et al. (2018) and Denissenkov et al. (2021). This was done for the MLT and downturn mixing scenarios in Figure 2.4 with an ingestion rate of 4×10^{-3} $\mathrm{M_{\odot}s^{-1}}$. This approach also allows for the identification of reaction rates that are relevant for the production of an isotope using correlations. The Pearson coefficient describes correlations between $X/X_{\text{no variation}}$ and the variation factors where X is the final mass-averaged and decayed mass fraction for a Monte Carlo case and $X_{\text{no variation}}$ is the same for the default case where all variation factors are 1. All correlations with $|r_{\mathrm{P}}| \geq 0.15$ are reported in this study. In addition to the Pearson coefficient, a logarithmic slope ζ is also reported to determine the importance of a reaction on the final mass fraction of an isotope, which is discussed along with caveats about correlation rates in Appendix 2.6.1.

2.4 Results

An overview of our results in terms of overproduction factors and average spreads of overproduction factors is presented in Table 2.1.

Table 2.1: $\langle \mathrm{OP} \rangle$ for each mixing scenario and the average spread $(\mathrm{OP}_{\mathrm{max}} - \mathrm{OP}_{\mathrm{min}})$ for the Monte Carlo simulations for the p nuclei. All Monte Carlo simulations are calculated with an ingestion rate of 4×10^{-3} $\mathrm{M_{\odot}s^{-1}}$.

Scenario	No Ingestion	4×10^{-5} $\mathrm{M_{\odot}s^{-1}}$	4×10^{-4} $\mathrm{M_{\odot}s^{-1}}$	4×10^{-3} $\mathrm{M_{\odot}s^{-1}}$	MC Spread
MLT	−0.11	1.06	1.92	2.24	0.56
1× Downturn	0.05	1.12	1.98	2.58	0.59
3× Downturn	−0.23	1.28	2.18	2.83	0.69
10× Downturn	−1.23	1.18	2.10	2.89	0.76
50× Downturn	−5.47	0.88	1.81	2.72	0.79
GOSH-like	–	–	–	2.06	–
Stronger GOSH-like	–	–	–	1.78	–
Partial Merger	–	–	–	2.13	–
Stronger Partial Merger	–	–	–	1.91	–

2.4.1 Convective-reactive production of the p nuclei

Convective-reactive nucleosynthesis is characterized by a region where the timescales for advection and nuclear reactions are similar. In the γ process, heavier species are produced at cooler temperatures of 1.5–2 GK and are destroyed at higher temperatures, and lighter species are produced in temperatures up to 3.5 GK (Rauscher et al., 2013). Whether an isotope undergoes (γ, n) and (n, γ) reactions or contributes to the production of lighter p nuclei by (γ, p) and (γ, α) reactions depends on the temperature at that position. The convective-reactive environment of the O-shell allows for the production of both light and heavy p nuclei because the shell is not well-mixed, and therefore isotopes can be produced at their ideal temperatures while still contributing to lighter species. Figure 2.6 shows how different mass ranges of p nuclei can be produced and peak at different positions in the O-shell.

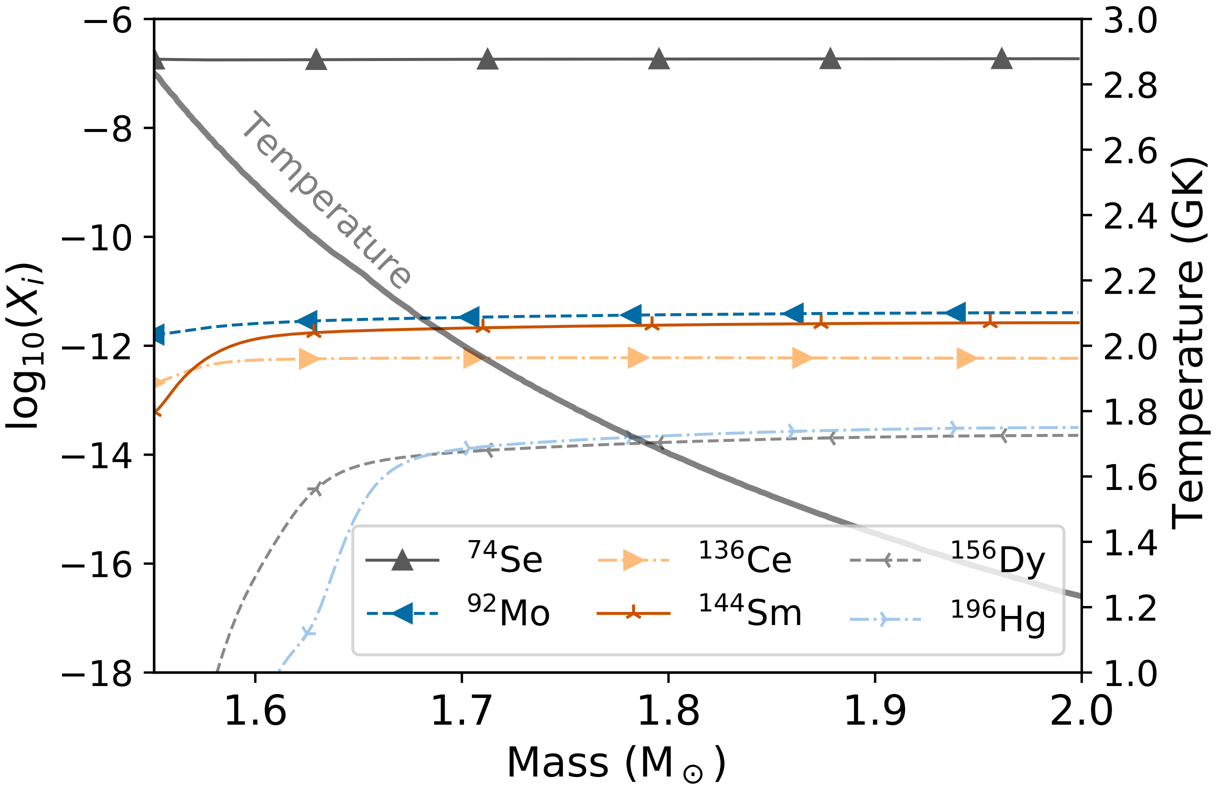

Figure 2.6: Mass fractions without radiogenic contributions at t = 110 sec for the MLT mixing scenario without C-shell ingestion.

Locations of peak destruction can be identified by a sudden drop in mass fraction as seen for ^{156}Dy, ^{196}Hg, and to a lesser extent ^{144}Sm. This is the location where $D_\alpha = 1$, which is different for each isotope (Herwig et al., 2011). This is contrary to the normal assumption of a well-mixed convective environment where $D_\alpha \ll 1$ or radiative burning where little to no mixing occurs, and is a key reason why the γ process in the O-shell produces the whole range of p nuclei. Figure 2.7 shows the dominant reactions that ^{156}Dy is produced and destroyed by in the simulation without C-shell ingestion. These reactions are shown as reaction fluxes f_{ij} which are defined as the net flux of a reaction between species i and j:

$$f_{ij} = \frac{X_i X_j}{A_i A_j} \rho N_A \Big(\langle \sigma v \rangle_{ij} - \langle \sigma v \rangle_{ji} \Big) \tag{2.7}$$

where X is the mass fraction, A is the atomic mass, ρ is the density, N_A is Avogadro's number, and $\langle \sigma v \rangle_{ij}$ is the reaction rate between species i and j.

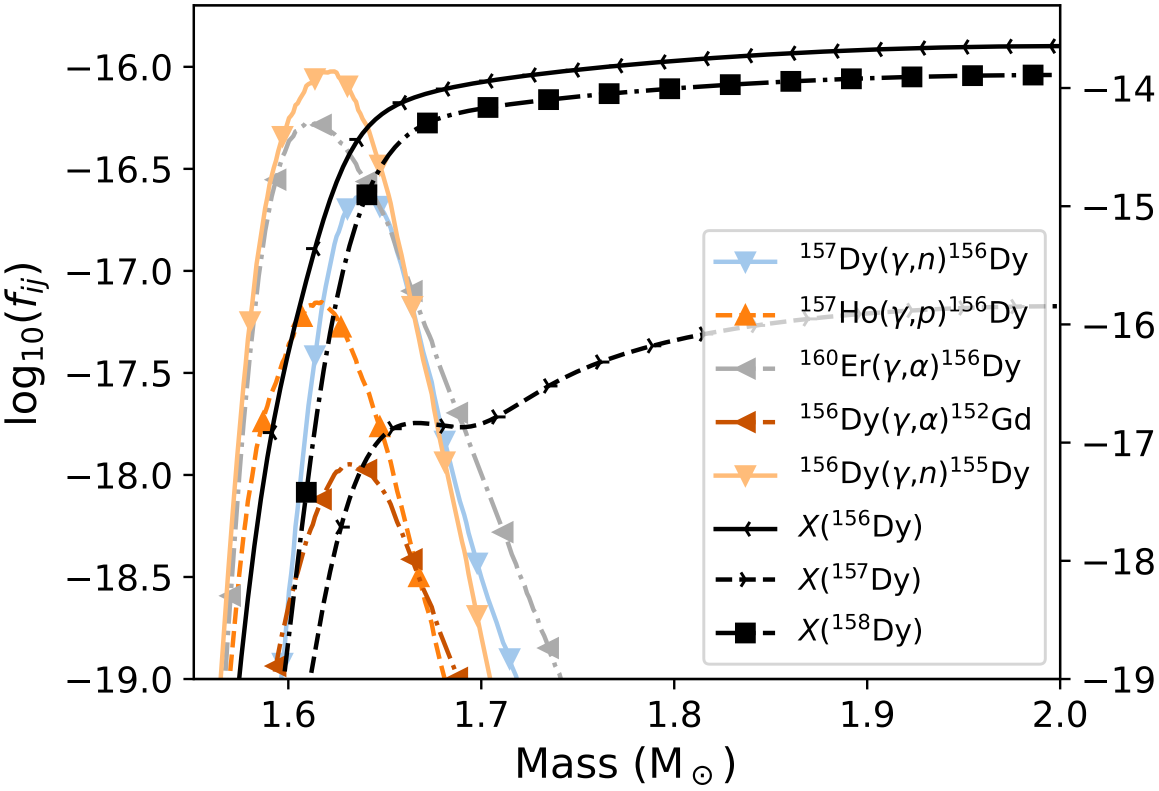

Figure 2.7: Reaction fluxes f_{ij} for ^{156}Dy and mass fractions X_i for ^{156,158}Dy and ^{157}Dy ($t_{1/2} = 8.1$ h) without radiogenic contributions for the MLT scenario with no ingestion after $t = 110$ s. The direction of a reaction is written left to right in the legend.

The reactions that ^{156}Dy undergoes in the O-shell depend on the location in the shell, however Figure 2.7 shows that the dominant destruction channel $^{156}\mathrm{Dy}(\gamma, n)^{155}\mathrm{Dy}$ net destroys ^{156}Dy, as Figure 2.11 will show. It is also evident that the mass fraction is not well-mixed as the gradient of the mass fraction is steep at the location of peak destruction.

Entraining C-shell material is important for this process, as heavier species can be gradually depleted by (γ,α) and (γ,p) reactions. Figure 2.8 shows the same as Figure 2.7, but with a C-shell ingestion rate of 4×10^{-3} $\mathrm{M_\odot s^{-1}}$, the maximum considered in this study. Since the initial amount of ^{156}Dy in the ingested C-shell is negligible as shown in Figure 2.2, the role of the merger is to provide the species that produce ^{156}Dy like the stable Dy isotopes.

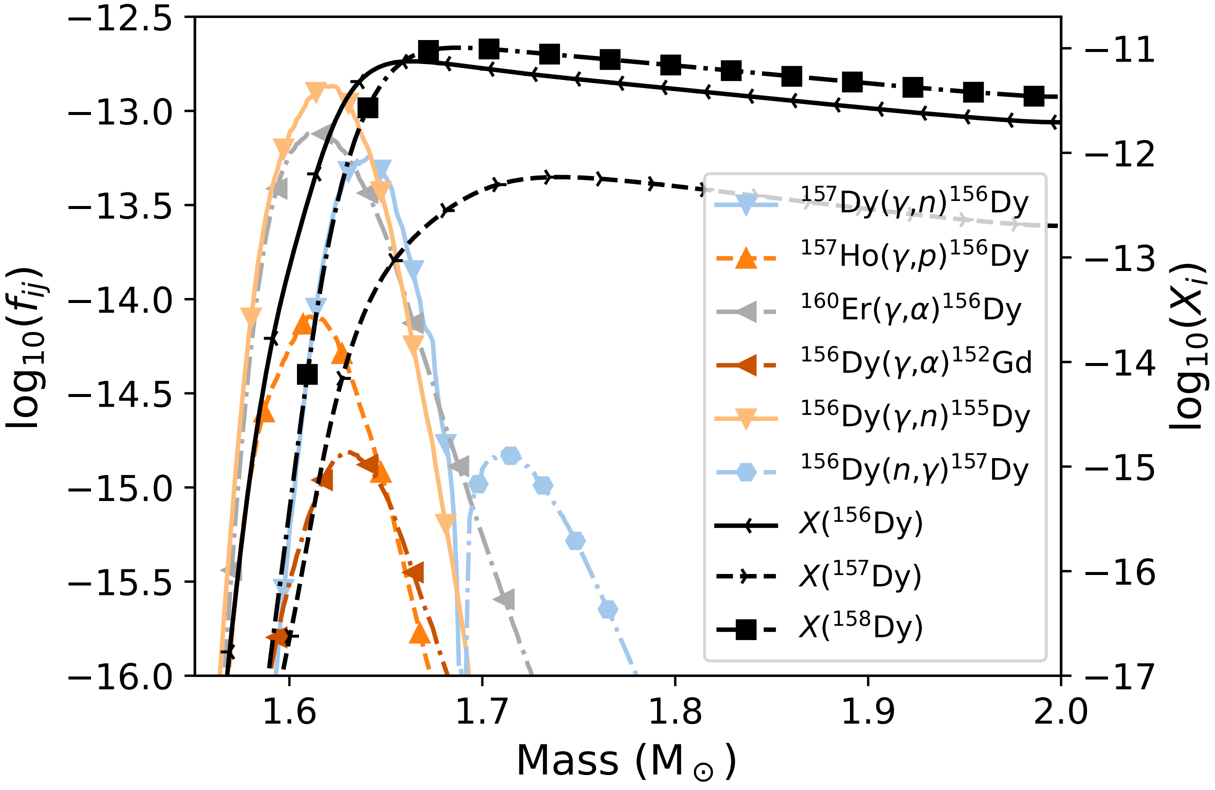

Figure 2.8: Reaction fluxes f_{ij} for ^{156}Dy and mass fractions X_i for $^{156-158}$Dy without radiogenic contributions for the MLT scenario with an ingestion rate of 4×10^{-3} $\mathrm{M_\odot s^{-1}}$ after $t = 110$ s. The direction of a reaction is written left to right in the legend.

There are several differences between Figures 2.7 and 2.8. First, f_{ij} and X_i are larger by several orders of magnitude and ^{156}Dy has a net production in the shell, as Figure 2.11 will show in Section 2.4.3. Second, the mass fraction of ^{156}Dy has a tilt up where it is net produced and then drops off sharply at the location of peak destruction instead of the decline seen in Figure 2.7.

^{156}Dy is produced because the ingestion of C-shell material allows for ^{158}Dy to be

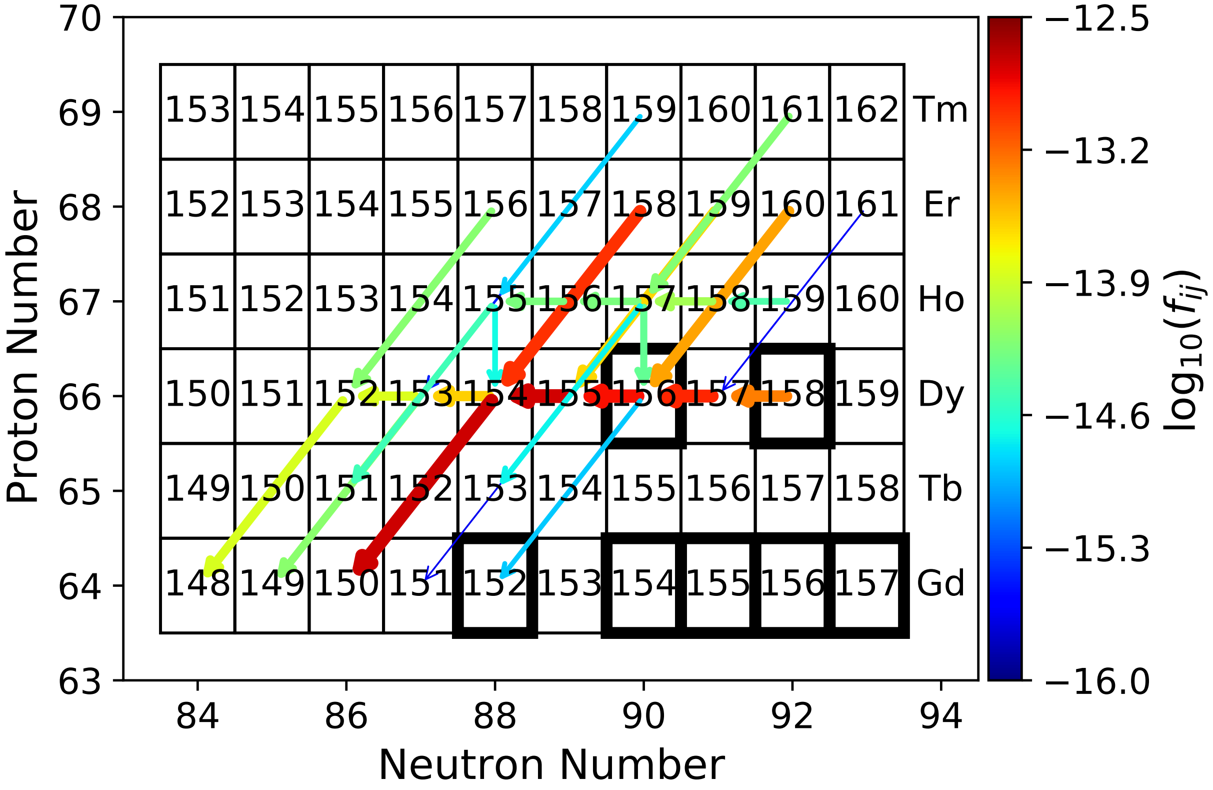

Figure 2.9: Chart of reactions between isotopes at $m = 1.64$ M$_\odot$ [$T = 2.28$ GK] for the same conditions as Figure 2.8. Both arrow colour and size indicate $\log_{10}(f_{ij})$, and arrows point in the direction of the reaction. The range of $\log_{10}(f_{ij})$ is the same as Figure 2.8.

replenished as it advects into the shell. With a continual supply of ^{158}Dy, the chain ^{158}Dy$(\gamma, n)^{157}$Dy$(\gamma, n)^{156}$Dy can occur and significantly contribute to the production of ^{156}Dy equal to ^{160}Er$(\gamma, \alpha)^{156}$Dy.

Figure 2.8 also shows another feature of this convective-reactive environment: ^{156}Dy and ^{157}Dy co-produce each other. ^{156}Dy is advected from its location of peak production at ~ 1.63 M$_\odot$ both deeper into the shell where it is fully destroyed, and toward the top where it undergoes ^{156}Dy$(n, \gamma)^{157}$Dy, which mildly contributes to the production of ^{157}Dy and peaks at ~ 1.73 M$_\odot$.

Figures 2.7 and 2.8 demonstrate that in a convective-reactive environment isotopes are not well-mixed, and that the relevance of a reaction rate depends on their location in the shell. Figure 2.8 also show how isotopes can contribute to the production of each other at different locations in the shell. Finally, comparing Figure 2.8 to Figure 2.7 shows the importance of ingesting C-shell material for significant production of the p nuclei in the

O-shell.

2.4.2 Impact from a downturn and a boost to the mixing speeds

Here we present the impact of a 3D-inspired gradual downturn at the lower boundary and boosting mixing speeds as explained in Section 2.3.2 with the diffusion coefficients in Figure 2.4. These cases are calculated with an ingestion rate of 4×10^{-3} $\mathrm{M_{\odot} s^{-1}}$ and the results are shown in Figure 2.10.

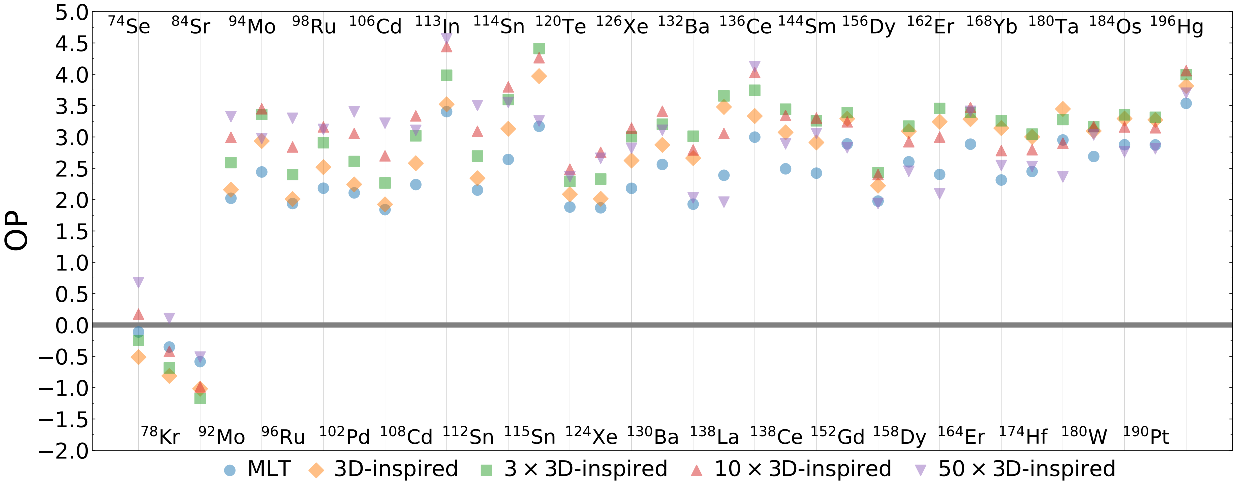

Figure 2.10: The overproduction compared to initial of the p nuclei for the MLT and 3D-inspired mixing scenarios. The average spread in production $\mathrm{OP_{max}} - \mathrm{OP_{min}} = 0.96$ dex. $\mathrm{OP} = 0$ is the initial amount.

The MLT simulation has an $\langle \mathrm{OP} \rangle$ of 2.24 dex, and the downturn scenarios have $\langle \mathrm{OP} \rangle$ of 2.58 dex, 2.83 dex, 2.89 dex, and 2.72 dex for the 1×, 3×, 10×, and 50×3D-inspired mixing scenarios respectively. The average spread in production for each isotope $\mathrm{OP_{max}} - \mathrm{OP_{min}} = 0.96$ dex, which shows that mixing speeds are important for the production of the p nuclei. This O-shell during the merger significantly produces all p nuclei except ^{74}Se, ^{78}Kr, and ^{84}Sr.

The 3D-inspired 1× scenario favours the production of the heavier p nuclei compared to the MLT scenario because τ_{mix} decreases as the temperature. Because of this, more reactions occur at the cooler temperatures where the (n, γ) and (γ, n) reactions are more favoured than the (γ, α) and (γ, p) reactions. All isotopes are comparably produced to MLT or more produced except ^{74}Se, ^{78}Kr, and ^{84}Sr who require the hottest temperatures for their production.

As mixing speeds increase, the production increases in a non-linear and non-monotonic way. For the 50× case, the average production of all p nuclei is lower than the 3× and 10×

scenarios. This is because the mixing speeds are high enough that material is advected to the bottom of the O-shell fast enough despite the downturn, and correspondingly the lighter p nuclei are generally more favoured including ^{74}Se, ^{78}Kr, and ^{84}Sr. Production for individual isotopes also can be non-linear and non-monotonic. For example, ^{115}Sn, ^{132}Ba, and ^{138}La all increase for the 1× and 3× scenarios, but then their production is not as strong for the 10× and 50× scenarios.

Another result is that isotopic pairs of the same element are not affected the same way by the downturn compared to MLT, nor by the increase in mixing speed and we find that the ratio between these isotopes is dependent on the mixing scenario. Since these isotopes are connected by (γ, n) and (n, γ) reactions, if the location of $D_\alpha = 1$ for a reaction changes because of a change to the mixing speed or the presence of the decreasing diffusion profile, then the production of these isotopes will change. ^{94}Mo is produced more for all mixing scenarios except for the 50× scenario, where ^{92}Mo has a larger OP, and likewise ^{115}Sn exhibits this behaviour when compared to ^{112}Sn and ^{114}Sn. We find that it is possible that the ratio can tend to unity as mixing speeds increase as seen for ^{96,98}Ru, ^{106,108}Cd, and ^{112,114}Sn. For ^{136,138}Ce the lighter isotope is always favoured as mixing speed increases and for ^{156,158}Dy the opposite is true. This demonstrates the importance of the decreasing diffusion profile and increasing mixing speed is for the production of the p nuclei.

2.4.3 Impact from varying the ingestion rate

Here we present the impact of entraining C-shell material with 4×10^{-5} M$_\odot$s^{-1}, 4×10^{-4} M$_\odot$s^{-1}, 4×10^{-3} M$_\odot$s^{-1} as well as no entrainment as explained in Section 2.3.2. Figure 2.11 shows the results for the MLT mixing scenario and Figures 2.16–2.19 in Appendix 2.6.2 show the results for all downturn scenarios.

The results show that the production of the p nuclei is monotonically increased by the ingestion of C-shell material for all isotopes except ^{74}Se, ^{78}Kr, and ^{84}Sr who exhibit the opposite behaviour for all mixing scenarios. The only exception is that ^{74}Se production increases for the 10× and 50×3D-inspired scenarios with ingestion rate. This is because with higher ingestion rates, the more stable isotopes enter the shell as demonstrated in Section 2.4.1. The lightest three have the opposite behaviour because without ingestion they are destroyed less by (n, γ) reactions. The difference in OP between two ingestion rates is largely uniformly for ^{92}Mo–^{196}Hg. The average spread $\mathrm{OP}_{\mathrm{max}} - \mathrm{OP}_{\mathrm{min}}$ between the different ingestion rates for the MLT and 3D-inspired scenarios is 1.22, 1.58, 1.64, 1.78, and 1.84 dex. This shows that the non-linear and non-monotonic behaviour in Section 2.4.2 is

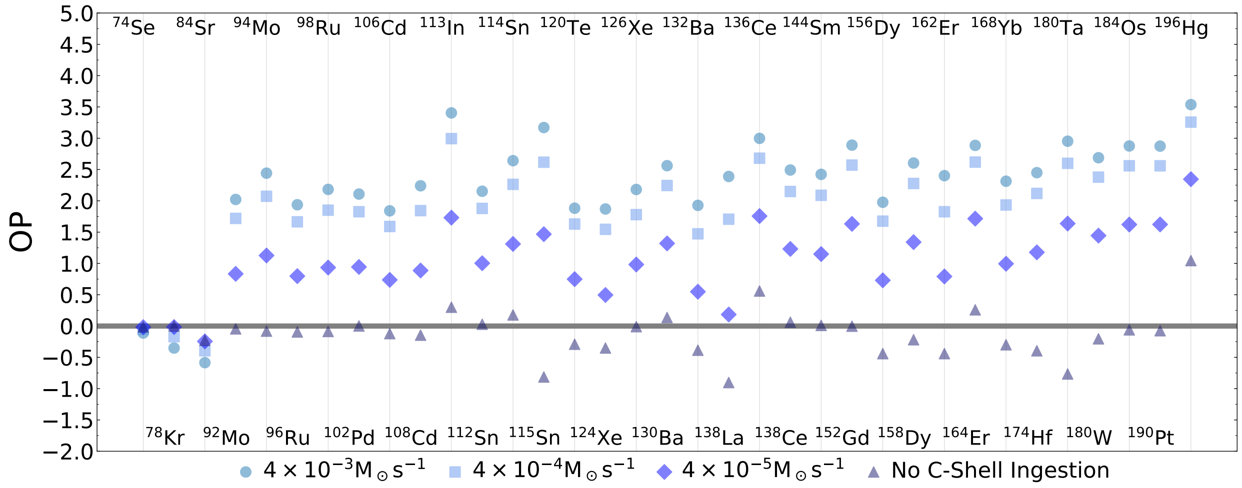

Figure 2.11: The overproduction compared to initial of the p nuclei for the MLT mixing scenario for no ingestion, 4×10^{-5} M$_\odot$s^{-1}, 4×10^{-4} M$_\odot$s^{-1}, and 4×10^{-3} M$_\odot$s^{-1}. The average spread in production $\mathrm{OP}_{\mathrm{max}} - \mathrm{OP}_{\mathrm{min}} = 1.22$ dex excluding the no ingestion case. $\mathrm{OP} = 0$ is the initial amount.

because of the changing location of peak burning in the convective-reactive environment and not just more material being present.

Without ingestion of C-shell material, the MLT, 1×, and 3× scenarios see little to no production, but for the 10× and 50× scenarios there is a significant underproduction of the heavier p nuclei. This is because in the fastest cases the species are advected to the bottom of the shell where the temperatures are purely destructive and there is no replenishment from the C-shell. This shows that entrainment of C-shell material is necessary for significant contributions from pre-explosive γ process.

The sign of the ratio of isotopic pairs is largely preserved across the ingestion rates for the MLT, 1×, 3×, and 50× scenarios, but the magnitude of the ratio does change. The few exceptions are ^{162,164}Er in the 1× and 3× scenarios who become roughly equal for the fastest ingestion rate, ^{115}Sn which becomes more abundant than ^{112,114}Sn in the 3× scenario. In the 10× scenario production of isotopic pairs is largely equal for the slower ingestion rates, but at the fastest ingestion rate the ratio can become unequal. This shows that the the ingestion rate matters for the magnitude of the ratio between isotopic pairs, but that the sign of the ratio depends on which diffusion profile is used.

2.4.4 Impact from dips from convective quenching

Here we present the impact of dips from convective quenching using the profiles shown in Figure 2.5 from Section 2.3.2 which represent GOSH-like feedback and a partial merger. The results are shown in Figure 2.12.

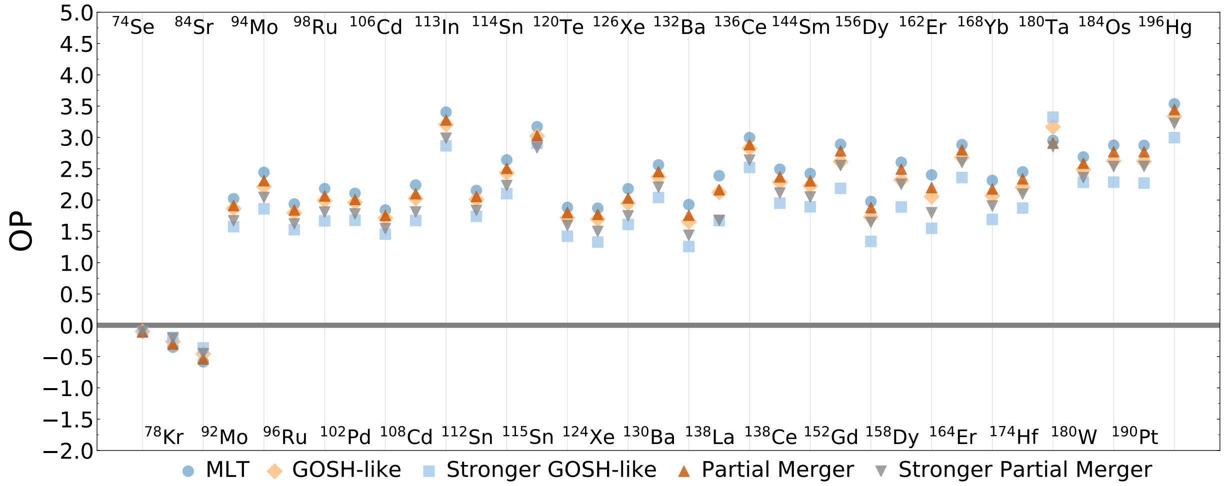

Figure 2.12: The overproduction compared to initial of the p nuclei for the MLT, GOSH-like, and partial merger scenarios with ingestion rate 4×10^{-3} $\mathrm{M}_{\odot}\mathrm{s}^{-1}$. The average spread in production $\mathrm{OP}_{\mathrm{max}} - \mathrm{OP}_{\mathrm{min}} = 0.51$ dex. $\mathrm{OP} = 0$ is the initial amount.

The MLT simulation has $\langle \mathrm{OP} \rangle$ of 2.24 dex, the GOSH-like scenarios have $\mathrm{OP} = 2.06$ dex and 1.78 dex, and the partial merger scenarios have $\mathrm{OP} = 2.13$ dex and 1.91 dex. We find that the GOSH-like scenarios suppresses the production more than the partial merger scenarios of equal dip depths, and that the deeper dips are suppress production more than the shallow with an average spread $\mathrm{OP}_{\mathrm{max}} - \mathrm{OP}_{\mathrm{min}} = 0.51$.

The dip functions as a barrier for the convective-reactive flow, and can section off parts of the O-shell. The partial merger scenario both limits the ingested C-shell material and slows down the material from deeper in the O-shell from advecting up to the top of the shell where very few reactions occur. The GOSH-like dip slows down the material from reaching their preferential temperatures, and also prevents material at the deepest part of the O-shell from mixing up to the top of the shell which keeps it at hotter temperatures where it can be destroyed. This is also why the deeper dips suppress production more, as the velocities are slower by an additional factor of 10 at the deepest point of the dip.

The suppression of production is largely uniform for all isotopes except for ^{74}Se, ^{78}Kr, ^{84}Sr, and ^{180}Ta. Additionally, it appears that isotopes $A \geq 138$ are more strongly affected by the stronger GOSH-like dip. The isotopes ^{74}Se, ^{78}Kr, and ^{84}Sr have a minor increase from these dips because the location of their production is at the bottom of the O-shell where the dips are not present. The boost in production of ^{180}Ta is because the peak production and destruction locations happen to be centered at the exact same location as the GOSH dip, which lowers its destruction and slightly boosts its production. Isotopic ratios are not significantly affected by the dips, although the magnitude of the ratios can increase slightly. This demonstrates the importance of both the location and magnitude of the convective dips in the O-shell for convective-reactive γ process.

2.4.5 Nuclear physics impact and mixing dependencies

Here we present the impact of varying our adopted nuclear physics rates for the MLT and 3D-inspired mixing scenarios for an ingestion rate of 4×10^{-3} M$_\odot$s^{-1}. The result for the MLT mixing scenario is shown in Figure 2.13 and Table 2.4, and the 3D-inspired mixing scenarios are shown in Figures 2.20–2.23 and Tables 2.4–2.8 which can be found in Appendix 2.6.3.

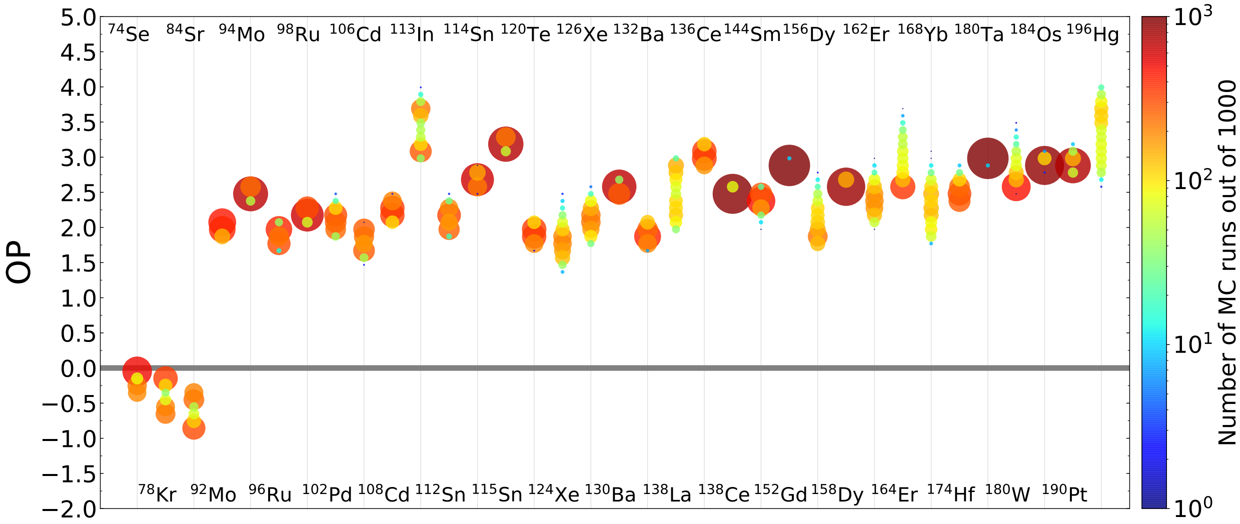

Figure 2.13: Histogram showing the spread due to varying (γ, p), (γ, n), (γ, α) and corresponding capture rates for unstable n-deficient isotopes from Se–Po for the MLT mixing scenario. Colour and size both correspond to the logarthimic binning of Monte Carlo runs. The average spread $\mathrm{OP}_{\mathrm{max}} - \mathrm{OP}_{\mathrm{min}} = 0.56$ dex. OP $= 0$ is the initial amount.

The MLT mixing scenario has an average spread in production of $\mathrm{OP}_{\mathrm{max}} - \mathrm{OP}_{\mathrm{min}} = 0.56$ dex, and the 3D-inspired scenarios have an average spread of 0.59 dex, 0.69 dex, 0.76 dex, and 0.79 dex for the 1×, 3×, 10×, and 50× scenarios respectively. We find that the spread in production increases with mixing speed because the material is able to reach hotter temperatures and the number of possible nucleosynthetic pathways changes.

In the MLT mixing scenario about a third of the isotopes are not affected in any significant way, but in the 3D-inspired scenarios only 5 are not affected although the specific isotopes vary. The isotopes that appear the least affected across mixing scenario are ^{138}Ce, ^{152}Gd, ^{158}Dy, and ^{180}Ta.

The spread of an individual isotope is dependent on the mixing scenario. Species like ^{106}Cd, ^{156}Dy, and ^{180}W have a different spread in production for each mixing scenario. While the change can be monotonic for species like ^{180}W, ^{184}Os, and ^{190}Pt, for ^{106}Cd and ^{112}Sn, and ^{130}Ba they decrease for the 50×3D-inspired scenario.

This mixing scenario dependence for the spread is also seen for the distribution of OP as no isotope is double peaked across all mixing scenarios. As examples, ^{74}Se, ^{113}In, and ^{138}La in some mixing scenarios clearly are double peaked, indicating that there are distinctive branches in the nucleosynthetic pathways, but do not have it in others. Additionally, the magnitude of which peak is favoured is also dependent on the mixing scenario as seen for ^{78}Kr and ^{84}Sr.

Whether a particular reaction rate is correlated with an isotope's final mass fraction along with the strength of the correlation is dependent on the mixing scenario. Table 2.2 lists the rates unique to single mixing scenario.

It is clearly important to consider the mixing conditions if an experiment is to be proposed to measure a reaction rate. As Table 2.2 shows for the 50×3D-inspired scenario, there are many reactions even for a single isotope that can be correlated uniquely in that mixing scenario. This clearly shows that a decreasing radial velocity profile and the exact magnitude of the mixing speeds are crucial for understanding the nuclear reactions in this convective-reactive environment.

There are also correlated reactions that all mixing scenarios share as shown in Table 2.3. Additionally, all downturn cases share correlations not found in the MLT scenario: $X(^{115}\mathrm{Sn})$ with $^{110}\mathrm{Sn}(\gamma,\alpha)$ and $X(^{138}\mathrm{Ce})$ with $^{138}\mathrm{Nd}(\gamma,p)$. However, the shared correlations are not of equal strength across all mixing scenarios. As an example the final mass fraction of ^{156}Dy is correlated with $^{160}\mathrm{Er}(\gamma,\alpha)$, but in the 50×3D-inspired the correlation is much weaker. This underscores the possible difficulties in using 1D astrophysical sites to identify important reactions for nuclear physics experiments.

The spread in production for varying our adopted nuclear physics rates for each of the mixing scenarios is comparable to the spread seen from varying the mixing conditions. The results in Section 2.4.4 have a spread of 0.51 dex, in Section 2.4.2 they are 0.96 dex, and the maximum spread in Section 2.4.3 is 1.84 dex. The average spread in production from varying the nuclear physics rates ranges from 0.56–0.79 dex.

Table 2.2: Reactions correlated with the production/destruction of an isotope unique to an individual mixing scenario.

Isotope	**Unique Correlated Reaction Rates**
MLT Mixing Case	
^{138}Ce	^{139}Pr(γ, p)
^{168}Yb	^{176}W(γ, α)
^{174}Hf	^{178}W(γ, n)
^{184}Os	^{186}Pt(γ, n), ^{188}Pt(γ, n)
3D-inspired Mixing Scenario	
^{113}In	^{114}In(γ, n)
^{152}Gd	^{150}Gd(γ, α), ^{196}Pb(γ, n)
^{180}Ta	^{179}Ta(γ, α)
3×3D-inspired Mixing Scenario	
^{180}W	^{181}Os(γ, n)
10×3D-inspired Mixing Scenario	
^{84}Sr	^{84}Rb(γ, n)
^{120}Te	^{119}Te(γ, n)
^{126}Xe	^{122}Xe(γ, n)
^{130}Ba	^{126}Ba(γ, p), ^{128}Ba(γ, α), ^{128}Ba(γ, p)
^{132}Ba	^{128}Ba(γ, α)
^{168}Yb	^{169}Hf(γ, n)
^{174}Hf	^{176}W(γ, α)
^{184}Os	^{185}Pt(γ, α)
50×3D-inspired Mixing Scenario	
^{92}Mo	^{100}Pd(γ, α), ^{100}Pd(γ, p), ^{110}Sn(γ, n), ^{110}Sn(γ, p)
^{96}Ru	^{97}Ru(γ, α), ^{110}Sn(γ, α), ^{110}Sn(γ, n), ^{110}Sn(γ, p)
^{102}Pd	^{104}Cd(γ, α), ^{104}Cd(γ, p)
^{106}Cd	^{104}Cd(γ, p), ^{110}Sn(γ, p)
^{108}Cd	^{110}Sn(γ, α)
^{112}Sn	^{110}Sn(γ, p)
^{115}Sn	^{122}Xe(γ, n)
^{120}Te	^{120}Xe(γ, α)
^{126}Xe	^{127}Ba(γ, n)
^{130}Ba	^{132}Ce(γ, α), ^{132}Ce(γ, n), ^{132}Ce(γ, p), ^{134}Ce(γ, α), ^{134}Ce(γ, n)
^{132}Ba	^{132}Ce(γ, α), ^{132}Ce(γ, n), ^{132}Ce(γ, p), ^{133}Ce(γ, n), ^{134}Ce(γ, α)
^{138}Ce	^{139}Nd(γ, n)
^{156}Dy	^{156}Er(γ, α), ^{158}Er(γ, α), ^{158}Er(γ, n)
^{162}Er	^{168}Hf(γ, n), ^{162}Yb(γ, α), ^{164}Yb(γ, α)
^{184}Os	^{184}Pt(γ, n)

Rauscher et al. (2016) studied the impact of nuclear uncertainties for the explosive γ-process for a 15 $M_\odot$ and two 25 $M_\odot$ models with solar metallicity using a Monte Carlo

Table 2.3: Reactions correlated with the production/destruction of an isotope shared across all mixing scenarios.

Isotope	**Shared Correlated Reaction Rates**
^{74}Se	^{75}Se(γ, n)
^{78}Kr	^{79}Kr(γ, n)
^{84}Sr	^{85}Sr(γ, n)
^{92}Mo	^{93}Mo(γ, n)
^{94}Mo	^{93}Mo(γ, n)
^{96}Ru	^{97}Ru(γ, n)
^{98}Ru	^{100}Pd(γ, α), ^{100}Pd(γ, p)
^{102}Pd	^{100}Pd(γ, α), ^{100}Pd(γ, p), ^{103}Pd(γ, n)
^{106}Cd	^{107}Cd(γ, n), ^{110}Sn(γ, α)
^{108}Cd	^{107}Cd(γ, n)
^{113}In	^{113}Sn(γ, n)
^{112}Sn	^{113}Sn(γ, n)
^{114}Sn	^{110}Sn(γ, α), ^{113}Sn(γ, n), ^{122}Xe(γ, α)
^{115}Sn	^{113}Sn(γ, n)
^{120}Te	^{122}Xe(γ, α), ^{122}Xe(γ, p)
^{124}Xe	^{122}Xe(γ, α), ^{122}Xe(γ, p)
^{138}La	^{137}La(γ, n)
^{136}Ce	^{138}Nd(γ, n), ^{138}Nd(γ, p), ^{140}Nd(γ, α)
^{144}Sm	^{196}Pb(γ, n), ^{142}Sm(γ, n), ^{142}Sm(γ, p), ^{143}Sm(γ, n)
^{152}Gd	^{152}Dy(γ, α)
^{156}Dy	^{160}Er(γ, α)
^{164}Er	^{164}Yb(γ, α), ^{164}Yb(γ, n)
^{174}Hf	^{174}W(γ, α)
^{180}Ta	^{179}Ta(γ, n)
^{180}W	^{180}Os(γ, α), ^{180}Os(γ, n), ^{196}Pb(γ, n)
^{184}Os	^{196}Pb(γ, n), ^{184}Pt(γ, α)
^{190}Pt	^{190}Hg(γ, α), ^{190}Hg(γ, n), ^{196}Pb(γ, n)
^{196}Hg	^{196}Pb(γ, n), ^{202}Pb(γ, n)

method. The spread in their 90% probability interval for the 15 $M_\odot$ model was 0.61 dex, 0.63 dex for the 25 $M_\odot$ KEPLER model, and 0.99 dex for the model from Hashimoto et al. (1989). This is comparable to the maximum spread found in this work, although we are considering pre-explosive γ process. Rauscher et al. (2016) also provide tables of correlated rates, but only a handful of these rates appear in our Tables 2.4–2.8 including those they find with $r_{\mathrm{P}} \geq |0.65|$. This is because the convective-reactive environment we consider allows for different reaction pathways to be favoured depending on the mixing conditions.

2.5 Discussions and Conclusion

In this paper, we have shown that understanding the mixing details in the O-burning shell during an O-C shell merger is crucial for accurately modelling the nucleosynthesis of the *p* nuclei. This work raises the importance of 3D hydrodynamic simulations for understanding the nucleosynthesis in O-C shell mergers (Bazan and Arnett, 1994; Yadav et al., 2020; Rizzuti et al., 2024a). We have demonstrated the convective-reactive nature of the nucleosynthesis in the O-shell, where the timescales for advection and reaction are comparable and our results show that:

- A gradual downturn motivated by 3D simulations increases production of the *p* nuclei, but increasing mixing speeds impacts the production in a non-linear and non-monotonic way.
- The ratio of isotopic pairs is sensitive to the mixing scenario.
- Increasing the entrainment rate of C-shell material increases the production of the *p* nuclei.
- Without entrainment, the *p* nuclei are negligibly produced or net destroyed.
- A dip in the convective profile can suppress the production of the *p* nuclei.
- The location and magnitude of the convective dip impacts the nucleosynthesis of the *p* nuclei.
- Varying the adopted reactions rates have a comparable spread in production to changing mixing conditions.
- The spread due to varying the reaction rates is dependent on the mixing scenario.
- Whether a reaction rate is correlated with an isotope is dependent on the mixing scenario, and some are unique to a single mixing scenario.

Figure 2.14 shows the maximum spread for the *p* nuclei across all mixing scenarios considered in this paper, excluding the case of no merger, with an average spread of 2.45 dex. This shows the significant impact of the macrophysical uncertainties in 1D stellar models on nucleosynthesis, and this highlights the importance of understanding hydrodynamic models better as the shell merger dominates production of the *p* nuclei (Roberti et al., 2023, 2024).

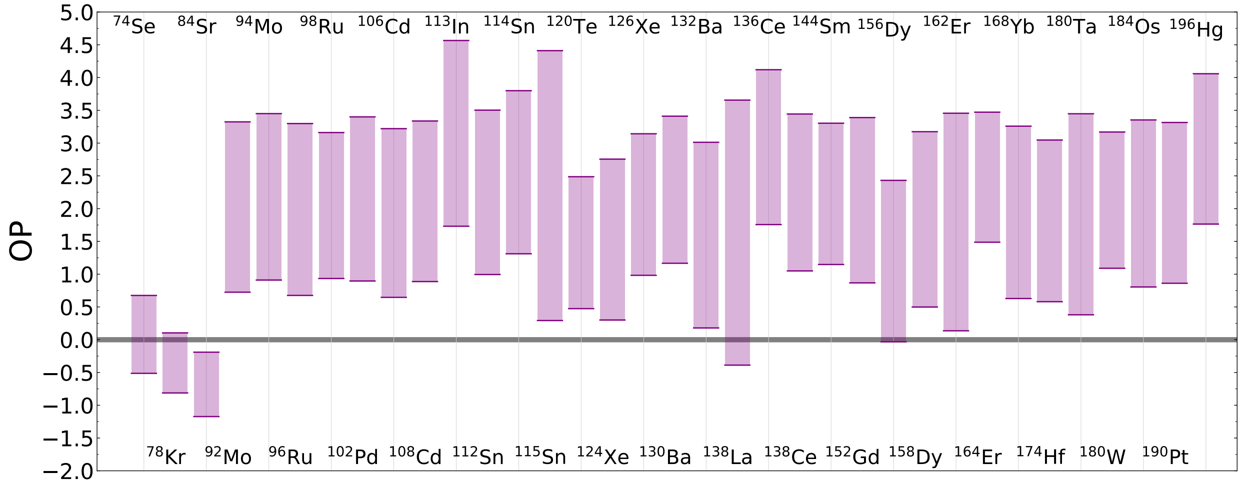

Figure 2.14: Bars representing the maximum and minimum OP across all mixing scenarios, excluding those without C-shell ingestion. The average spread $\mathrm{OP}_{\mathrm{max}} - \mathrm{OP}_{\mathrm{min}} = 2.45$ dex. $\mathrm{OP} = 0$ is the initial amount.

Although we find that the mixing conditions significantly impact the results of Section 2.4.5, not all scenarios are equally likely to represent the conditions in a merger. The MLT mixing scenario, 1×, and 50× case may not be representative of the conditions for realistic O-C shell mergers. 3D hydrodynamic simulations show the O-shell has a downturn to radial convective velocities and mixing speeds roughly $3 - 10$ times larger than what MLT predicts (Jones et al., 2017; Andrassy et al., 2020; Rizzuti et al., 2024a). This suggests that the 3× and 10× downturn mixing scenarios are likely more representative of the conditions in a merger. The exploration done in this paper shows the importance of understanding the mixing conditions.

The results in this work are important for the interpretation of presolar grains. Fok et al. (2024) argue that the nucleosynthesis in O-C shell mergers matter when interpreting the $^{29}\mathrm{Si}/^{28}\mathrm{Si}$ ratio seen in grains. As shown in this work, the ratio of isotopic pairs is sensitive to the mixing conditions in the O-shell. This means that comparing the grains data to the results of this work can be used as a diagnostic tool to constrain the mixing details of O-C shell mergers and connect measured isotopic ratios to 3D hydrodynamics.

There are limitations to the results provided in this work and further extensions that could be done. We have focused on the impact of mixing conditions and varying reaction rates, but do not investigate how different stellar conditions are relevant to the nucleosynthesis or if changing the stable seeds from the C-shell impact these results. The distribution of stable seeds and the metallicity of the star are of significant importance for the nucleosynthesis of the p nuclei (Travaglio et al., 2015; Battino et al., 2020). It is possible that earlier in stellar evolution that weak s process in the C-shell could modify the stable seeds (Pignatari et al., 2010), which could be relevant for the lighter p nuclei.

Other stellar models could have different O-shell sizes and temperature profiles due to different mixing prescriptions, initial mass, and rotations, which would directly affect locations of peak burning and how the mixing conditions impact the nucleosynthesis. However, if the shell is convective-reactive, a spread in production comparing mixing scenarios would still be expected.

Finally, O-C shell mergers are crucial to the nucleosynthesis of a massive star prior to the CCSN regardless of explosive energy (Roberti et al., 2024). Even if the results in Figure 2.14 do not represent the whole of the nucleosynthesis of the p nuclei, they are still crucial for understanding the nucleosynthesis in the O-shell prior to the CCSN.

The results of this work have implications beyond the p nuclei. The light odd-Z elements P, Cl, K, and Sc are also produced during O-C shell mergers and based on our preliminary results are likewise impacted by varying the mixing conditions (Ritter et al., 2018a; Roberti et al., 2025). The long-lived radioactive isotope ^{40}K ($t_{1/2} = 1.25 \times 10^9$ yr), which is relevant to the heating of planets early in their formation (Frank et al., 2014; O'Neill et al., 2020), is also affected along with the stable K isotopes ^{39}K and ^{41}K. Finally, observations have found P-enhanced stars (Masseron et al., 2020; Brauner et al., 2023, 2024) which could be explained by a O-C shell merger from a previous massive star.

O-C shell mergers have a potentially huge impact on galactic chemical evolution models (Ritter et al., 2018a), and massive star models show this feature regardless of metallicity and stellar evolution model (Roberti et al., 2025). Further work is needed to understand the impact of the macrophysical uncertainties in 1D stellar models on the nucleosynthesis of these light odd-Z elements.

2.6 Appendix

2.6.1 Correlations of nuclear reaction rates

The Pearson correlation coefficient, r_{P}, is insufficient to assess the importance of a correlated rate. As shown in Figure 2.15, a strong correlation does not necessarily imply a significant impact on the final mass fraction of a species. To better quantify this impact, we use ζ, which is defined as the slope of the linear regression between $\log_{10}(X/X_{\text{no variation}})$ and $\log_{10}(\text{variation factor})$, where X is the final, mass-averaged, and decayed mass fraction for a variation, and $X_{\text{no variation}}$ is the corresponding default case with no rate variation.

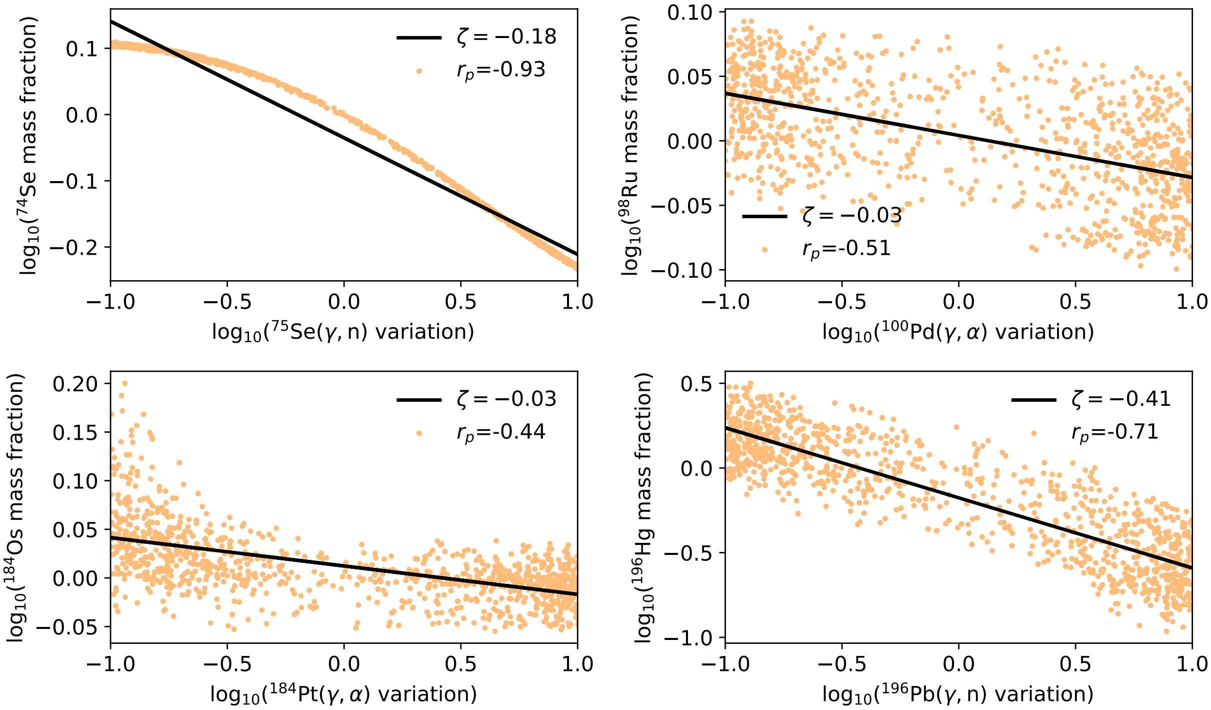

Figure 2.15: Examples of strong correlations between mass fractions and reaction rates for four species under the MLT scenario. Orange dots indicate mass fractions for each variation factor, and the black line shows the linear fit to $\log_{10}(X/X_{\text{no variation}})$ versus $\log_{10}$(variation factor). Top left and bottom right: strong correlation and significant mass fraction changes for ^{74}Se and ^{196}Hg. Top right: strong correlation for ^{98}Ru with large scatter. Bottom left: correlation for ^{184}Os with a weak slope and asymmetric impact.

Figure 2.15 demonstrates that strong correlations do not always imply significance, nor does a strong ζ guarantee it. For instance, the bottom right panel shows ^{196}Hg with both a strong correlation and slope, while the bottom left shows a strong correlation for ^{184}Os but a weak slope. Only rates with both high r_{P} and ζ substantially affect final abundances.

A caveat of r_{P} for this method of varying the reaction rates is that it not distinguish between the photo-disintegration and corresponding capture rate because the same variation factor is applied to both. All correlated rates are reported according to their photo-disintegration rates, but as shown by the upper left plot of Figure 2.15 for ^{74}Se and $^{75}\mathrm{Se}(\gamma, n)^{74}\mathrm{Se}$ this results in a production term having a negative correlation because $^{74}\mathrm{Se}(n, \gamma)^{75}\mathrm{Se}$ is also modified in the same way. As explained in Section 2.4.1, the reactions in this shell are not balanced and both a destruction and production term could be relevant at different locations, although as Figure 2.8 shows for heavier species the (γ, n) rate is typically much stronger.

2.6.2 Results of varying ingestion rate

Here we provide the results for varying the ingestion rates for the scenarios with a downturn in the mixing efficiency profile as shown in Figure 2.4.

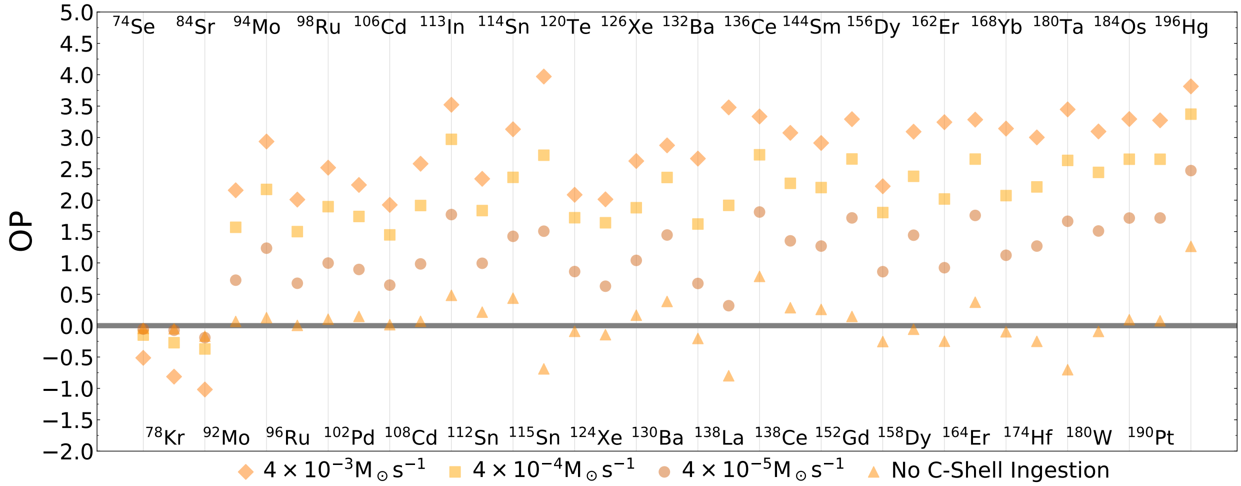

Figure 2.16: The overproduction compared to initial of the p nuclei for the 3D-inspired mixing scenario for no ingestion, 4×10^{-5} $M_\odot s^{-1}$, 4×10^{-4} $M_\odot s^{-1}$, and 4×10^{-3} $M_\odot s^{-1}$. The average spread in production $OP_{max} - OP_{min} = 1.58$ dex. $OP = 0$ is the initial amount.

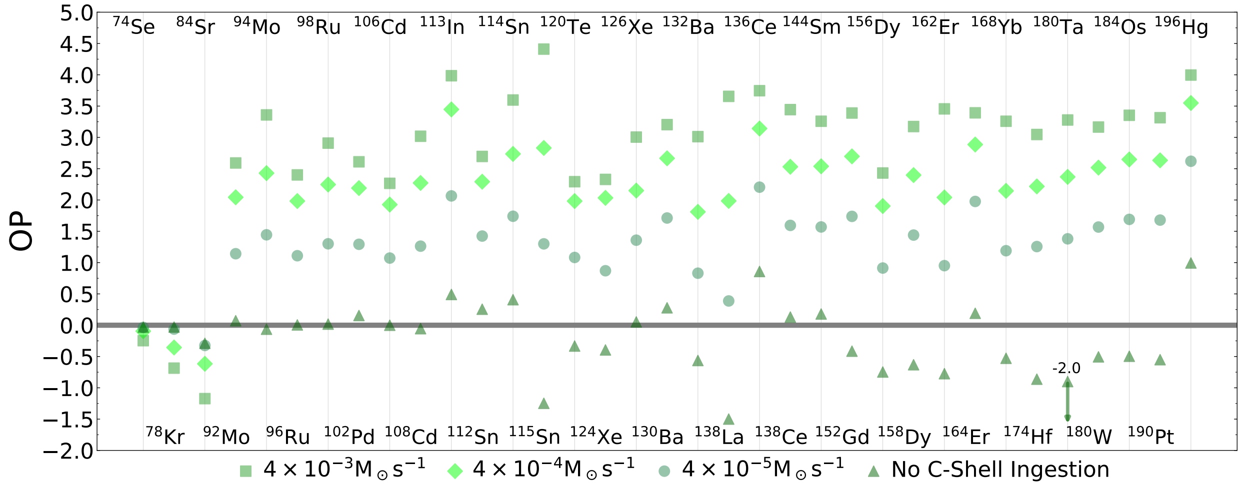

Figure 2.17: The overproduction compared to initial of the p nuclei for the 3×3D-inspired mixing scenario for no ingestion, 4×10^{-5} $M_\odot s^{-1}$, 4×10^{-4} $M_\odot s^{-1}$, and 4×10^{-3} $M_\odot s^{-1}$. The average spread in production $OP_{max} - OP_{min} = 1.64$ dex excluding the no ingestion case. $OP = 0$ is the initial amount.

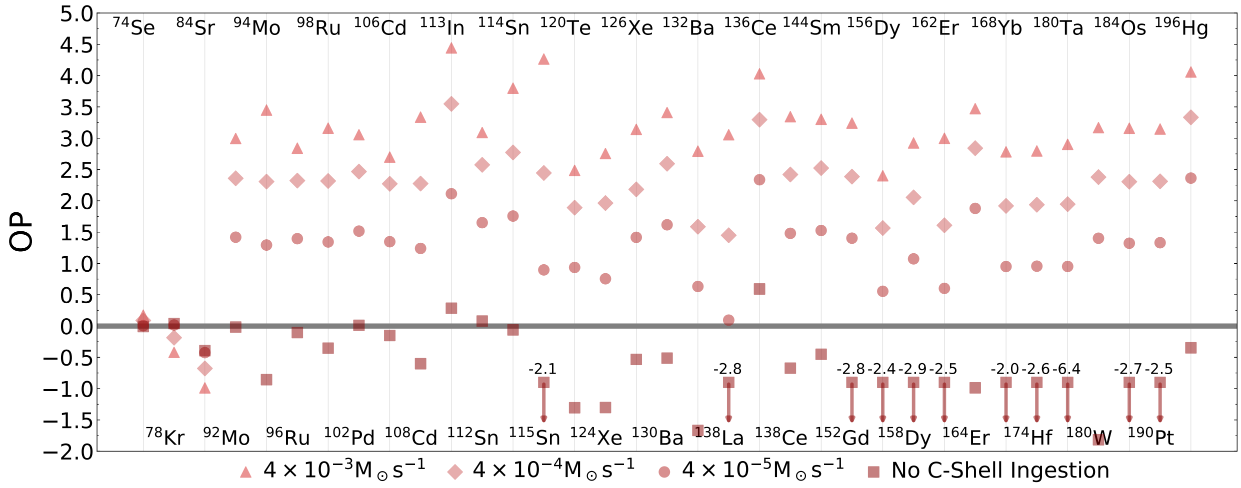

Figure 2.18: The overproduction compared to initial of the p nuclei for the 10×3D-inspired mixing scenario for no ingestion, 4×10^{-5} $\mathrm{M_{\odot}s^{-1}}$, 4×10^{-4} $\mathrm{M_{\odot}s^{-1}}$, and 4×10^{-3} $\mathrm{M_{\odot}s^{-1}}$. Arrows denote OP out of bounds and the true OP is written above. The average spread in production $\mathrm{OP_{max}} - \mathrm{OP_{min}} = 1.78$ dex excluding the no ingestion case. OP = 0 is the initial amount.

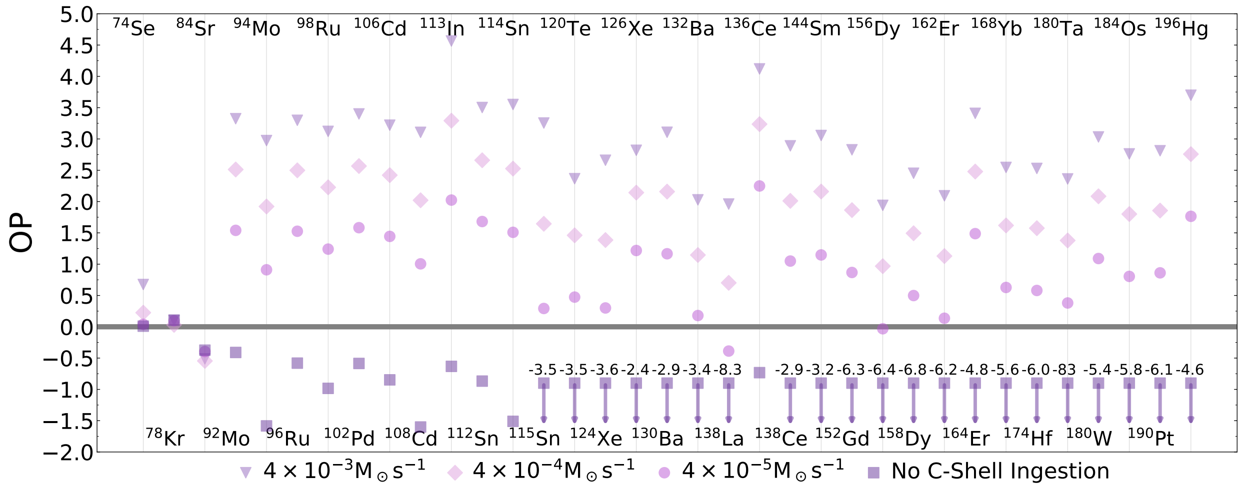

Figure 2.19: The overproduction compared to initial of the p nuclei for the 50×3D-inspired mixing scenario for no ingestion, 4×10^{-5} $\mathrm{M_{\odot}s^{-1}}$, 4×10^{-4} $\mathrm{M_{\odot}s^{-1}}$, and 4×10^{-3} $\mathrm{M_{\odot}s^{-1}}$. Arrows denote OP out of bounds and the true OP is written above. The average spread in production $\mathrm{OP_{max}} - \mathrm{OP_{min}} = 1.84$ dex excluding the no ingestion case. OP = 0 is the initial amount.

2.6.3 Results of varying the input nuclear reactions

Here we provide the results for varying the input nuclear reactions for the scenarios with a downturn in the mixing efficiency profile as shown in Figure 2.4 and the reaction rate correlation tables for the MLT and downturn scenarios.

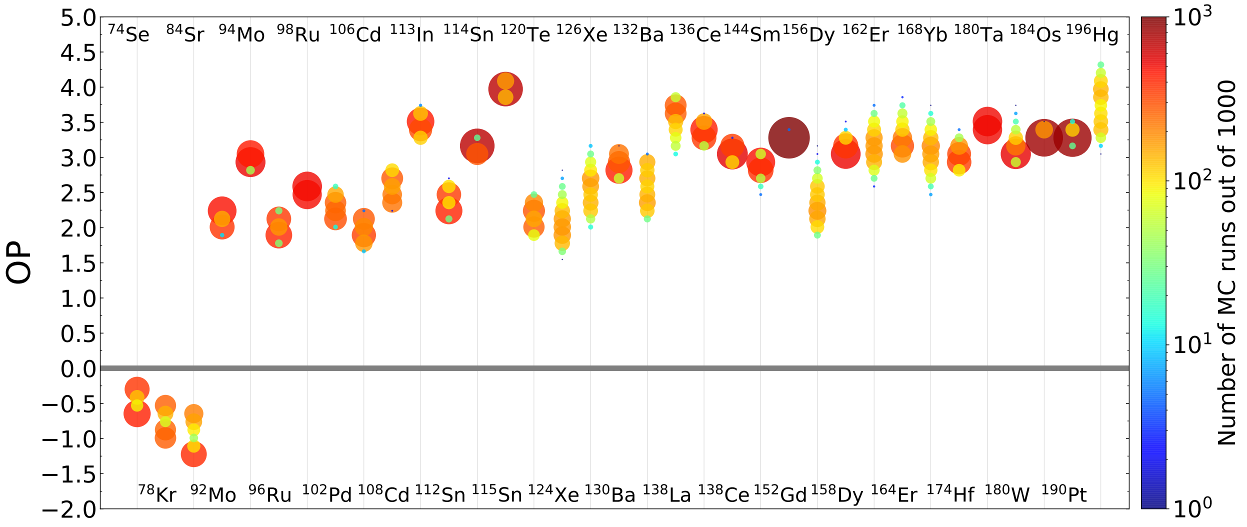

Figure 2.20: Histogram showing the spread due to varying (γ, p), (γ, n), (γ, α) and corresponding capture rates for unstable n-deficient isotopes from Se–Po for the 3D-inspired mixing scenario. Colour and size both correspond to the logarthimic binning of Monte Carlo runs. The average spread $\mathrm{OP}_{\max} - \mathrm{OP}_{\min} = 0.59$ dex. OP $= 0$ is the initial amount.

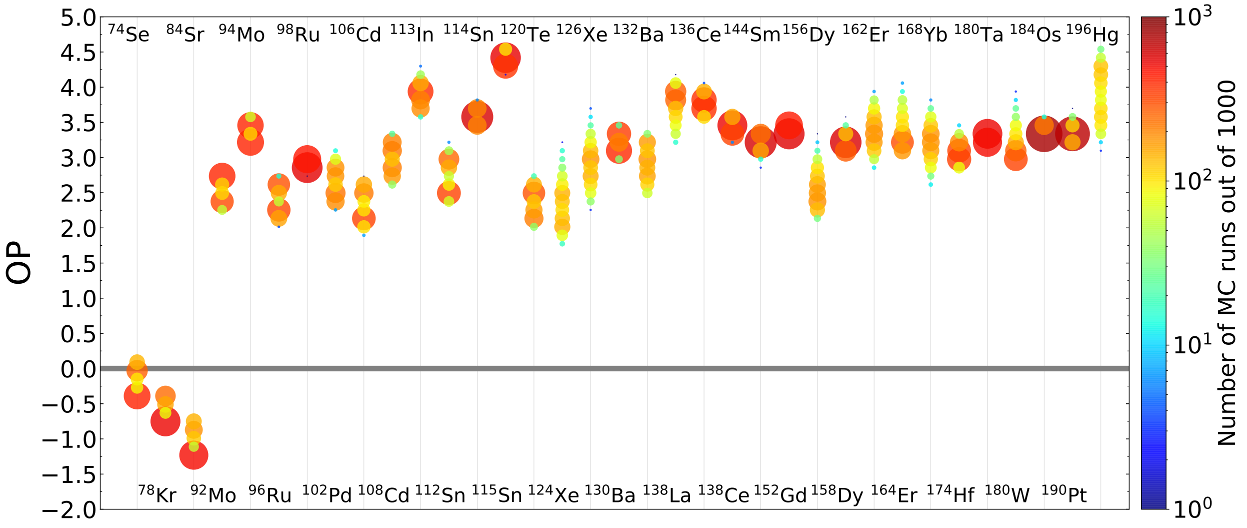

Figure 2.21: Histogram showing the spread due to varying (γ, p), (γ, n), (γ, α) and corresponding capture rates for unstable n-deficient isotopes from Se–Po for the 3×3D-inspired mixing scenario. Colour and size both correspond to the logarthimic binning of Monte Carlo runs. The average spread $\mathrm{OP}_{\max} - \mathrm{OP}_{\min} = 0.69$ dex. OP $= 0$ is the initial amount.

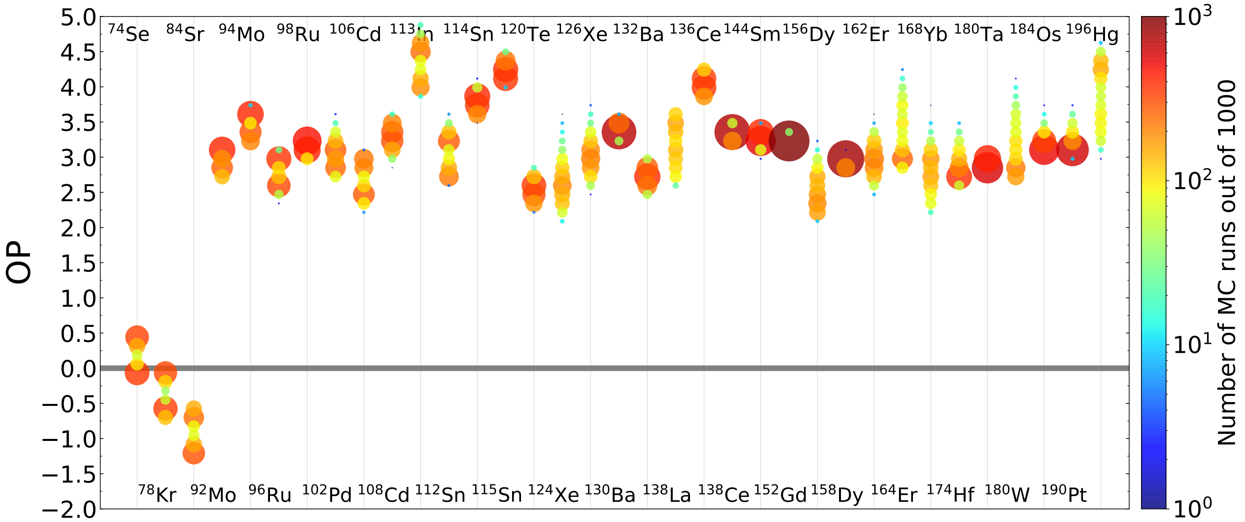

Figure 2.22: Histogram showing the spread due to varying (γ, p), (γ, n), (γ, α) and corresponding capture rates for unstable n-deficient isotopes from Se–Po for the 10×3D-inspired mixing scenario. Colour and size both correspond to the logarthimic binning of Monte Carlo runs. The average spread $\text{OP}_{\text{max}} - \text{OP}_{\text{min}} = 0.76$ dex. OP $= 0$ is the initial amount.

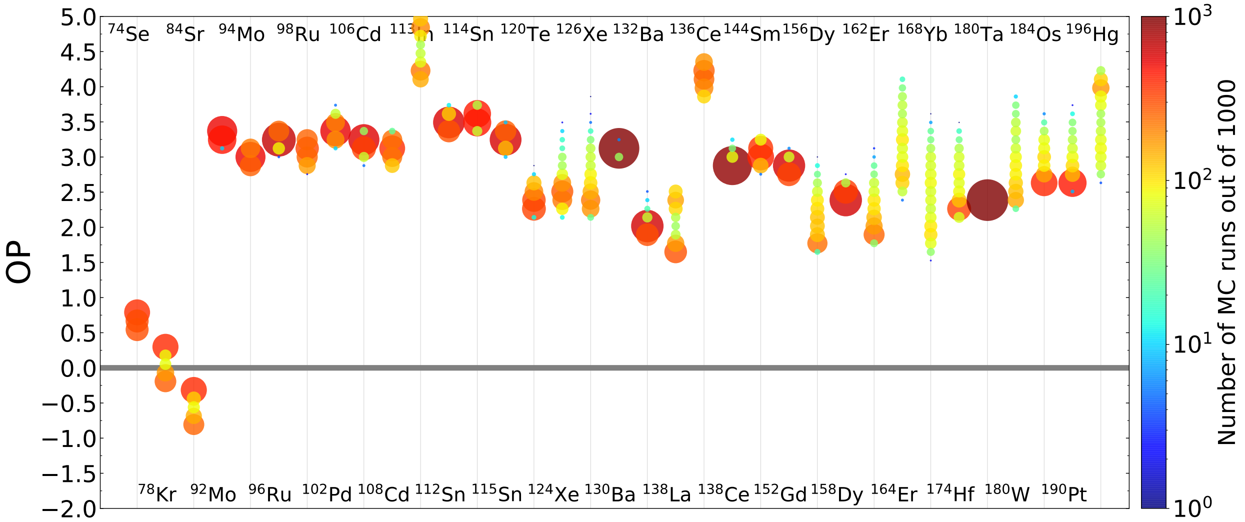

Figure 2.23: Histogram showing the spread due to varying (γ, p), (γ, n), (γ, α) and corresponding capture rates for unstable n-deficient isotopes from Se–Po for the 50×3D-inspired mixing scenario. Colour and size both correspond to the logarthimic binning of Monte Carlo runs. The average spread $\text{OP}_{\text{max}} - \text{OP}_{\text{min}} = 0.79$ dex. OP $= 0$ is the initial amount.

Table 2.4: Correlations and ζ slopes between mass fraction and reaction rates for the MLT mixing scenario.

Isotope	**Reaction**	$\mathbf{r_P}$	ζ	**Isotope**	**Reaction**	$\mathbf{r_P}$	ζ
^{74}Se	^{75}Se(γ,n)	−0.93	−0.18	^{144}Sm	^{142}Sm(γ,n)	−0.19	−0.02
^{78}Kr	^{79}Kr(γ,n)	−0.88	−0.28		^{142}Sm(γ,p)	−0.17	−0.02
^{84}Sr	^{85}Sr(γ,n)	−0.88	−0.28		^{143}Sm(γ,n)	−0.25	−0.03
^{92}Mo	^{93}Mo(γ,n)	−0.94	−0.07		^{146}Sm(γ,n)	0.20	0.03
	^{110}Sn(γ,α)	0.16	0.01		^{150}Gd(γ,n)	0.17	0.02
^{94}Mo	^{93}Mo(γ,n)	0.97	0.06		^{150}Gd(γ,α)	−0.15	−0.02
^{96}Ru	^{97}Ru(γ,n)	−0.88	−0.12		^{196}Pb(γ,n)	0.47	0.06
	^{100}Pd(γ,α)	0.20	0.03		^{202}Pb(γ,n)	0.21	0.03
^{98}Ru	^{97}Ru(γ,n)	0.36	0.02	^{152}Gd	^{152}Dy(γ,α)	−0.40	−0.01
	^{100}Pd(γ,p)	0.62	0.04		^{154}Dy(γ,α)	−0.15	−0.00
	^{100}Pd(γ,α)	−0.51	−0.03		^{160}Er(γ,α)	0.39	0.00
^{102}Pd	^{100}Pd(γ,p)	−0.29	−0.05	^{156}Dy	^{159}Er(γ,n)	−0.18	−0.06
	^{100}Pd(γ,α)	−0.30	−0.05		^{160}Er(γ,α)	0.74	0.26
	^{103}Pd(γ,n)	−0.66	−0.12		^{202}Pb(γ,n)	0.18	0.05
^{106}Cd	^{107}Cd(γ,n)	−0.86	−0.16	^{158}Dy	^{158}Er(γ,α)	−0.23	−0.01
	^{110}Sn(γ,α)	0.23	0.05		^{160}Er(γ,α)	0.56	0.01
^{108}Cd	^{107}Cd(γ,n)	0.72	0.10		^{196}Pb(γ,n)	0.16	0.00
	^{109}Cd(γ,n)	−0.46	−0.06		^{202}Pb(γ,n)	0.18	0.00
	^{110}Sn(γ,p)	0.16	0.02	^{162}Er	^{159}Er(γ,n)	−0.18	−0.06
^{113}In	^{113}Sn(γ,n)	0.91	0.37		^{160}Er(γ,n)	−0.18	−0.06
^{112}Sn	^{110}Sn(γ,α)	−0.17	−0.03		^{160}Er(γ,α)	−0.26	−0.07
	^{113}Sn(γ,n)	−0.83	−0.15		^{161}Er(γ,n)	0.21	0.06
^{114}Sn	^{110}Sn(γ,α)	−0.15	−0.01		^{166}Yb(γ,α)	0.53	0.14
	^{113}Sn(γ,n)	0.74	0.06		^{196}Pb(γ,n)	0.25	0.07
	^{122}Xe(γ,n)	−0.18	−0.01		^{202}Pb(γ,n)	0.17	0.05
	^{122}Xe(γ,p)	0.20	0.02	^{164}Er	^{164}Yb(γ,n)	−0.24	−0.09
	^{122}Xe(γ,α)	0.41	0.04		^{164}Yb(γ,α)	−0.58	−0.32
^{115}Sn	^{113}Sn(γ,n)	0.80	0.05		^{196}Pb(γ,n)	0.17	0.05
	^{122}Xe(γ,p)	0.17	0.01	^{168}Yb	^{168}Hf(γ,α)	−0.28	−0.14
	^{122}Xe(γ,α)	0.35	0.02		^{172}Hf(γ,α)	0.60	0.24
^{120}Te	^{121}Te(γ,n)	−0.71	−0.09		^{176}W(γ,α)	0.20	0.07
	^{122}Xe(γ,p)	0.45	0.05		^{196}Pb(γ,n)	0.21	0.07

Continued on next page

Table 2.4 – continued from previous page

Isotope	Reaction	$\mathbf{r_P}$	ζ	Isotope	Reaction	$\mathbf{r_P}$	ζ
	^{122}Xe(γ,α)	-0.32	-0.04	^{174}Hf	^{174}W(γ,n)	-0.21	-0.03
^{124}Xe	^{122}Xe(γ,n)	-0.17	-0.04		^{174}W(γ,α)	-0.40	-0.08
	^{122}Xe(γ,p)	-0.24	-0.06		^{178}W(γ,n)	-0.15	-0.03
	^{122}Xe(γ,α)	-0.45	-0.15		^{178}W(γ,α)	0.42	0.07
	^{123}Xe(γ,n)	0.16	0.03	^{180}Ta	^{179}Ta(γ,n)	-0.91	-0.02
	^{125}Xe(γ,n)	-0.46	-0.16	^{180}W	^{180}Os(γ,n)	-0.28	-0.07
^{126}Xe	^{122}Xe(γ,α)	-0.34	-0.09		^{180}Os(γ,α)	-0.52	-0.21
	^{125}Xe(γ,n)	0.49	0.13		^{196}Pb(γ,n)	0.21	0.05
	^{127}Xe(γ,n)	-0.25	-0.07	^{184}Os	^{185}Os(γ,n)	0.33	0.02
	^{126}Ba(γ,p)	-0.18	-0.04		^{184}Pt(γ,α)	-0.44	-0.03
	^{126}Ba(γ,α)	-0.32	-0.09		^{186}Pt(γ,n)	0.17	0.01
^{130}Ba	^{126}Ba(γ,α)	-0.17	-0.01		^{186}Pt(γ,α)	-0.16	-0.01
	^{128}Ba(γ,n)	-0.19	-0.01		^{188}Pt(γ,n)	-0.17	-0.01
	^{129}Ba(γ,n)	0.23	0.01		^{196}Pb(γ,n)	0.16	0.01
	^{131}Ba(γ,n)	-0.79	-0.05	^{190}Pt	^{190}Hg(γ,n)	-0.28	-0.03
^{132}Ba	^{131}Ba(γ,n)	0.66	0.09		^{190}Hg(γ,α)	-0.51	-0.06
	^{133}Ba(γ,n)	-0.61	-0.08		^{196}Pb(γ,n)	0.20	0.02
^{138}La	^{137}La(γ,n)	-0.71	-0.37	^{196}Hg	^{196}Pb(γ,n)	-0.71	-0.41
^{136}Ce	^{138}Nd(γ,n)	-0.38	-0.05		^{197}Pb(γ,n)	-0.16	-0.06
	^{138}Nd(γ,p)	0.65	0.08		^{200}Pb(γ,n)	0.19	0.10
	^{138}Nd(γ,α)	-0.16	-0.02		^{202}Pb(γ,n)	0.30	0.14
	^{140}Nd(γ,α)	0.34	0.04				
^{138}Ce	^{137}Ce(γ,n)	0.51	0.02				
	^{139}Ce(γ,n)	-0.43	-0.01				
	^{139}Pr(γ,p)	0.29	0.01				
	^{138}Nd(γ,n)	-0.30	-0.01				
	^{138}Nd(γ,α)	-0.22	-0.01				

Table 2.5: Correlations and ζ slopes between mass fraction and reaction rates for the 3D-inspired mixing scenario.

Isotope	**Reaction**	$\mathbf{r_P}$	ζ	**Isotope**	**Reaction**	$\mathbf{r_P}$	ζ
^{74}Se	^{75}Se(γ,n)	-0.83	-0.22	^{152}Gd	^{150}Gd(γ,α)	-0.18	-0.00
^{78}Kr	^{79}Kr(γ,n)	-0.79	-0.24		^{151}Gd(γ,n)	-0.20	-0.00
^{84}Sr	^{85}Sr(γ,n)	-0.80	-0.34		^{152}Dy(γ,α)	-0.31	-0.01
^{92}Mo	^{93}Mo(γ,n)	-0.91	-0.14		^{154}Dy(γ,α)	-0.17	-0.00
^{94}Mo	^{93}Mo(γ,n)	0.93	0.10		^{160}Er(γ,α)	0.39	0.01
^{96}Ru	^{97}Ru(γ,n)	-0.82	-0.14		^{196}Pb(γ,n)	0.16	0.00
	^{100}Pd(γ,α)	0.21	0.04	^{156}Dy	^{157}Dy(γ,n)	-0.28	-0.12
^{98}Ru	^{97}Ru(γ,n)	0.50	0.02		^{159}Er(γ,n)	-0.17	-0.05
	^{100}Pd(γ,p)	0.58	0.03		^{160}Er(γ,α)	0.68	0.26
	^{100}Pd(γ,α)	-0.31	-0.01		^{196}Pb(γ,n)	0.16	0.05
	^{110}Sn(γ,α)	0.22	0.01	^{158}Dy	^{157}Dy(γ,n)	0.24	0.03
^{102}Pd	^{100}Pd(γ,p)	-0.18	-0.04		^{159}Dy(γ,n)	-0.21	-0.03
	^{100}Pd(γ,α)	-0.21	-0.04		^{159}Er(γ,n)	-0.17	-0.02
	^{103}Pd(γ,n)	-0.72	-0.16		^{160}Er(γ,α)	0.66	0.07
^{106}Cd	^{107}Cd(γ,n)	-0.75	-0.16		^{196}Pb(γ,n)	0.16	0.02
	^{110}Sn(γ,α)	0.31	0.07		^{202}Pb(γ,n)	0.20	0.02
^{108}Cd	^{107}Cd(γ,n)	0.20	0.05	^{162}Er	^{159}Er(γ,n)	-0.25	-0.10
	^{109}Cd(γ,n)	-0.83	-0.20		^{159}Er(γ,α)	-0.16	-0.05
^{113}In	^{114}In(γ,n)	-0.32	-0.05		^{160}Er(γ,n)	-0.23	-0.09
	^{110}Sn(γ,p)	-0.16	-0.02		^{160}Er(γ,α)	-0.44	-0.15
	^{110}Sn(γ,α)	-0.27	-0.04		^{161}Er(γ,n)	0.16	0.06
	^{113}Sn(γ,n)	0.60	0.10		^{166}Yb(γ,α)	0.33	0.11
	^{169}Lu(γ,n)	0.15	0.02		^{196}Pb(γ,n)	0.27	0.10
^{112}Sn	^{113}Sn(γ,n)	-0.80	-0.18		^{202}Pb(γ,n)	0.16	0.06
^{114}Sn	^{110}Sn(γ,α)	-0.17	-0.01	^{164}Er	^{164}Yb(γ,n)	-0.26	-0.07
	^{113}Sn(γ,n)	0.65	0.05		^{164}Yb(γ,α)	-0.56	-0.18
	^{122}Xe(γ,p)	0.21	0.02		^{196}Pb(γ,n)	0.21	0.06
	^{122}Xe(γ,α)	0.44	0.03		^{202}Pb(γ,n)	0.18	0.05
^{115}Sn	^{110}Sn(γ,α)	-0.16	-0.01	^{168}Yb	^{164}Yb(γ,α)	-0.19	-0.09
	^{113}Sn(γ,n)	0.74	0.06		^{166}Yb(γ,n)	-0.22	-0.08
	^{122}Xe(γ,p)	0.16	0.01		^{166}Yb(γ,α)	-0.38	-0.13
	^{122}Xe(γ,α)	0.33	0.03		^{167}Yb(γ,n)	0.20	0.07

Continued on next page

Table 2.5 – continued from previous page

Isotope	**Reaction**	$\mathbf{r_P}$	ζ	**Isotope**	**Reaction**	$\mathbf{r_P}$	ζ
^{120}Te	^{121}Te(γ,n)	−0.76	−0.19		^{172}Hf(γ,α)	0.43	0.16
	^{122}Xe(γ,p)	0.26	0.05		^{196}Pb(γ,n)	0.28	0.09
	^{122}Xe(γ,α)	−0.23	−0.05		^{202}Pb(γ,n)	0.19	0.06
^{124}Xe	^{122}Xe(γ,p)	−0.19	−0.05	^{174}Hf	^{172}Hf(γ,α)	−0.40	−0.07
	^{122}Xe(γ,α)	−0.39	−0.15		^{174}W(γ,α)	−0.19	−0.04
	^{125}Xe(γ,n)	−0.54	−0.23		^{178}W(γ,α)	0.51	0.09
^{126}Xe	^{122}Xe(γ,α)	−0.35	−0.14		^{182}Os(γ,α)	0.18	0.03
	^{125}Xe(γ,n)	0.22	0.09		^{196}Pb(γ,n)	0.19	0.03
	^{127}Xe(γ,n)	−0.63	−0.27	^{180}Ta	^{179}Ta(γ,n)	−0.91	−0.07
^{130}Ba	^{131}Ba(γ,n)	−0.82	−0.13		^{179}Ta(γ,α)	−0.15	−0.01
^{132}Ba	^{131}Ba(γ,n)	0.36	0.14	^{180}W	^{180}Os(γ,n)	−0.27	−0.05
	^{133}Ba(γ,n)	−0.76	−0.30		^{180}Os(γ,α)	−0.51	−0.13
^{138}La	^{133}La(γ,p)	−0.20	−0.07		^{196}Pb(γ,n)	0.23	0.04
	^{135}La(γ,n)	−0.35	−0.12	^{184}Os	^{182}Os(γ,α)	−0.38	−0.02
	^{136}La(γ,n)	0.26	0.08		^{184}Pt(γ,α)	−0.33	−0.02
	^{137}La(γ,n)	−0.34	−0.14		^{186}Pt(γ,α)	−0.15	−0.01
^{136}Ce	^{137}Ce(γ,n)	−0.49	−0.07		^{188}Pt(γ,α)	0.23	0.01
	^{138}Nd(γ,n)	−0.27	−0.03		^{196}Pb(γ,n)	0.19	0.01
	^{138}Nd(γ,p)	0.48	0.06	^{190}Pt	^{190}Hg(γ,n)	−0.30	−0.02
	^{140}Nd(γ,α)	0.38	0.04		^{190}Hg(γ,α)	−0.50	−0.05
^{138}Ce	^{137}Ce(γ,n)	0.65	0.07		^{196}Pb(γ,n)	0.20	0.02
	^{139}Ce(γ,n)	−0.52	−0.05	^{196}Hg	^{196}Pb(γ,n)	−0.68	−0.35
	^{138}Nd(γ,p)	0.16	0.01		^{197}Pb(γ,n)	−0.26	−0.10
^{144}Sm	^{142}Sm(γ,n)	−0.15	−0.02		^{200}Pb(γ,n)	0.17	0.07
	^{142}Sm(γ,p)	−0.16	−0.02		^{202}Pb(γ,n)	0.24	0.10
	^{143}Sm(γ,n)	−0.19	−0.03				
	^{146}Sm(γ,n)	0.19	0.03				
	^{146}Sm(γ,α)	−0.22	−0.03				
	^{150}Gd(γ,n)	0.21	0.03				
	^{150}Gd(γ,α)	−0.20	−0.03				
	^{196}Pb(γ,n)	0.46	0.06				
	^{202}Pb(γ,n)	0.20	0.03				

Table 2.6: Correlations and ζ slopes between mass fraction and reaction rates for the 3×3D-inspired mixing scenario.

Isotope	**Reaction**	$\mathbf{r_P}$	ζ	**Isotope**	**Reaction**	$\mathbf{r_P}$	ζ
^{74}Se	^{75}Se(γ,n)	-0.81	-0.24	^{144}Sm	^{142}Sm(γ,n)	-0.23	-0.02
^{78}Kr	^{79}Kr(γ,n)	-0.76	-0.20		^{142}Sm(γ,p)	-0.23	-0.03
^{84}Sr	^{85}Sr(γ,n)	-0.75	-0.26		^{143}Sm(γ,n)	-0.30	-0.04
^{92}Mo	^{93}Mo(γ,n)	-0.91	-0.23		^{146}Sm(γ,α)	-0.17	-0.02
^{94}Mo	^{93}Mo(γ,n)	0.92	0.17		^{150}Gd(γ,n)	0.17	0.02
^{96}Ru	^{97}Ru(γ,n)	-0.84	-0.25		^{150}Gd(γ,α)	-0.16	-0.02
^{98}Ru	^{97}Ru(γ,n)	0.65	0.05		^{196}Pb(γ,n)	0.44	0.05
	^{100}Pd(γ,p)	0.47	0.03		^{202}Pb(γ,n)	0.17	0.02
	^{100}Pd(γ,α)	-0.23	-0.02	^{152}Gd	^{151}Gd(γ,n)	-0.17	-0.00
	^{110}Sn(γ,α)	0.21	0.01		^{152}Dy(γ,α)	-0.39	-0.01
^{102}Pd	^{100}Pd(γ,p)	-0.20	-0.06		^{154}Dy(γ,α)	-0.19	-0.00
	^{100}Pd(γ,α)	-0.22	-0.06		^{160}Er(γ,α)	0.33	0.01
	^{103}Pd(γ,n)	-0.71	-0.26	^{156}Dy	^{157}Dy(γ,n)	-0.21	-0.08
^{106}Cd	^{107}Cd(γ,n)	-0.78	-0.27		^{159}Er(γ,n)	-0.18	-0.06
	^{110}Sn(γ,α)	0.21	0.08		^{160}Er(γ,α)	0.69	0.25
^{108}Cd	^{107}Cd(γ,n)	0.24	0.08		^{196}Pb(γ,n)	0.15	0.05
	^{109}Cd(γ,n)	-0.80	-0.24		^{202}Pb(γ,n)	0.15	0.05
^{113}In	^{110}Sn(γ,p)	-0.22	-0.04	^{158}Dy	^{157}Dy(γ,n)	0.20	0.02
	^{110}Sn(γ,α)	-0.33	-0.06		^{159}Er(γ,n)	-0.19	-0.02
	^{113}Sn(γ,n)	0.62	0.15		^{160}Er(γ,α)	0.67	0.07
	^{169}Lu(γ,n)	0.16	0.03		^{196}Pb(γ,n)	0.16	0.02
^{112}Sn	^{113}Sn(γ,n)	-0.78	-0.31		^{202}Pb(γ,n)	0.20	0.02
^{114}Sn	^{110}Sn(γ,p)	-0.17	-0.02	^{162}Er	^{159}Er(γ,n)	-0.29	-0.12
	^{110}Sn(γ,α)	-0.26	-0.03		^{159}Er(γ,α)	-0.17	-0.05
	^{113}Sn(γ,n)	0.70	0.08		^{160}Er(γ,n)	-0.22	-0.09
	^{122}Xe(γ,p)	0.16	0.02		^{160}Er(γ,α)	-0.40	-0.13
	^{122}Xe(γ,α)	0.27	0.03		^{161}Er(γ,n)	0.18	0.08
	^{169}Lu(γ,n)	0.15	0.01		^{166}Yb(γ,α)	0.32	0.11
^{115}Sn	^{110}Sn(γ,p)	-0.17	-0.02		^{196}Pb(γ,n)	0.27	0.10
	^{110}Sn(γ,α)	-0.25	-0.03		^{202}Pb(γ,n)	0.15	0.06
	^{113}Sn(γ,n)	0.73	0.08	^{164}Er	^{164}Yb(γ,n)	-0.24	-0.08
	^{122}Xe(γ,α)	0.24	0.03		^{164}Yb(γ,α)	-0.56	-0.24

Continued on next page

Table 2.6 – continued from previous page

Isotope	**Reaction**	$\mathbf{r_P}$	ζ	**Isotope**	**Reaction**	$\mathbf{r_P}$	ζ
	^{169}Lu(γ,n)	0.15	0.01		^{165}Yb(γ,n)	−0.17	−0.06
^{120}Te	^{121}Te(γ,n)	−0.78	−0.24		^{196}Pb(γ,n)	0.19	0.06
	^{122}Xe(γ,p)	0.24	0.06		^{202}Pb(γ,n)	0.15	0.06
	^{122}Xe(γ,α)	−0.22	−0.06	^{168}Yb	^{164}Yb(γ,α)	−0.22	−0.10
^{124}Xe	^{122}Xe(γ,p)	−0.20	−0.07		^{166}Yb(γ,n)	−0.18	−0.07
	^{122}Xe(γ,α)	−0.36	−0.18		^{166}Yb(γ,α)	−0.34	−0.12
	^{125}Xe(γ,n)	−0.54	−0.33		^{167}Yb(γ,n)	0.19	0.07
^{126}Xe	^{122}Xe(γ,p)	−0.19	−0.07		^{172}Hf(γ,α)	0.43	0.16
	^{122}Xe(γ,α)	−0.39	−0.18		^{196}Pb(γ,n)	0.29	0.10
	^{125}Xe(γ,n)	0.22	0.11		^{202}Pb(γ,n)	0.19	0.06
	^{127}Xe(γ,n)	−0.57	−0.29	^{174}Hf	^{172}Hf(γ,α)	−0.31	−0.06
^{130}Ba	^{126}Ba(γ,α)	−0.16	−0.02		^{174}W(γ,n)	−0.19	−0.03
	^{131}Ba(γ,n)	−0.81	−0.15		^{174}W(γ,α)	−0.30	−0.07
^{132}Ba	^{131}Ba(γ,n)	0.41	0.15		^{178}W(γ,α)	0.46	0.08
	^{133}Ba(γ,n)	−0.74	−0.27		^{182}Os(γ,α)	0.17	0.03
^{138}La	^{133}La(γ,p)	−0.19	−0.08		^{196}Pb(γ,n)	0.20	0.04
	^{135}La(γ,n)	−0.31	−0.12	^{180}Ta	^{179}Ta(γ,n)	−0.89	−0.07
	^{136}La(γ,n)	0.25	0.08	^{180}W	^{180}Os(γ,n)	−0.26	−0.08
	^{137}La(γ,n)	−0.35	−0.16		^{180}Os(γ,α)	−0.50	−0.21
^{136}Ce	^{137}Ce(γ,n)	−0.47	−0.07		^{181}Os(γ,n)	−0.16	−0.04
	^{138}Nd(γ,n)	−0.31	−0.04		^{196}Pb(γ,n)	0.22	0.06
	^{138}Nd(γ,p)	0.52	0.07	^{184}Os	^{182}Os(γ,α)	−0.19	−0.02
	^{140}Nd(γ,α)	0.32	0.04		^{185}Os(γ,n)	0.17	0.01
^{138}Ce	^{137}Ce(γ,n)	0.66	0.08		^{184}Pt(γ,α)	−0.45	−0.04
	^{139}Ce(γ,n)	−0.37	−0.04		^{186}Pt(γ,α)	−0.16	−0.01
	^{138}Nd(γ,n)	−0.16	−0.02		^{188}Pt(γ,α)	0.16	0.01
	^{138}Nd(γ,p)	0.28	0.03		^{196}Pb(γ,n)	0.20	0.01
	^{140}Nd(γ,α)	0.18	0.02	^{190}Pt	^{190}Hg(γ,n)	−0.30	−0.04
					^{190}Hg(γ,α)	−0.51	−0.07
					^{196}Pb(γ,n)	0.19	0.02
				^{196}Hg	^{196}Pb(γ,n)	−0.68	−0.42
					^{197}Pb(γ,n)	−0.28	−0.13
					^{202}Pb(γ,n)	0.20	0.10

Table 2.7: Correlations and ζ slopes between mass fraction and reaction rates for the 10×3D-inspired mixing scenario.

Isotope	**Reaction**	$\mathbf{r_P}$	ζ	**Isotope**	**Reaction**	$\mathbf{r_P}$	ζ
^{74}Se	^{75}Se(γ,n)	-0.87	-0.30	^{138}Ce	^{137}Ce(γ,n)	0.58	0.05
^{78}Kr	^{79}Kr(γ,n)	-0.81	-0.35		^{139}Ce(γ,n)	-0.19	-0.01
^{84}Sr	^{84}Rb(γ,n)	0.16	0.06		^{138}Nd(γ,n)	-0.31	-0.02
	^{85}Sr(γ,n)	-0.81	-0.33		^{138}Nd(γ,p)	0.37	0.03
^{92}Mo	^{93}Mo(γ,n)	-0.93	-0.17		^{138}Nd(γ,α)	-0.17	-0.01
^{94}Mo	^{93}Mo(γ,n)	0.94	0.21		^{140}Nd(γ,α)	0.20	0.01
^{96}Ru	^{97}Ru(γ,n)	-0.88	-0.25	^{144}Sm	^{142}Sm(γ,n)	-0.31	-0.04
^{98}Ru	^{97}Ru(γ,n)	0.68	0.07		^{142}Sm(γ,p)	-0.29	-0.03
	^{100}Pd(γ,p)	0.45	0.05		^{143}Sm(γ,n)	-0.41	-0.05
	^{100}Pd(γ,α)	-0.29	-0.03		^{196}Pb(γ,n)	0.35	0.04
	^{110}Sn(γ,α)	0.18	0.02	^{152}Gd	^{152}Dy(γ,α)	-0.50	-0.02
^{102}Pd	^{100}Pd(γ,p)	-0.29	-0.08		^{154}Dy(γ,α)	-0.16	-0.00
	^{100}Pd(γ,α)	-0.30	-0.08		^{158}Er(γ,n)	0.15	0.00
	^{103}Pd(γ,n)	-0.65	-0.21		^{160}Er(γ,α)	0.19	0.00
^{106}Cd	^{107}Cd(γ,n)	-0.83	-0.30	^{156}Dy	^{159}Er(γ,n)	-0.19	-0.06
	^{110}Sn(γ,α)	0.19	0.07		^{160}Er(γ,α)	0.70	0.26
^{108}Cd	^{107}Cd(γ,n)	0.63	0.15		^{202}Pb(γ,n)	0.16	0.05
	^{109}Cd(γ,n)	-0.50	-0.10	^{158}Dy	^{159}Dy(γ,n)	0.19	0.01
^{113}In	^{110}Sn(γ,p)	-0.17	-0.05		^{158}Er(γ,n)	-0.16	-0.01
	^{110}Sn(γ,α)	-0.24	-0.08		^{158}Er(γ,α)	-0.28	-0.01
	^{113}Sn(γ,n)	0.82	0.34		^{159}Er(γ,n)	-0.18	-0.01
^{112}Sn	^{110}Sn(γ,α)	-0.17	-0.05		^{160}Er(γ,α)	0.56	0.02
	^{113}Sn(γ,n)	-0.78	-0.33		^{196}Pb(γ,n)	0.17	0.01
^{114}Sn	^{110}Sn(γ,p)	-0.18	-0.02		^{202}Pb(γ,n)	0.17	0.01
	^{110}Sn(γ,α)	-0.27	-0.04	^{162}Er	^{159}Er(γ,n)	-0.28	-0.10
	^{113}Sn(γ,n)	0.76	0.12		^{159}Er(γ,α)	-0.16	-0.05
	^{122}Xe(γ,α)	0.15	0.03		^{160}Er(γ,n)	-0.19	-0.07
	^{169}Lu(γ,n)	0.16	0.02		^{160}Er(γ,α)	-0.29	-0.09
^{115}Sn	^{110}Sn(γ,p)	-0.18	-0.02		^{161}Er(γ,n)	0.18	0.06
	^{110}Sn(γ,α)	-0.27	-0.04		^{166}Yb(γ,α)	0.40	0.12
	^{113}Sn(γ,n)	0.77	0.12		^{196}Pb(γ,n)	0.26	0.09
	^{169}Lu(γ,n)	0.16	0.02		^{202}Pb(γ,n)	0.15	0.05

Continued on next page

Table 2.7 – continued from previous page

Isotope	**Reaction**	$\mathbf{r_P}$	ζ	**Isotope**	**Reaction**	$\mathbf{r_P}$	ζ
^{120}Te	^{119}Te(γ,n)	−0.20	−0.04	^{164}Er	^{164}Yb(γ,n)	−0.23	−0.10
	^{121}Te(γ,n)	−0.66	−0.13		^{164}Yb(γ,α)	−0.59	−0.43
	^{122}Xe(γ,p)	0.42	0.07		^{165}Yb(γ,n)	−0.17	−0.09
	^{122}Xe(γ,α)	−0.35	−0.06		^{196}Pb(γ,n)	0.16	0.07
^{124}Xe	^{122}Xe(γ,n)	−0.22	−0.08	^{168}Yb	^{168}Hf(γ,n)	−0.16	−0.05
	^{122}Xe(γ,p)	−0.27	−0.10		^{168}Hf(γ,α)	−0.40	−0.21
	^{122}Xe(γ,α)	−0.44	−0.23		^{169}Hf(γ,n)	−0.17	−0.05
	^{125}Xe(γ,n)	−0.40	−0.22		^{172}Hf(γ,α)	0.41	0.19
^{126}Xe	^{122}Xe(γ,n)	−0.21	−0.06		^{196}Pb(γ,n)	0.22	0.08
	^{122}Xe(γ,p)	−0.26	−0.08	^{174}Hf	^{174}W(γ,n)	−0.23	−0.06
	^{122}Xe(γ,α)	−0.46	−0.19		^{174}W(γ,α)	−0.52	−0.19
	^{125}Xe(γ,n)	0.38	0.16		^{176}W(γ,α)	−0.15	−0.05
	^{127}Xe(γ,n)	−0.26	−0.11	^{180}Ta	^{179}Ta(γ,n)	−0.88	−0.03
^{130}Ba	^{126}Ba(γ,p)	−0.18	−0.02	^{180}W	^{180}Os(γ,n)	−0.30	−0.12
	^{126}Ba(γ,α)	−0.31	−0.03		^{180}Os(γ,α)	−0.54	−0.39
	^{128}Ba(γ,n)	−0.26	−0.03		^{196}Pb(γ,n)	0.21	0.08
	^{128}Ba(γ,p)	−0.16	−0.01	^{184}Os	^{184}Pt(γ,α)	−0.49	−0.10
	^{128}Ba(γ,α)	−0.27	−0.02		^{185}Pt(γ,α)	−0.16	−0.02
	^{129}Ba(γ,n)	0.21	0.02		^{196}Pb(γ,n)	0.16	0.02
	^{131}Ba(γ,n)	−0.51	−0.05	^{190}Pt	^{190}Hg(γ,n)	−0.27	−0.06
^{132}Ba	^{128}Ba(γ,α)	−0.18	−0.02		^{190}Hg(γ,α)	−0.52	−0.15
	^{131}Ba(γ,n)	0.63	0.12		^{196}Pb(γ,n)	0.18	0.04
	^{133}Ba(γ,n)	−0.56	−0.10	^{196}Hg	^{196}Pb(γ,n)	−0.75	−0.53
^{138}La	^{137}La(γ,n)	−0.65	−0.35		^{202}Pb(γ,n)	0.20	0.12
^{136}Ce	^{138}Nd(γ,n)	−0.39	−0.06				
	^{138}Nd(γ,p)	0.65	0.10				
	^{138}Nd(γ,α)	−0.16	−0.03				
	^{140}Nd(γ,α)	0.31	0.05				

Table 2.8: Correlations and ζ slopes between mass fraction and reaction rates for the 50×3D-inspired mixing scenario.

Isotope	**Reaction**	$\mathbf{r_P}$	ζ	**Isotope**	**Reaction**	$\mathbf{r_P}$	ζ
^{74}Se	^{75}Se(γ,n)	−0.95	−0.10	^{130}Ba	^{126}Ba(γ,α)	−0.19	−0.01
^{78}Kr	^{79}Kr(γ,n)	−0.91	−0.28		^{132}Ce(γ,n)	−0.23	−0.01
^{84}Sr	^{85}Sr(γ,n)	−0.92	−0.26		^{132}Ce(γ,p)	0.32	0.01
^{92}Mo	^{93}Mo(γ,n)	−0.57	−0.03		^{132}Ce(γ,α)	−0.20	−0.01
	^{100}Pd(γ,p)	0.19	0.01		^{134}Ce(γ,n)	−0.20	−0.01
	^{100}Pd(γ,α)	0.20	0.01		^{134}Ce(γ,α)	0.41	0.02
	^{110}Sn(γ,n)	0.16	0.01	^{132}Ba	^{132}Ce(γ,n)	−0.28	−0.04
	^{110}Sn(γ,p)	0.23	0.01		^{132}Ce(γ,p)	−0.25	−0.03
	^{110}Sn(γ,α)	0.37	0.02		^{132}Ce(γ,α)	−0.31	−0.04
^{94}Mo	^{93}Mo(γ,n)	0.89	0.08		^{133}Ce(γ,n)	−0.19	−0.03
^{96}Ru	^{97}Ru(γ,n)	−0.62	−0.05		^{134}Ce(γ,α)	−0.18	−0.02
	^{97}Ru(γ,α)	−0.18	−0.01	^{138}La	^{137}La(γ,n)	−0.75	−0.45
	^{100}Pd(γ,α)	0.33	0.03	^{136}Ce	^{138}Nd(γ,n)	−0.42	−0.09
	^{110}Sn(γ,n)	0.16	0.01		^{138}Nd(γ,p)	0.66	0.14
	^{110}Sn(γ,p)	0.16	0.01		^{140}Nd(γ,α)	0.25	0.06
	^{110}Sn(γ,α)	0.23	0.02	^{138}Ce	^{138}Nd(γ,n)	−0.33	−0.04
^{98}Ru	^{100}Pd(γ,p)	0.70	0.13		^{138}Nd(γ,p)	−0.31	−0.04
	^{100}Pd(γ,α)	−0.53	−0.10		^{138}Nd(γ,α)	−0.24	−0.02
^{102}Pd	^{100}Pd(γ,p)	−0.39	−0.06		^{139}Nd(γ,n)	−0.31	−0.04
	^{100}Pd(γ,α)	−0.38	−0.05	^{144}Sm	^{142}Sm(γ,n)	−0.36	−0.06
	^{103}Pd(γ,n)	−0.23	−0.04		^{142}Sm(γ,p)	−0.29	−0.04
	^{104}Cd(γ,p)	0.17	0.03		^{143}Sm(γ,n)	−0.50	−0.09
	^{104}Cd(γ,α)	−0.27	−0.04		^{196}Pb(γ,n)	0.19	0.03
^{106}Cd	^{104}Cd(γ,p)	−0.23	−0.03	^{152}Gd	^{152}Dy(γ,α)	−0.50	−0.05
	^{107}Cd(γ,n)	−0.62	−0.07		^{158}Er(γ,n)	0.18	0.01
	^{110}Sn(γ,p)	0.20	0.02	^{156}Dy	^{156}Er(γ,α)	−0.44	−0.27
	^{110}Sn(γ,α)	0.40	0.05		^{158}Er(γ,n)	0.19	0.09
^{108}Cd	^{107}Cd(γ,n)	0.61	0.11		^{158}Er(γ,α)	−0.18	−0.07
	^{110}Sn(γ,p)	0.49	0.08		^{160}Er(γ,α)	0.25	0.15
	^{110}Sn(γ,α)	−0.33	−0.06	^{158}Dy	^{158}Er(γ,n)	−0.28	−0.02
^{113}In	^{113}Sn(γ,n)	0.94	0.44		^{158}Er(γ,α)	−0.53	−0.05
^{112}Sn	^{110}Sn(γ,p)	−0.25	−0.03	^{162}Er	^{162}Yb(γ,α)	−0.49	−0.30

Continued on next page

Table 2.8 – continued from previous page

Isotope	**Reaction**	$\mathbf{r_P}$	ζ	**Isotope**	**Reaction**	$\mathbf{r_P}$	ζ
	^{110}Sn(γ,α)	−0.34	−0.04		^{164}Yb(γ,α)	−0.16	−0.07
	^{113}Sn(γ,n)	−0.65	−0.08		^{168}Hf(γ,n)	0.17	0.07
^{114}Sn	^{110}Sn(γ,α)	−0.21	−0.02	^{164}Er	^{164}Yb(γ,n)	−0.31	−0.17
	^{113}Sn(γ,n)	0.78	0.08		^{164}Yb(γ,α)	−0.56	−0.51
	^{122}Xe(γ,n)	−0.28	−0.03		^{202}Pb(γ,n)	0.16	0.09
	^{122}Xe(γ,p)	0.16	0.02	^{168}Yb	^{168}Hf(γ,n)	−0.28	−0.12
	^{122}Xe(γ,α)	0.23	0.03		^{168}Hf(γ,α)	−0.55	−0.57
	^{169}Lu(γ,n)	0.15	0.01	^{174}Hf	^{174}W(γ,n)	−0.30	−0.13
^{115}Sn	^{110}Sn(γ,α)	−0.21	−0.02		^{174}W(γ,α)	−0.53	−0.37
	^{113}Sn(γ,n)	0.80	0.08	^{180}Ta	^{179}Ta(γ,n)	−0.87	−0.00
	^{122}Xe(γ,n)	−0.27	−0.03	^{180}W	^{180}Os(γ,n)	−0.38	−0.21
	^{122}Xe(γ,p)	0.15	0.02		^{180}Os(γ,α)	−0.52	−0.46
	^{122}Xe(γ,α)	0.22	0.03		^{196}Pb(γ,n)	0.19	0.11
	^{169}Lu(γ,n)	0.15	0.01	^{184}Os	^{184}Pt(γ,n)	−0.16	−0.05
^{120}Te	^{120}Xe(γ,α)	−0.22	−0.05		^{184}Pt(γ,α)	−0.55	−0.29
	^{122}Xe(γ,p)	0.58	0.11		^{196}Pb(γ,n)	0.16	0.04
	^{122}Xe(γ,α)	−0.49	−0.10	^{190}Pt	^{190}Hg(γ,n)	−0.30	−0.13
^{124}Xe	^{122}Xe(γ,n)	−0.28	−0.10		^{190}Hg(γ,α)	−0.49	−0.30
	^{122}Xe(γ,p)	−0.31	−0.11		^{196}Pb(γ,n)	0.20	0.08
	^{122}Xe(γ,α)	−0.43	−0.21	^{196}Hg	^{196}Pb(γ,n)	−0.76	−0.60
	^{123}Xe(γ,n)	0.18	0.06		^{202}Pb(γ,n)	0.18	0.11
^{126}Xe	^{126}Ba(γ,p)	−0.35	−0.17				
	^{126}Ba(γ,α)	−0.48	−0.32				
	^{127}Ba(γ,n)	−0.22	−0.12				

Chapter 3

Investigations Beyond the *p* Nuclei

The work presented in Section 3.1 presents the preliminary results of exploratory research done on the light odd-Z elements produced in O-C shell mergers solely by myself. The work presented in Section 3.2 presents the preliminary results of collaborative research done with Dr. Falk Herwig on the advective-reactive *r*-process around a black hole.

3.1 Light Odd-Z Isotope Production

The *p*-nuclei are not the sole unique nucleosynthetic feature of O-C shell mergers. The light odd-Z elements P, Cl, K, and Sc have also been noted as products during the merger (Ritter et al., 2018a; Roberti et al., 2025). These elements are of interest because they are underproduced in galactic chemical evolution calculations (Ritter et al., 2018a), there are observations of P-enhanced stars (Masseron et al., 2020; Brauner et al., 2023, 2024), and K in particular is relevant for the habitability of exoplanets. This is because ^{40}K is a radionuclide that contributes significantly to the heating of an exoplanet's mantle and impacts the tectonics of the planet and its atmosphere composition Frank et al. (2014); O'Neill et al. (2020).

Using the same models described in Chapter 2, I present the preliminary results of how the light odd-Z elements are produced in O-C shell mergers.

As Figure 3.1 shows, the light odd-Z elements are all clearly affected by the presence of a convective downturn. Similar to the *p*-nuclei, the impact is non-monotonic and non-linear, as ^{31}P, ^{35}Cl, ^{40}K, and ^{45}Sc all decrease in production at the fastest mixing speeds. K and Sc show the most significant impact from the convective downturn with a spread in production of $1.5 - 2$ orders of magnitude.

Further, comparing the total elemental production of the light odd-Z elements shows that there can be a monotonic relationship between the final production, mixing speeds,

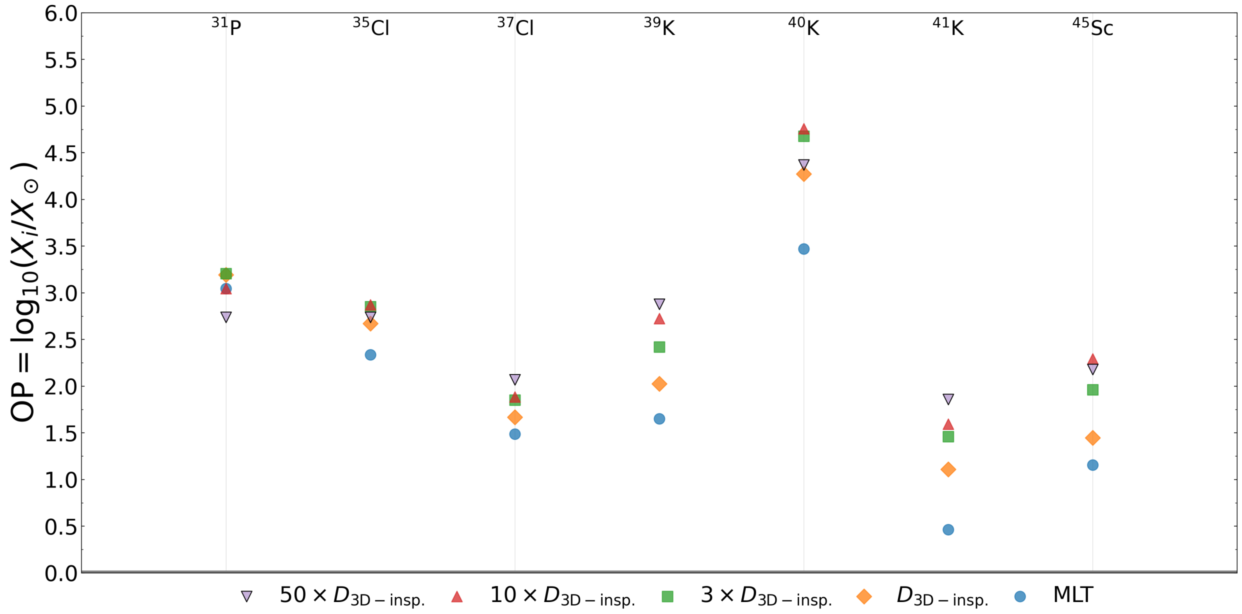

Figure 3.1: Impact on the production of the light odd-Z stable isotopes of P, Cl, K, and Sc comparing MLT and convective dowturn models.

and ingestion rate. Figures 3.2 and 3.3 show the MLT and convective mixing downturn scenarios in square bracket notation and the MLT mixing scenario with different ingestion rates, respectively. As it can be seen, as mixing speeds increase, the total production of [K/Ar] and [Ne/O] decrease, but as ingestion rate of C-shell material increases, the total production of [K/Ar] and [Ne/O] increases. This behaviour is not shared across all elements, but points to further need to research the impact of mixing conditions on nucleosynthesis in O-C shell mergers.

3.2 Advective-Reactive r process

Advective-reactive nucleosynthesis is the generalization of the convective-reactive framework to include transport of material beyond convection. In this work, Dr. Herwig and I took `SkyNet` post-processed trajectories that escaped a black hole formed by neutron star mergers from Dr. Rodrigo Fernandez (priv. com.) to determine whether the advective-reactive framework is relevant to r-process nucleosynthesis.

Over time, the distance between any two trajectories increases as they move away from the black hole. That means there is a time limit on how long the trajectories are able to exchange material. We define a distance L_{mix} analogously to ℓ_{mix} and if any two trajectories

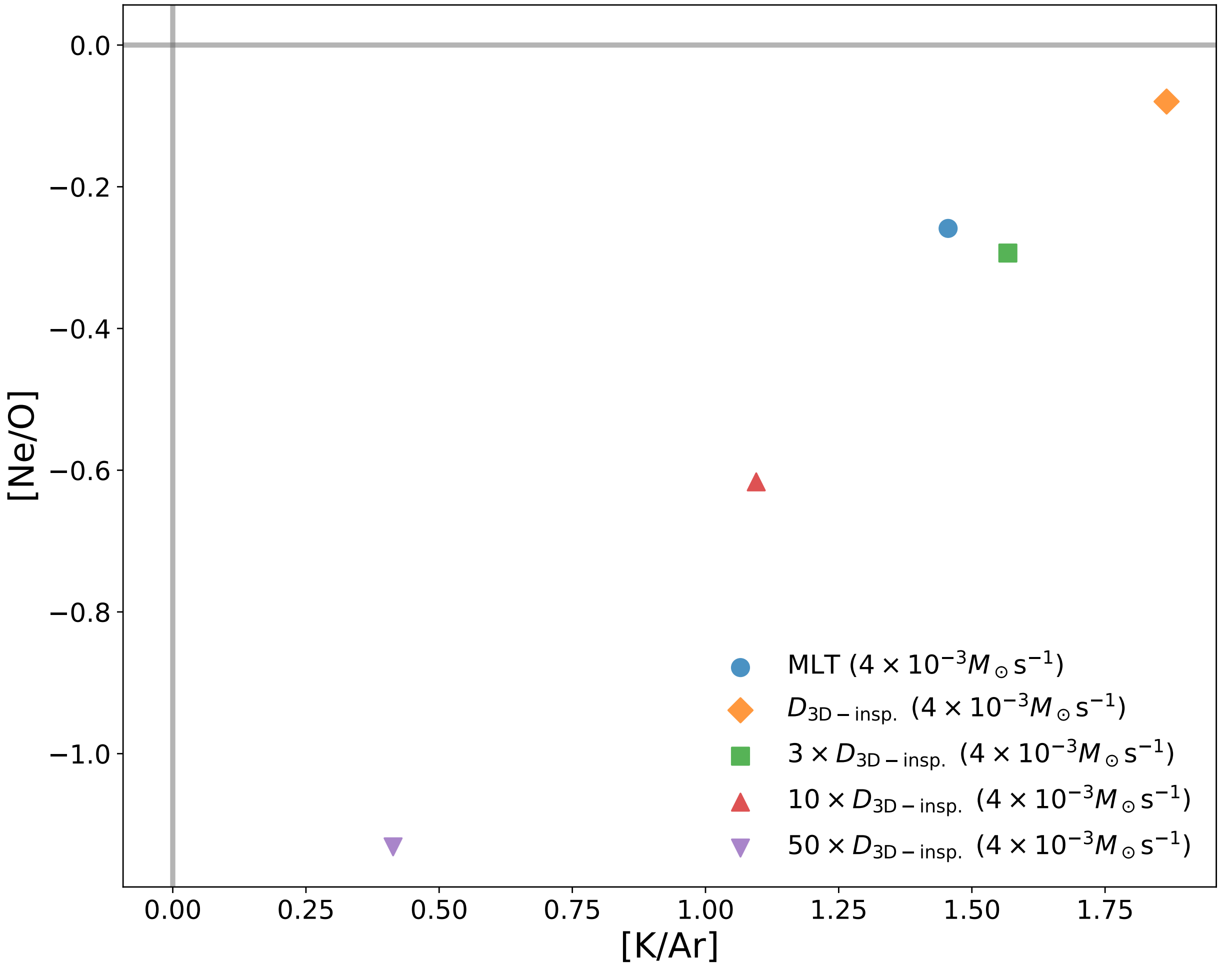

Figure 3.2: The MLT and convective mixing downturn scenarios in square bracket notation.

are within this distance can exchange material.

$$L_{\mathrm{mix}} = \sqrt{D t_{\mathrm{nuc}}} \tag{3.1}$$

where $D = 3 \times 10^{16}$ cm^2/s is the diffusion coefficient and t_{nuc} was given an analytic form based on a linear fitting of $\tau = X/(dX/dt)$ vs t plots for some n-heavy In isotopes. From this, we get L_{mix} as a function of time. Not only do trajectories need to be within a mixing distance, they also need to be within this distance for a sufficient amount of time to exchange material. We define that if two trajectories are within $L_{\mathrm{mix}}(t)$ of each other for $t = t_{\mathrm{mix}}$, then they have exchanged material. Since there is some ambiguity in the definition of t_{mix}, we consider five cases of 0.25, 0.5, 0.75, 1, and 1.5 times $L_{\mathrm{mix}}(t)$. The results of this analysis are shown in Figure 3.4 which shows that 7.5-15% of trajectories could be able to exchange

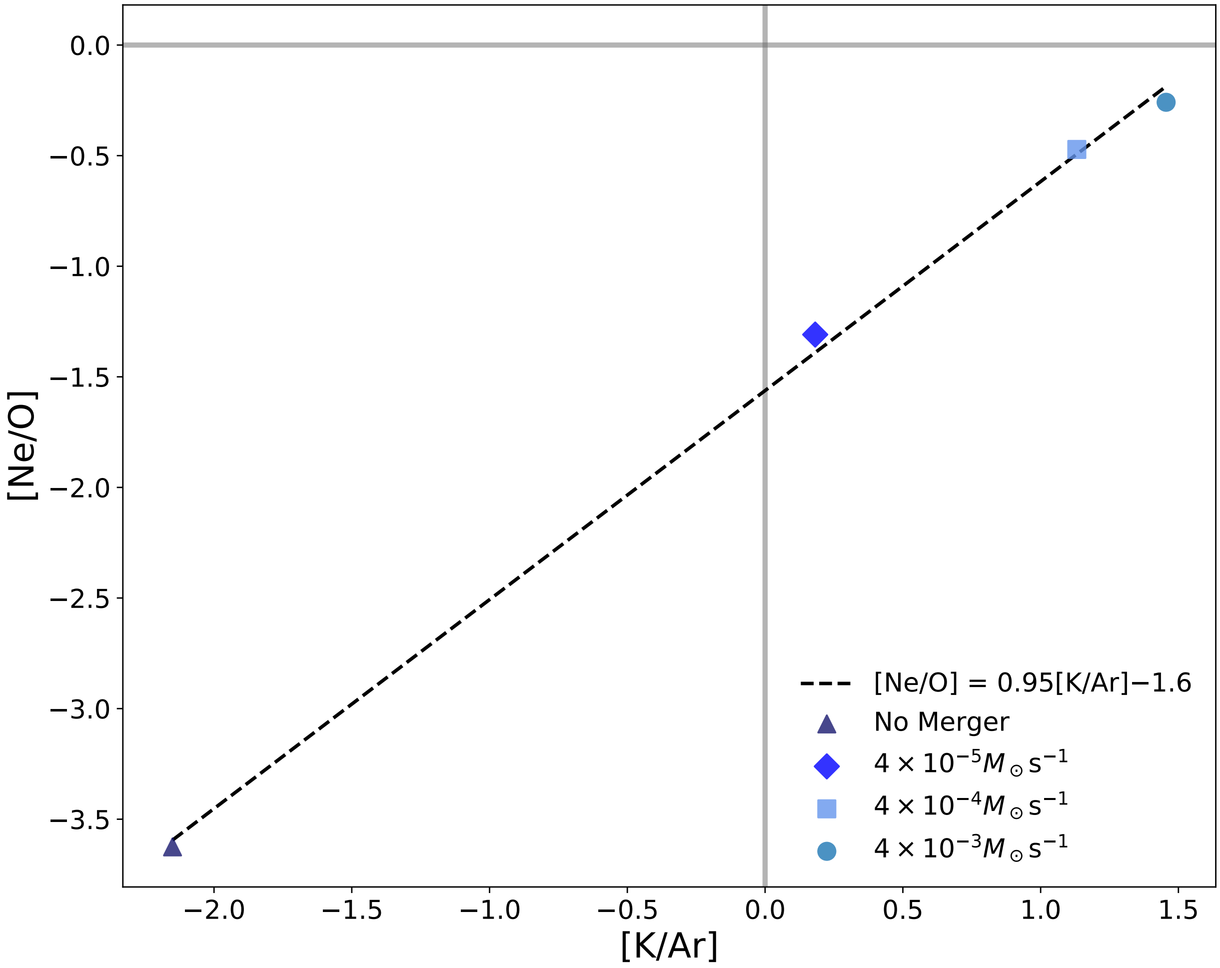

Figure 3.3: The MLT mixing scenario with different ingestion rates in square bracket notation.

material for the optimistic cases.

Much more work needs to be done to understand whether this analysis reveals anything impactful for r-process nucleosynthesis. If all nearby trajectories are in nuclear static equilibrium, then it is likely that there is no significnat difference in the final production.

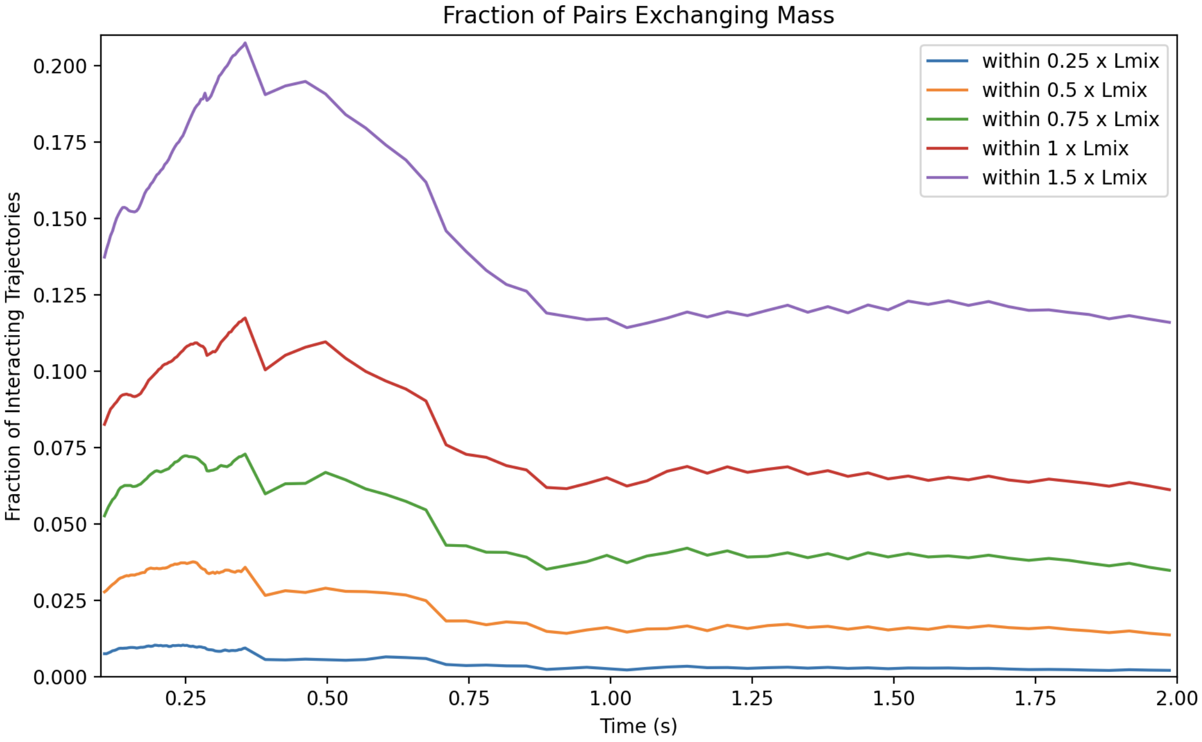

Figure 3.4: Fraction of trajectories with distance for enough time to exchange mass. Each coloured line represents a size for L_{mix}.

Chapter 4

Summary and Conclusion

4.1 Mixing, Nuclear Physics, and the p Nuclei

In this work, I have explored how changing the mixing assumptions made in 1D stellar evolution models can have a significant impact on the final nucleosynthesis of the p nuclei in O-C shell mergers. I have shown that the convective mixing downturn, which is a feature of 3D hydrodynamic simulations, can have a significant impact on the nucleosynthesis of the p nuclei. The convective mixing downturn leads to a non-monotonic and non-linear impact on the production of the p nuclei, with isotopes of the same element being effected differently, which has direct implications for grains analysis. I have also shown that the impact of the C-shell entrainment rate is also significant. While most species are uniformly boosted by the entrainment, the large variation depending on the true entrainment rate means that there exists large uncertainties there. Potential convective quenching in the profile either GOSH-like at peak Ne-burning or at the top of the shell due to hydrodynamic feedback only partially merging the O- and C-shells decrease the production of the p nuclei also was shown. Finally, I have shown that while the impact from varying the input nuclear physics has a comparable impact to any individual mixing scenario, different scenearios result in different nuclear physics impacts. Addtionally, whether a species and reaction rate are correlated is largely dependent on the mixing scenario with few shared correlated rates. This demonstrates the importance of understanding the mixing conditions in the O-C shell merger environment to accurately model the nucleosynthesis of the p nuclei.

4.2 Light Odd-Z Isotopes and Macrophysics

Although the work is preliminary, current results show that the light odd-Z elements are also significantly impacted by the 1D mixing asssumptions showing all the same features as the *p* nuclei. This shows the importance of understanding the mixing conditions in O-C shell mergers for nucleosynthesis generically, and not just the *p* nuclei. The convective-reactive environment is a complex scenario for nucleosynthesis, and this emphasizes the importance of understanding and connecting 3D hydrodynamic simulations to nucleosynthesis.

Bibliography

Andrassy, R., Herwig, F., Woodward, P., and Ritter, C. (2020). 3D hydrodynamic simulations of C ingestion into a convective O shell. *Monthly Notices of the Royal Astronomical Society*, 491:972–992.

Arcones, A. and Montes, F. (2011). Production of Light-element Primary Process Nuclei in Neutrino-driven Winds. *The Astrophysical Journal*, 731:5.

Arnett, W. D. and Meakin, C. (2011). Toward Realistic Progenitors of Core-collapse Supernovae. *The Astrophysical Journal*, 733:78.

Arnett, W. D., Meakin, C., Hirschi, R., Cristini, A., Georgy, C., Campbell, S., Scott, L. J. A., Kaiser, E. A., Viallet, M., and Mocák, M. (2019). 3D Simulations and MLT. I. Renzini's Critique. *The Astrophysical Journal*, 882:18.

Arnould, M. (1976). Possibility of synthesis of proton-rich nuclei in highly evolved stars. II. *Astronomy and Astrophysics*, 46:117–125.

Arnould, M. and Goriely, S. (2003). The p-process of stellar nucleosynthesis: Astrophysics and nuclear physics status. *Physics Reports*, 384(1):1–84.

Arnould, M., Goriely, S., and Takahashi, K. (2007). The r-process of stellar nucleosynthesis: Astrophysics and nuclear physics achievements and mysteries. *Physics Reports*, 450:97–213.

Battino, U., Pignatari, M., Travaglio, C., Lederer-Woods, C., Denissenkov, P., Herwig, F., Thielemann, F., and Rauscher, T. (2020). Heavy elements nucleosynthesis on accreting white dwarfs: Building seeds for the p-process. *Monthly Notices of the Royal Astronomical Society*, 497:4981–4998.

Battino, U., Tattersall, A., Lederer-Woods, C., Herwig, F., Denissenkov, P., Hirschi, R., Trappitsch, R., den Hartogh, J. W., Pignatari, M., and NuGrid Collaboration (2019).

NuGrid stellar data set - III. Updated low-mass AGB models and s-process nucleosynthesis with metallicities Z= 0.01, Z = 0.02, and Z = 0.03. *Monthly Notices of the Royal Astronomical Society*, 489:1082–1098.

Bazan, G. and Arnett, D. (1994). Convection, Nucleosynthesis, and Core Collapse. *The Astrophysical Journal*, 433:L41.

Bisterzo, S., Gallino, R., Straniero, O., Cristallo, S., and Käppeler, F. (2011). The s-process in low-metallicity stars - II. Interpretation of high-resolution spectroscopic observations with asymptotic giant branch models. *Monthly Notices of the Royal Astronomical Society*, 418:284–319.

Böhm-Vitense, E. (1958). Über die Wasserstoffkonvektionszone in Sternen verschiedener Effektivtemperaturen und Leuchtkräfte. Mit 5 Textabbildungen. *Zeitschrift fur Astrophysik*, 46:108.

Brauner, M., Masseron, T., García-Hernández, D. A., Pignatari, M., Womack, K. A., Lugaro, M., and Hayes, C. R. (2023). Unveiling the chemical fingerprint of phosphorus-rich stars: I. In the infrared region of APOGEE-2. *Astronomy & Astrophysics*, 673:A123.

Brauner, M., Pignatari, M., Masseron, T., García-Hernández, D. A., and Lugaro, M. (2024). Unveiling the chemical fingerprint of phosphorus-rich stars II. Heavy-element abundances from UVES/VLT spectra.

Burbidge, E. M., Burbidge, G. R., Fowler, W. A., and Hoyle, F. (1957). Synthesis of the Elements in Stars. *Reviews of Modern Physics*, 29(4):547–650.

Chapman, S. (1961). Scale Times and Scale Lengths of Variables: With Geomagnetic and Ionospheric Illustrations. *Proceedings of the Physical Society*, 77:424–432.

Choplin, A., Goriely, S., Hirschi, R., Tominaga, N., and Meynet, G. (2022). The p-process in exploding rotating massive stars. *Astronomy and Astrophysics*, 661:A86.

Choplin, A., Siess, L., and Goriely, S. (2021). The intermediate neutron capture process - I. Development of the i-process in low-metallicity low-mass AGB stars. *Astronomy & Astrophysics*, 648:A119.

Collins, C., Müller, B., and Heger, A. (2018). Properties of convective oxygen and silicon burning shells in supernova progenitors. *Monthly Notices of the Royal Astronomical Society*, 473:1695–1704.

Courant, R., Friedrichs, K., and Lewy, H. (1928). Über die partiellen Differenzengleichungen der mathematischen Physik. *Mathematische Annalen*, 100(1):32–74.

Cowan, J. J. and Rose, W. K. (1977). Production of 14C and neutrons in red giants. *The Astrophysical Journal*, 212:149–158.

Cox, J. P. and Giuli, R. T. (1968). *Principles of Stellar Structure*. Gordon and Breach Science Publishers.

Denissenkov, P., Perdikakis, G., Herwig, F., Schatz, H., Ritter, C., Pignatari, M., Jones, S., Nikas, S., and Spyrou, A. (2018). The impact of (n, γ) reaction rate uncertainties of unstable isotopes near N = 50 on the i-process nucleosynthesis in He-shell flash white dwarfs. *Journal of Physics G Nuclear Physics*, 45:055203.

Denissenkov, P. A., Herwig, F., Perdikakis, G., and Schatz, H. (2021). The impact of (n,γ) reaction rate uncertainties of unstable isotopes on the i-process nucleosynthesis of the elements from Ba to W. *Monthly Notices of the Royal Astronomical Society*, 503:3913–3925.

Dillmann, I., Rauscher, T., Heil, M., Käppeler, F., Rapp, W., and Thielemann, F. K. (2008). P-Process simulations with a modified reaction library. *Journal of Physics G Nuclear Physics*, 35:014029.

Dimotakis, P. E. (2005). Turbulent Mixing. *Annual Review of Fluid Mechanics*, 37:329–356.

Fok, H. K., Pignatari, M., Côté, B., and Trappitsch, R. (2024). Silicon Isotopic Composition of Mainstream Presolar SiC Grains Revisited: The Impact of Nuclear Reaction Rate Uncertainties. *The Astrophysical Journal*, 977:L24.

Frank, E. A., Meyer, B. S., and Mojzsis, S. J. (2014). A radiogenic heating evolution model for cosmochemically Earth-like exoplanets. *Icarus*, 243:274–286.

Freytag, B., Ludwig, H. G., and Steffen, M. (1996). Hydrodynamical models of stellar convection. The role of overshoot in DA white dwarfs, A-type stars, and the Sun. *Astronomy and Astrophysics*, 313:497–516.

Fröhlich, C., Martínez-Pinedo, G., Liebendörfer, M., Thielemann, F. K., Bravo, E., Hix, W. R., Langanke, K., and Zinner, N. T. (2006). Neutrino-Induced Nucleosynthesis of A>64 Nuclei: The Np Process. *Physical Review Letters*, 96:142502.

Goriely, S., Arnould, M., Borzov, I., and Rayet, M. (2001). The puzzle of the synthesis of the rare nuclide 138La. *Astronomy and Astrophysics*, 375:L35–L38.

Goriely, S., Bauswein, A., Just, O., Pllumbi, E., and Janka, H.-T. (2015). Impact of weak interactions of free nucleons on the r-process in dynamical ejecta from neutron star mergers. *Monthly Notices of the Royal Astronomical Society*, 452(4):3894–3904.

Goriely, S., José, J., Hernanz, M., Rayet, M., and Arnould, M. (2002). He-detonation in sub-Chandrasekhar CO white dwarfs: A new insight into energetics and p-process nucleosynthesis. *Astronomy and Astrophysics*, 383:L27–L30.

Hashimoto, M., Nomoto, K., and Shigeyama, T. (1989). Explosive nucleosynthesis in supernova 1987A. *Astronomy and Astrophysics*, 210:L5–L8.

Henyey, L. G., Forbes, J. E., and Gould, N. L. (1964). A New Method of Automatic Computation of Stellar Evolution. *The Astrophysical Journal*, 139:306.

Herwig, F. (2000). The evolution of AGB stars with convective overshoot.

Herwig, F. (2013). Evolution of Solar and Intermediate-Mass Stars. In Oswalt, T. D. and Barstow, M. A., editors, *Planets, Stars and Stellar Systems: Volume 4: Stellar Structure and Evolution*, pages 397–445. Springer Netherlands, Dordrecht.

Herwig, F., Blöcker, T., Langer, N., and Driebe, T. (1999). On the formation of hydrogen-deficient post-AGB stars.

Herwig, F., Freytag, B., Hueckstaedt, R. M., and Timmes, F. X. (2006). Hydrodynamic Simulations of He Shell Flash Convection. *The Astrophysical Journal*, 642(2):1057.

Herwig, F., Pignatari, M., Woodward, P. R., Porter, D. H., Rockefeller, G., Fryer, C. L., Bennett, M., and Hirschi, R. (2011). CONVECTIVE–REACTIVE PROTON–12C COMBUSTION IN SAKURAI'S OBJECT (V4334 SAGITTARII) AND IMPLICATIONS FOR THE EVOLUTION AND YIELDS FROM THE FIRST GENERATIONS OF STARS. *The Astrophysical Journal*, 727(2):89.

Herwig, F., Woodward, P. R., Lin, P.-H., Knox, M., and Fryer, C. (2014). GLOBAL NON-SPHERICAL OSCILLATIONS IN THREE-DIMENSIONAL 4π SIMULATIONS OF THE H-INGESTION FLASH. *The Astrophysical Journal Letters*, 792(1):L3.

Iben, Jr., I. (1975). Thermal pulses: P-capture, alpha -capture, s-process nucleosynthesis; and convective mixing in a star of intermediate mass. *The Astrophysical Journal*, 196:525–547.

Iliadis, C. (2015). *Nuclear Physics of Stars*. Wiley-VCH.

Issa, J., Herwig, F., Denissenkov, P., and Pignatari, M. (2025). Impact of 3D macro physics and nuclear physics on the p nuclei in O-C shell mergers.

Johnson, J. (2017). Where Your Elements Came From. *Astronomy Picture of the Day (APOD)*, NASA.

Jones, S., Andrassy, R., Sandalski, S., Davis, A., Woodward, P., and Herwig, F. (2017). Idealized hydrodynamic simulations of turbulent oxygen-burning shell convection in 4π geometry. *Monthly Notices of the Royal Astronomical Society*, 465:2991–3010.

Joyce, M. and Tayar, J. (2023). A Review of the Mixing Length Theory of Convection in 1D Stellar Modeling. *Galaxies*, 11(3):75.

Käppeler, F., Gallino, R., Bisterzo, S., and Aoki, W. (2011). The s process: Nuclear physics, stellar models, and observations. *Reviews of Modern Physics*, 83:157–194.

Kippenhahn, R., Weigert, A., and Weiss, A. (2013). *Stellar Structure and Evolution*. Springer.

Kobayashi, C., Karakas, A. I., and Lugaro, M. (2020). The Origin of Elements from Carbon to Uranium. *The Astrophysical Journal*, 900:179.

Lingenfelter, R. E. (2019). The Origin of Cosmic Rays: How Their Composition Defines Their Sources and Sites and the Processes of Their Mixing, Injection, and Acceleration. *The Astrophysical Journal Supplement Series*, 245(2):30.

Lodders, K., Palme, H., and Gail, H. P. (2009). Abundances of the Elements in the Solar System. *Landolt Börnstein*, 4B:712.

Masseron, T., García-Hernández, D. A., Santoveña, R., Manchado, A., Zamora, O., Manteiga, M., and Dafonte, C. (2020). Phosphorus-rich stars with unusual abundances are challenging theoretical predictions. *Nature Communications*, 11:3759.

Meakin, C. A. and Arnett, D. (2006). Active Carbon and Oxygen Shell Burning Hydrodynamics. *The Astrophysical Journal*, 637:L53–L56.

Meakin, C. A. and Arnett, D. (2007). Turbulent Convection in Stellar Interiors. I. Hydrodynamic Simulation. *The Astrophysical Journal*, 667:448–475.

Mewaldt, R. A. (1988). Elemental composition and energy spectra of galactic cosmic rays. In *Interplanetary Particle Environment*, pages 121–132.

Meyer, J.-P., Drury, L. O., and Ellison, D. C. (1997). Galactic Cosmic Rays from Supernova Remnants. I. A Cosmic-Ray Composition Controlled by Volatility and Mass-to-Charge Ratio. *The Astrophysical Journal*, 487(1):182.

Miller Bertolami, M. M., Althaus, L. G., Serenelli, A. M., and Panei, J. A. (2006). New evolutionary calculations for the born again scenario. *Astronomy and Astrophysics*, 449:313–326.

Mitler, H. E. (1970). Cosmic-Ray Production of Deuterium, He3, Lithium, Beryllium and Boron in the Galaxy. *SAO Special Report*, 330.

Müller, B. (2016). The Status of Multi-Dimensional Core-Collapse Supernova Models. *Publications of the Astronomical Society of Australia*, 33:e048.

Müller, B. (2020). Hydrodynamics of core-collapse supernovae and their progenitors. *Living Reviews in Computational Astrophysics*, 6:3.

Mumpower, M. R., Kawano, T., Sprouse, T. M., Vassh, N., Holmbeck, E. M., Surman, R., and Möller, P. (2018). β-delayed Fission in r-process Nucleosynthesis. *The Astrophysical Journal*, 869:14.

O'Neill, C., Lowman, J., and Wasiliev, J. (2020). The effect of galactic chemical evolution on terrestrial exoplanet composition and tectonics. *Icarus*, 352:114025.

Paxton, B., Bildsten, L., Dotter, A., Herwig, F., Lesaffre, P., and Timmes, F. (2010). MODULES FOR EXPERIMENTS IN StelLAR ASTROPHYSICS (MESA). *The Astrophysical Journal Supplement Series*, 192(1):3.

Pignatari, M., Gallino, R., Heil, M., Wiescher, M., Käppeler, F., Herwig, F., and Bisterzo, S. (2010). THE WEAK s-PROCESS IN MASSIVE STARS AND ITS DEPENDENCE ON THE NEUTRON CAPTURE CROSS SECTIONS. *The Astrophysical Journal*, 710(2):1557.

Pignatari, M., Göbel, K., Reifarth, R., and Travaglio, C. (2016a). The production of proton-rich isotopes beyond iron: The γ-process in stars. *International Journal of Modern Physics E*, 25(04):1630003.

Pignatari, M., Herwig, F., Hirschi, R., Bennett, M., Rockefeller, G., Fryer, C., Timmes, F. X., Ritter, C., Heger, A., Jones, S., Battino, U., Dotter, A., Trappitsch, R., Diehl, S., Frischknecht, U., Hungerford, A., Magkotsios, G., Travaglio, C., and Young, P. (2016b). NuGrid Stellar Data Set. I.Stellar Yields from H to Bi for Stars with Metallicities Z = 0.02 and Z = 0.01. *The Astrophysical Journal Supplement Series*, 225:24.

Prandtl, L. (1925). 7. Bericht über Untersuchungen zur ausgebildeten Turbulenz. *ZAMM - Journal of Applied Mathematics and Mechanics / Zeitschrift für Angewandte Mathematik und Mechanik, vol. 5, issue 2, pp. 136-139*, 5(2):136.

Prantzos, N., Hashimoto, M., Rayet, M., and Arnould, M. (1990). The p-process in SN 1987A. *Astronomy and Astrophysics*, 238:455–461.

Prialnik, D. (2009). *An Introduction to the Theory of Stellar Structure and Evolution*. Cambridge University Press.

Rapp, W., Görres, J., Wiescher, M., Schatz, H., and Käppeler, F. (2006). Sensitivity of p-Process Nucleosynthesis to Nuclear Reaction Rates in a 25 Msolar Supernova Model. *The Astrophysical Journal*, 653:474–489.

Rauscher, T., Dauphas, N., Dillmann, I., Fröhlich, C., Fülöp, Z., and Gyürky, G. (2013). Constraining the astrophysical origin of the p-nuclei through nuclear physics and meteoritic data. *Reports on Progress in Physics*, 76(6):066201.

Rauscher, T., Heger, A., Hoffman, R. D., and Woosley, S. E. (2002). Nucleosynthesis in Massive Stars with Improved Nuclear and Stellar Physics. *The Astrophysical Journal*, 576:323–348.

Rauscher, T., Nishimura, N., Hirschi, R., Cescutti, G., Murphy, A. St. J., and Heger, A. (2016). Uncertainties in the production of p nuclei in massive stars obtained from Monte Carlo variations. *Monthly Notices of the Royal Astronomical Society*, 463(4):4153–4166.

Rayet, M., Arnould, M., Hashimoto, M., Prantzos, N., and Nomoto, K. (1995). The p-process in Type II supernovae. *Astronomy and Astrophysics*, 298:517.

Rayet, M., Arnould, M., and Prantzos, N. (1990). The p-process revisited. *Astronomy and Astrophysics*, 227:271–281.

Renzini, A. (1987). Some embarrassments in current treatments of convective overshooting. *Astronomy and Astrophysics*, 188:49–54.

Ritter, C., Andrassy, R., Côté, B., Herwig, F., Woodward, P. R., Pignatari, M., and Jones, S. (2018a). Convective-reactive nucleosynthesis of K, Sc, Cl and p-process isotopes in O-C shell mergers. *Monthly Notices of the Royal Astronomical Society*, 474:L1–L6.

Ritter, C., Herwig, F., Jones, S., Pignatari, M., Fryer, C., and Hirschi, R. (2018b). NuGrid stellar data set - II. Stellar yields from H to Bi for stellar models with MZAMS = 1-25 M$\odot$ and Z = 0.0001-0.02. *Monthly Notices of the Royal Astronomical Society*, 480:538–571.

Rizzuti, F., Hirschi, R., Varma, V., Arnett, W. D., Georgy, C., Meakin, C., Mocák, M., Murphy, A. S., and Rauscher, T. (2024a). Shell mergers in the late stages of massive star evolution: New insight from 3D hydrodynamic simulations. *Monthly Notices of the Royal Astronomical Society*, 533:687–704.

Rizzuti, F., Hirschi, R., Varma, V., Arnett, W. D., Georgy, C., Meakin, C., Mocák, M., Murphy, A. S., and Rauscher, T. (2024b). Stellar Evolution and Convection in 3D Hydrodynamic Simulations of a Complete Burning Phase. *Galaxies*, 12:87.

Roberti, L., Pignatari, M., Brinkman, H. E., Jeena, S. K., Sieverding, A., Falla, A., Limongi, M., Chieffi, A., and Lugaro, M. (2025). The Occurrence and Impact of Carbon-Oxygen Shell Mergers in Massive Stars.

Roberti, L., Pignatari, M., Fryer, C., and Lugaro, M. (2024). The γ-process nucleosynthesis in core-collapse supernovae - II. Effect of the explosive recipe. *Astronomy & Astrophysics*, 686:L8.

Roberti, L., Pignatari, M., Psaltis, A., Sieverding, A., Mohr, P., Fülöp, Zs., and Lugaro, M. (2023). The γ-process nucleosynthesis in core-collapse supernovae: I. A novel analysis of γ-process yields in massive stars. *Astronomy & Astrophysics*, 677:A22.

Sackmann, I. J., Smith, R. L., and Despain, K. H. (1974). Carbon and eruptive stars: Surface enrichment of lithium, carbon, nitrogen, and 13C by deep mixing. *The Astrophysical Journal*, 187:555–574.

Schatz, H., Aprahamian, A., Barnard, V., Bildsten, L., Cumming, A., Ouellette, M., Rauscher, T., Thielemann, F. K., and Wiescher, M. (2001). End Point of the rp Process on Accreting Neutron Stars. *Physical Review Letters*, 86:3471–3474.

Schatz, H., Aprahamian, A., Görres, J., Wiescher, M., Rauscher, T., Rembges, J. F., Thielemann, F. K., Pfeiffer, B., Möller, P., Kratz, K. L., Herndl, H., Brown, B. A., and Rebel, H. (1998). Rp-process nucleosynthesis at extreme temperature and density conditions. *Physics Reports*, 294(4):167–263.

Sieverding, A., Martínez-Pinedo, G., Huther, L., Langanke, K., and Heger, A. (2018). The ν-Process in the Light of an Improved Understanding of Supernova Neutrino Spectra. *The Astrophysical Journal*, 865:143.

Smith, N. and Arnett, W. D. (2014). PREPARING FOR AN EXPLOSION: HYDRODYNAMIC INSTABILITIES AND TURBULENCE IN PRESUPERNOVAE. *The Astrophysical Journal*, 785(2):82.

Sneden, C., Cowan, J. J., and Gallino, R. (2008). Neutron-capture elements in the early galaxy. *Annual Review of Astronomy and Astrophysics*, 46:241–288.

Tatischeff, V., Raymond, J. C., Duprat, J., Gabici, S., and Recchia, S. (2021). The origin of Galactic cosmic rays as revealed by their composition. *Monthly Notices of the Royal Astronomical Society*, 508:1321–1345.

Travaglio, C., Gallino, R., Rauscher, T., Röpke, F. K., and Hillebrandt, W. (2015). Testing the Role of SNe Ia for Galactic Chemical Evolution of p-nuclei with Two-dimensional Models and with s-process Seeds at Different Metallicities. *The Astrophysical Journal*, 799:54.

Travaglio, C., Rauscher, T., Heger, A., Pignatari, M., and West, C. (2018). Role of Core-collapse Supernovae in Explaining Solar System Abundances of p Nuclides. *The Astrophysical Journal*, 854(1):18.

Travaglio, C., Röpke, F. K., Gallino, R., and Hillebrandt, W. (2011). Type Ia Supernovae as Sites of the p-process: Two-dimensional Models Coupled to Nucleosynthesis. *The Astrophysical Journal*, 739:93.

Viallet, M., Baraffe, I., and Walder, R. (2011). Towards a new generation of multi-dimensional stellar evolution models: Development of an implicit hydrodynamic code. *Astronomy & Astrophysics*, 531:A86.

Woosley, S. E. and Heger, A. (2007). Nucleosynthesis and remnants in massive stars of solar metallicity. *Physics Reports*, 442:269–283.

Woosley, S. E., Heger, A., and Weaver, T. A. (2002). The evolution and explosion of massive stars. *Reviews of Modern Physics*, 74:1015–1071.

Woosley, S. E. and Hoffman, R. D. (1992). The alpha -Process and the r-Process. *The Astrophysical Journal*, 395:202.

Woosley, S. E. and Howard, W. M. (1978). The p-processes in supernovae. *The Astrophysical Journal Supplement Series*, 36:285–304.

Xiong, Z., Martínez-Pinedo, G., Just, O., and Sieverding, A. (2024). Production of \$p\$ Nuclei from \$r\$-Process Seeds: The \$\ensuremath{\nu}r\$ Process. *Physical Review Letters*, 132(19):192701.

Yadav, N., Müller, B., Janka, H. T., Melson, T., and Heger, A. (2020). Large-scale Mixing in a Violent Oxygen–Neon Shell Merger Prior to a Core-collapse Supernova. *The Astrophysical Journal*, 890(2):94.